

DESIGN AND APPLICATIONS OF GOLD NANOPARTICLES FOR
ION SENSING AND CANCER THERAPEUTICS

by

Jonghae Youn



APPROVED BY SUPERVISORY COMMITTEE:

Dr. Jiyong Lee, Chair

Dr. Kenneth J. Balkus Jr.

Dr. Gabriele Meloni

Dr. Paul Pantano

Copyright 2019

Jonghae Youn

All Rights Reserved

To Jinyoung and Jia
for keeping my heart, mind and soul.

DESIGN AND APPLICATIONS OF GOLD NANOPARTICLES FOR
ION SENSING AND CANCER THERAPEUTICS

by

JONGHAE YOUN, MS

DISSERTATION

Presented to the Faculty of
The University of Texas at Dallas
in Partial Fulfillment
of the Requirements
for the Degree of

DOCTOR OF PHILOSOPHY IN
CHEMISTRY

THE UNIVERSITY OF TEXAS AT DALLAS

May 2019

ACKNOWLEDGMENTS

I am grateful for the help and encouragement of my many colleagues, friends, and family members. First, I would like to express deep appreciation to my advisor, Prof. Jiyong Lee for fostering me to grow as an independent scientist and for providing me with professional and personal support throughout my 5 years.

I would also like to thank my committee members Prof. Kenneth Balkus, Prof. Gabriele Meloni and Prof. Paul Pantano for their insight and invaluable advice. The discussion and questions inspired me to think more deeply about my research from different angles. I would like to thank Prof. Zhenpeng Qin for supporting our gold nanorod project. I am also grateful for the help of Dr. Jae Ho Shin who initially gave me the motivation to start my scientific studies and let me to the doctoral study.

I am thankful to my past and present members of the Lee lab and other collaborators. It was a great pleasure to work and discuss with Maria Castañeda, Dr. Chao Long, and Jennifer Nguyen, who provided me invaluable insights and discussion. It would not be possible to complete this long journey without them. I would also like to thank to members of the Nano-Thermal Bioengineering Lab: Dr. Hejian Xiong and Xiaoqing Li. I am especially grateful to my collaborator, Peiyuan Kang for his help and guidance in the gold nanorod project.

I would like to thank my old friends: Yongbin Kim at Purdue University and Yujin Jang at North Carolina State University. Although we are studying far away from each other, you gave a great strength to me to face the uncertainty of my future. I will pray for all of you to successfully complete your PhD studies.

The friends I have made at The University of Texas at Dallas have made each day a little brighter: Dr. Yoon Jung Kim, Dr. Youngchul Byun, Dr. Jaegil Lee, Dr. Si-Joon Kim, Jaebeom Lee, Harrison Kim, and Su Min Hwang.

Most of all, I would like to thank my family: my parents, brother and my parents-in-law for their unconditional love and encouragement, my wife Jinyoung for her unending support, and my daughter Jia for always giving me a reason to smile. I thank you all from the bottom of my heart.

March 2019

DESIGN AND APPLICATIONS OF GOLD NANOPARTICLES FOR ION SENSING AND CANCER THERAPEUTICS

Jonghae Youn, PhD
The University of Texas at Dallas, 2019

Supervising Professor: Jiyong Lee, PhD

Gold nanoparticles have been studied extensively because their size- and shape-dependent chemical, physical, and optical characteristics, as well as, their surface chemistry that makes them a more powerful tool in a variety of fields. In this dissertation, two studies were carried out to design new gold nanoparticles by selecting the appropriate size, shape, and surface ligands for cancer therapy and metal ion sensing.

In the first project, I developed a novel gold nanorod that selectively targets and ablates cancer stem cells (CSCs) via photothermal therapy. CSCs have been identified as a new target for cancer therapy due to their unique characteristics of tumor initiation, recurrence, metastasis, and drug resistance. Despite extensive research that has provided new targets, technologies, and tools for CSC treatment, the practical use of these is limited. Herein, I report that gold nanorods by functionalized with the CL-1-19-1 ligand selectively binds to CSCs versus non-CSCs, and they can decrease CSC populations via laser-induced photothermal therapy. I demonstrated that gold nanorods bound to an Aldehyde dehydrogenase (ALDH) positive subpopulation rather than Aldehyde dehydrogenase negative subpopulation. Breast cancer cells treated with gold nanorods

following laser irradiation (the nanosecond pulsed laser at 532 nm) showed decreased number of ALDH positive cells (>50% compared to control group) and diminished expressions of CSC-associated transcription factors. Thus, these results suggested an effective platform to eradicate CSCs.

In the second project, I took advantage of the reduction capability of tyrosine at alkaline conditions to develop peptide-templated fluorescent gold nanoclusters (AuNCs). In order to better understand the role of tyrosine in forming fluorescent AuNC, tripeptides, tyrosine-cysteine-tyrosine (YCY) and serine-cysteine-tyrosine (SCY), were designed and prepared. Then under a pH of 10 and 70 °C, we obtained AuNCs of blue and red fluorescence from YCY peptide and the AuNC of blue fluorescence from SCY peptide. Transmission electron microscopy (TEM) and dynamic light scattering (DLS) revealed that peptide-templated AuNCs possessed a spherical shape and narrow particle size distribution in aqueous solution. Furthermore, I found that the fluorescence of blue-emitting YCY- and SCY-AuNCs is quenched with Fe^{3+} and Cu^{2+} in a wide liner range, while the fluorescence of the red-emitting YCY-AuNC are stable in 13 different metal ion solutions. Interestingly, blue-YCY-AuNC was more than doubly responsive to Fe^{3+} compared to SCY-AuNC presumably due to the presence of two tyrosine residues, causing enhanced aggregation propensity under the presence of Fe^{3+} in DLS measurement. These results thus suggest the chelation effect between the peptide on the AuNC surface and the target ion resulted in aggregation, which was found to cause fluorescence quenching. In addition, the DLS data demonstrates that the aggregation propensity is closely related to the sensitivity of the sensing system to the target metal ion.

TABLE OF CONTENTS

ACKNOWLEDGMENTS	v
ABSTRACT	vii
LIST OF FIGURES	xii
LIST OF SCHEMES	xiv
LIST OF TABLES.....	xv
LIST OF ABBREVIATIONS	xvi
CHAPTER 1 INTRODUCTION	1
1.1 Gold nanoparticles	1
1.2 Opto-physical properties of gold nanoparticles at different size and shape	1
1.2.1 Size	1
1.2.2 Shape and structure.....	4
1.3 References	5
CHAPTER 2 SELECTIVE ELIMINATION OF CANCER STEM CELLS BY GOLD NANOROD-MEDIATED HYPERTHERMIA.....	10
2.1 Introduction.....	10
2.2 Experimental section	15
2.2.1 Reagents and materials.....	15
2.2.2 Synthesis of ligands.....	16
2.2.3 Preparation and characterization of the ligand-modified AuNRs	17
2.2.4 Cell lines.....	17
2.2.5 Silver staining.....	18
2.2.6 Cell viability assay	18
2.2.7 In situ ALDEFLUOR assay	19
2.2.8 Isolation of breast CSCs using FACS	20
2.2.9 Western blot analysis	21
2.2.10 Two-photon luminescence imaging	22
2.3 Result and discussion	22

2.3.1	Preparation and characterization of AuNRs.....	22
2.3.2	Cell binding study	26
2.3.3	Cytotoxicity of AuNR-mediated hyperthermia.....	27
2.3.4	Targeting ability of #1-AuNR to CSCs.....	30
2.3.5	Effect of the AuNR-mediated hyperthermia on CSC	33
2.4	Conclusions	34
2.5	Supplementary information.....	36
2.6	References.....	38
CHAPTER 3 TYROSINE-ASSISTED GOLD NANOCUSTER FOR SENSING FERRIC AND COOPER IONS		51
3.1	Introduction	51
3.2	Experimental section.....	53
3.2.1	Reagents and materials.....	53
3.2.2	Synthesis of tripeptides	54
3.2.3	Preparation of YCY- and SCY-templated fluorescent AuNCs.....	55
3.2.4	Characterization of AuNCs	56
3.2.5	The influence of pH and NaCl on fluorescence intensity	56
3.2.6	Fluorescent detections of metal ions	57
3.2.7	Quantum yield (QY) measurement of AuNCs.....	57
3.3	Results and discussion	58
3.3.1	Preparation of AuNCs	58
3.3.2	The optical and physical characteristics of AuNCs	61
3.3.3	Metal ion selectivity and sensitivity of AuNCs	66
3.3.4	Sensing mechanism.....	69
3.4	Conclusion	71
3.5	Supplementary information.....	73
3.5.1	Cell viability test	76
3.6	References.....	77
CHAPTER 4 SUMMARY AND FUTURE RESEARCH DIRECTION.....		83
4.1	Summary	83

4.2	Future research direction.....	84
4.2.1	Cancer stem cell targeted nanomaterials.....	84
4.2.2	Gold nanocluster for metal ions sensing and bioimaging.....	85
4.3	References.....	86
	BIOGRAPHICAL SKETCH.....	89
	CURRICULUM VITAE.....	91

LIST OF FIGURES

Figure 2.1 Optimization of ligand concentrations and stability of AuNRs in high salt solution.	24
Figure 2.2 Characterization of AuNRs.	25
Figure 2.3 Binding distribution of AuNRs in breast cancer cells.	27
Figure 2.4 Intact cell binding distribution of AuNRs in MCF-7	28
Figure 2.5 Effect of the AuNR-mediated hyperthermia on cell viability.	29
Figure 2.6 FACS analysis of ALDH ⁺ subpopulation in MCF-7 cells using the ALDEFLUOR™ assay	31
Figure 2.7 Examination of selectivity of #1-AuNR toward CSCs.	32
Figure 2.8 Analysis of CSC subpopulation in MCF-7 under the AuNR-mediated hyperthermia via in situ ALDELFUOR assay	33
Figure 2.9 Effect of AuNR-mediated hyperthermia on expression of stemness-associated transcription factors	35
Figure S.2.1 Characterization of the #1 ligand.	36
Figure S.2.2 Characterization of the #1 ligand.	37
Figure 3.1 Effect of different pH on synthesis of tyrosine-assisted AuNCs	60
Figure 3.2 UV-Vis and fluorescence spectra of AuNCs	62
Figure 3.3 Size analysis of AuNCs using TEM and DLS	63
Figure 3.4 Stability of AuNCs in high salt solution and different pH buffer	65
Figure 3.5 Effect of metal ions on fluorescence intensities of AuNCs	66
Figure 3.6 Fluorescence responses of Blue-YCY- and SCY-AuNCs to Fe ³⁺ and Cu ²⁺	67
Figure 3.7 Hydrodynamic diameter analysis of AuNCs in the presence of metal ions.	70

Figure S.3.1 Characterization of YCY peptide.....	73
Figure S.3.2 Characterization of SCY peptide	74
Figure S.3.3 Purification of AuNCs via size exclusion column.....	75
Figure S.3.3 Cytotoxicity of AuNCs	76

LIST OF SCHEMES

Scheme 1.1 The size effect on optical and physical properties on gold nanoparticles.....	2
Scheme 1.2 Illustration of surface plasmon resonance in gold nanoparticles	3
Scheme 1.3 Illustration of surface plasmon resonance in gold nanorod	4
Scheme 2.1 Schematic illustration of the ligand-conjugated AuNRs preparation procedure	23
Scheme 3.1 Schematic illustration of the preparation of fluorescent AuNC via tyrosine-assisted reduction.....	59

LIST OF TABLES

Table 2.1 Summary of wavelength at maximum OD and ζ -potential with different surface ligands	26
Table 3.1 Comparison sensing activity of Blue-YCY-AuNC and Blue-SCY-AuNC for Fe^{3+} and Cu^{2+}	68

LIST OF ABBREVIATIONS

ADC	Antibody drug conjugate
ABC	ATP-binding cassette
ALDH	Aldehyde dehydrogenase
ATP	Adenosine triphosphate
AuNC	Gold nanocluster
AuNP	Gold nanoparticle
AuNS	Gold nanoshell
BCA	Bicinchoninic acid
CD271	Nerve growth factor receptor
CSC	Cancer stem cell
Ctrl	Control
DCM	Dichloromethane
DEAB	<i>N,N</i> -diethylaminobenzaldehyde
DHLA	Dihydrolipoic acid
DLL-3	Delta like 3
DLL-4	Delta like 4
DLS	Dynamic light scattering
DMEM	Dulbecco's modified Eagle medium
DMF	Dimethylformamide
DMSO	Dimethyl sulfoxide
DPBS	Dulbecco's Phosphate-Buffered Saline
EMT	Epithelial-mesenchymal transition
FACS	Fluorescence-activated cell sorting
FAK	Focal adhesion kinase
FBS	Fetal bovine serum
FL	Fluorescence
Fmoc	Fluorenylmethoxycarbonyl protecting group

GSH	Glutathione
HBTU	2-(1 <i>H</i> -benzotriazol-1-yl)-1,1,3,3-tetramethyluronium hexafluorophosphate
HOBt	Hydroxybenzotriazole
HPLC	High-performance liquid chromatography
LC	Liquid chromatography
LGR5	Leucine-rich repeat-containing G-protein coupled receptor 5
MeOH	Methanol
mPEG-SH	Methoxypolyethylene glycol thiol
MALDI-TOF	Matrix-assisted laser desorption/ionization
MS/MS	Tandem mass spectrometry
MTT	3-(4,5-dimethylthiazol-2-yl)-2,5-diphenyltetrazolium bromide
NMP	<i>N</i> -Methyl-2-pyrrolidone
PAGE	Polyacrylamide gel electrophoresis
PBS	Phosphate buffered saline
PEI	Polyethylenimine
PVDF	Polyvinylidene fluoride
RP	Reverse-phase
RT	Room temperature
SCY	Serine-Cysteine-Tyrosine
SDS	Sodium dodecyl sulfate
SPR	Surface plasmon resonance
STAT3	Signal transducer and activator of transcription 3
TBS-T	Tris-buffered saline with Tween 20
tBu	Tert-butyl
TEM	Transmission electron microscopy
TFA	Trifluoroacetic acid
TIS	Triisopropylsilane
Trt	Trityl

YCY

Tyrosine-Cysteine-Tyrosine

CHAPTER 1

INTRODUCTION

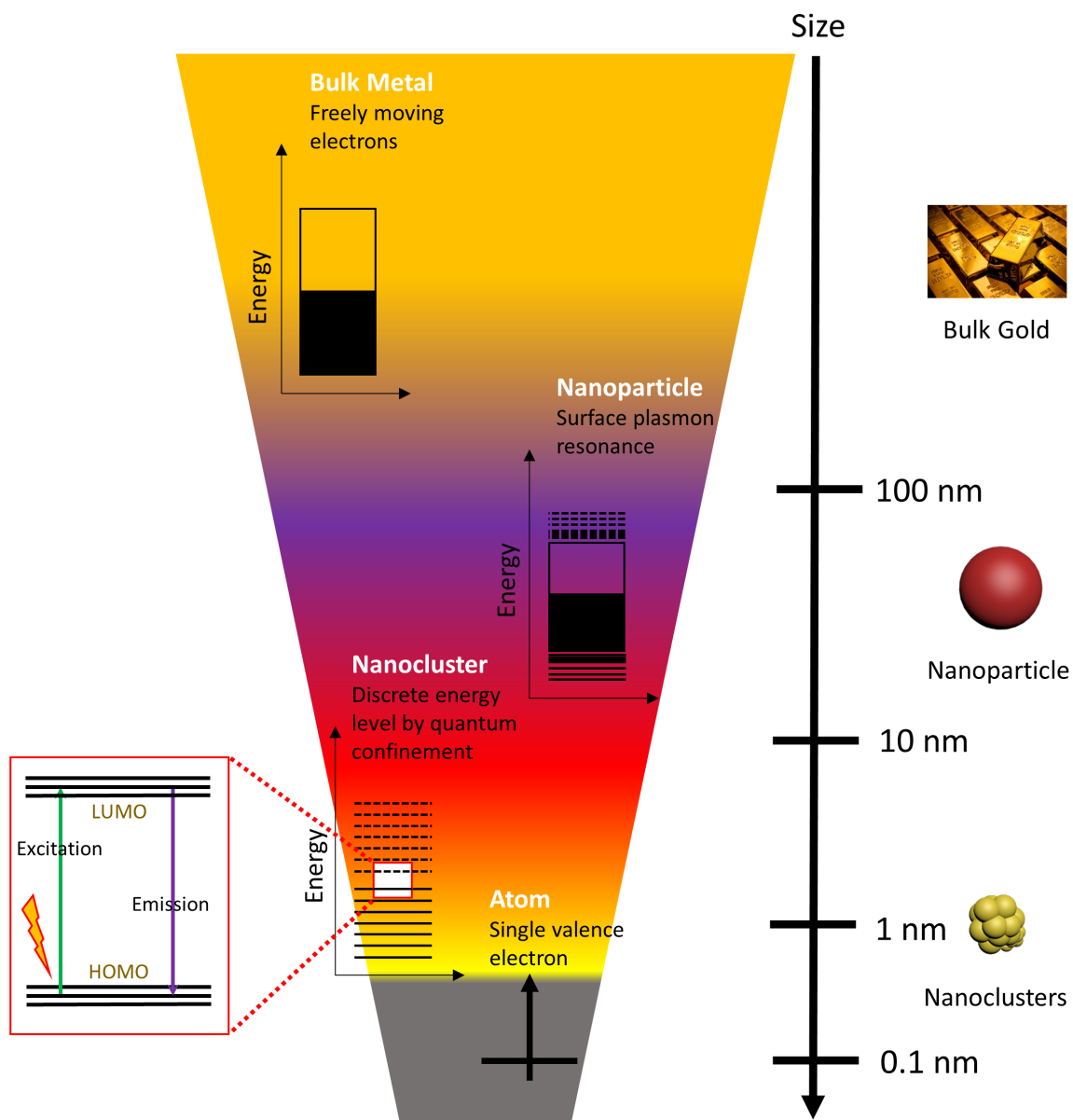
1.1 Gold nanomaterials

In the last two decades, gold nanomaterials have been considered attractive research subjects due to their distinctive features such as exceptional chemical and physical stability, surface modification with ligands, and size-dependent electrical and optical characteristics.¹⁻⁴ Among these, the optical and physical behaviors of gold nanomaterials with different size and structure have expanded their biomedical use as therapeutic tools, imaging, and sensing tools.⁵⁻⁷ In this chapter, we will briefly review the concepts of the optical and physical properties of gold nanomaterials with different sizes and structures and also introduce some representative applications.

1.2 Opto-physical properties of gold nanoparticles at different size and shape

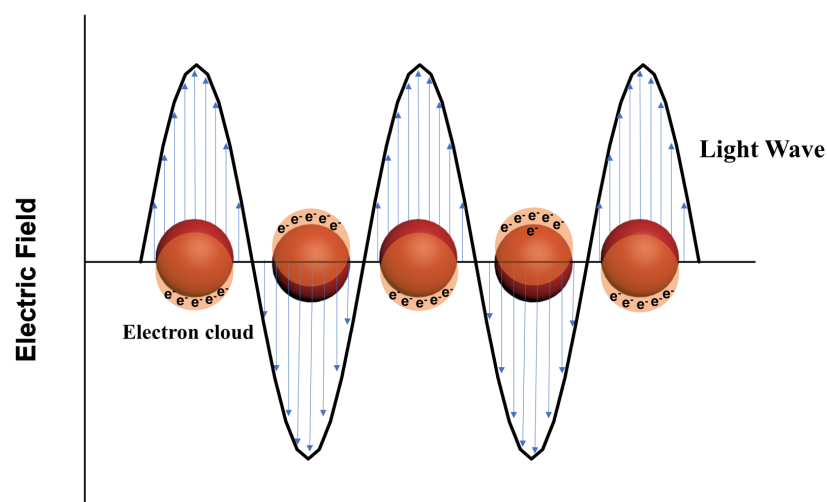
1.2.1 Size

The size of gold nanoparticles is a crucial factor to determine the physical, electrical, and chemical properties of gold (Scheme 1.1). While the free electrons in bulk gold thoroughly move through the entire system, all interactions in a system having a smaller size than 100 nm are happened with the surface.⁸ As depicted in Scheme 1.2, when the nanoparticle is exposed to the light that has a larger wavelength of electromagnetic radiation than the size of the particle, the light in resonance induces the electron density in the nanoparticle to be polarized to one side, resulting in a collective coherent oscillation of the electrons on the surface of the nanoparticle, called surface plasmon resonance (SPR).³ A strong light absorption caused by the SPR can be measured using a



Scheme 1.1. The size effect on optical and physical properties on gold nanoparticles.

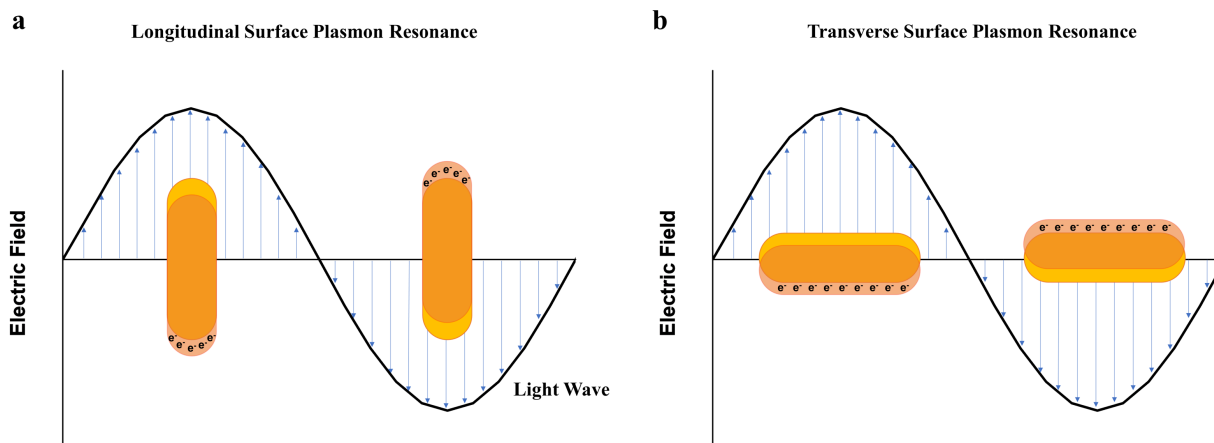
UV-Vis spectrometer. The factors associated with the density of the electron charge, such as the particle size, shape, surface components, and structure affect the absorption intensity and wavelength of the SPR band.^{9,10} Decreasing the particle size gradually decreases the intensity of SPR intensity and induces a blueshift.¹¹ When the size is smaller than 10 nm, the band of AuNP is



Scheme 1.2. Illustration of surface plasmon resonance in gold nanoparticles.

mostly damped because of higher rate of electron-surface collisions than in larger particles. Large AuNPs (>100 nm) have broad absorption peaks due to the higher level of electron oscillations.⁸ These unique optical and electrical properties of gold nanomaterials lead to biosensing and bioimaging applications. The Mirkin group has pioneered the use of AuNP-oligonucleotide conjugations in detection of their target.^{12,13}

Eventually, when the size of a AuNP is close to the Fermi wavelength of an electron, the particle is comprised of several number of gold atoms, called gold nanocluster (AuNC), and it has completely different optical and electrical properties from plasmonic AuNP (> 10 nm). In this size range, the continuous energy bands break into discrete energy levels, resulting in “single molecule like fluorescence”.¹⁴⁻¹⁶ Unlike a single molecule fluorophore, AuNC possesses large Stoke-shift, low toxicity in biological system, tunable emission wavelength, excellent photostability and high quantum yield.¹⁷⁻¹⁹ These distinctive properties enable AuNCs to be potential nanomaterials for applications in bioimaging, sensing tools, and biomedicine.²⁰⁻²²



Scheme 1.3. Illustration of surface plasmon resonance in gold nanorod. (a) Longitudinal surface plasmon resonance. (b) Transverse surface plasmon resonance.

1.2.2 Shape and structure

In addition to the size, SPR bands can be tuned by changing their shapes. With advanced nanoparticle preparation, synthesis methods for gold nanorod (AuNR) and gold nanoshell (AuNS) have been established.²³⁻²⁵ AuNRs have two split bands: a strong peak in NIR region originated from electron oscillations of the longitudinal axis and a weak band in the visible region originated from transverse axis (Scheme 1.3). With the increasing ratio of length and width in AuNR, the wavelength at longitudinal SPR peak increases up towards the red and above, resulting in color changes of AuNR. The SPR peak of AuNS composing of silica core and thin gold shell can be tuned by modifying the shell thickness. With decrease of the shell thickness from 20 to 5 nm, the SPR peak increases about 300 nm, because of more plasmonic coupling between the outer and inner shell.²⁶ In addition to SPR characteristic, AuNPs has a capacity to convert light energy to heat energy.²⁷ Thus, AuNPs have been utilized as mediators of photothermal therapy, in which the generated heat is sufficient to kill or damage the cells via hyperthermia.^{28,29} Furthermore, by using

different type of laser, such as pulsed and continuous wave visible laser, treatment region can be controlled.¹ For instance, a nanosecond pulsed laser is usually applied to achieve “selective photothermolysis” and an ablation of single cell, whereas a continuous wave laser can be utilized for extensive cell death.³⁰⁻³⁴ In summary, these studies suggest that gold nanomaterials can be potential tools for biomedical and chemical applications.

1.3 References

- (1) Qin, Z.; Bischof, J. C. Thermophysical and Biological Responses of Gold Nanoparticle Laser Heating. *Chem. Soc. Rev.* **2012**, *41*, 1191–1217.
- (2) García, I.; Sánchez-Iglesias, A.; Henriksen-Lacey, M.; Grzelczak, M.; Penadés, S.; Liz-Marzán, L. M. Glycans as Biofunctional Ligands for Gold Nanorods: Stability and Targeting in Protein-Rich Media. *J. Am. Chem. Soc.* **2015**, *137*, 3686–3692.
- (3) Amendola, V.; Pilot, R.; Frasconi, M.; Maragò, O. M.; Iatì, M. A. Surface Plasmon Resonance in Gold Nanoparticles: a Review. *J. Phys.: Condens. Matter* **2017**, *29*, 203002–203049.
- (4) Kister, T.; Monego, D.; Mulvaney, P.; Widmer-Cooper, A.; Kraus, T. Colloidal Stability of Apolar Nanoparticles: the Role of Particle Size and Ligand Shell Structure. *ACS Nano* **2018**, *12*, 5969–5977.
- (5) Liu, Y.; Yang, M.; Zhang, J.; Zhi, X.; Li, C.; Zhang, C.; Pan, F.; Wang, K.; Yang, Y.; Martinez de la Fuentea, J. Cui, D. Human Induced Pluripotent Stem Cells for Tumor Targeted Delivery of Gold Nanorods and Enhanced Photothermal Therapy. *ACS Nano* **2016**, *10*, 2375–2385.

- (6) Gao, L.; Liu, M.; Ma, G.; Wang, Y.; Zhao, L.; Yuan, Q.; Gao, F.; Liu, R.; Zhai, J.; Chai, Z.; Zhao, Y.; Gao, X. Peptide-Conjugated Gold Nanoprobe: Intrinsic Nanozyme-Linked Immunosorbant Assay of Integrin Expression Level on Cell Membrane. *ACS Nano* **2015**, *9*, 10979–10990.
- (7) Tong, L.; Lu, E.; Pichaandi, J.; Cao, P.; Nitz, M.; Winnik, M. A. Quantification of Surface Ligands on NaYF₄ Nanoparticles by Three Independent Analytical Techniques. *Chem. Mater.* **2015**, *27*, 4899–4910.
- (8) Eustis, S.; El-Sayed, M. A. Why Gold Nanoparticles Are More Precious Than Pretty Gold: Noble Metal Surface Plasmon Resonance and Its Enhancement of the Radiative and Nonradiative Properties of Nanocrystals of Different Shapes. *Chem. Soc. Rev.* **2006**, *35*, 209–217.
- (9) Kelly, K. L.; Coronado, E.; Zhao, L. L.; Schatz, G. C. The Optical Properties of Metal Nanoparticles: the Influence of Size, Shape, and Dielectric Environment. *J. Phys. Chem. B* **2003**, *107*, 668–677.
- (10) Link, S.; El-Sayed, M. A. Size and Temperature Dependence of the Plasmon Absorption of Colloidal Gold Nanoparticles. *J. Phys. Chem. B* **1999**, *103*, 4212–4217.
- (11) Jin, R.; Cao, Y.; Mirkin, C. A.; Kelly, K. L.; Schatz, G. C.; Zheng, J. G. Photoinduced Conversion of Silver Nanospheres to Nanoprisms. *Science* **2001**, *294*, 1901–1903.
- (12) Elghanian, R.; Storhoff, J. J.; Mucic, R. C.; Letsinger, R. L.; Mirkin, C. A. Selective Colorimetric Detection of Polynucleotides Based on the Distance-Dependent Optical Properties of Gold Nanoparticles. *Science* **1997**, *277*, 1078–1081.

- (13) Reynolds, R. A.; Mirkin, C. A.; Letsinger, R. L. Homogeneous, Nanoparticle-Based Quantitative Colorimetric Detection of Oligonucleotides. *J. Am. Chem. Soc.* **2000**, *122*, 3795–3796.
- (14) Link, S.; Beeby, A.; FitzGerald, S.; El-Sayed, M. A.; Schaaff, T. G.; Whetten, R. L. Visible to Infrared Luminescence From a 28-Atom Gold Cluster. **2002**, *106*, 3410–3415.
- (15) Lee, T.-H.; Gonzalez, J. I.; Zheng, J.; Dickson, R. M. Single-Molecule Optoelectronics. *Acc. Chem. Res.* **2005**, *38*, 534–541.
- (16) Zheng, J.; Nicovich, P. R.; Dickson, R. M. Highly Fluorescent Noble-Metal Quantum Dots. *Annu. Rev. Phys. Chem.* **2007**, *58*, 409–431.
- (17) Zhang, L.; Wang, E. Metal Nanoclusters: New Fluorescent Probes for Sensors and Bioimaging. *Nano Today* **2014**, *9*, 132–157.
- (18) Jin, R.; Zeng, C.; Zhou, M.; Chen, Y. Atomically Precise Colloidal Metal Nanoclusters and Nanoparticles: Fundamentals and Opportunities. *Chem. Rev.* **2016**, *116*, 10346–10413.
- (19) Zheng, Y.; Lai, L.; Liu, W.; Jiang, H.; Wang, X. Recent Advances in Biomedical Applications of Fluorescent Gold Nanoclusters. *Adv. Colloid Interface Sci.* **2017**, *242*, 1–16.
- (20) Zhang, J.; Cheng, F.; Li, J.; Zhu, J.-J.; Lu, Y. Fluorescent Nanoprobes for Sensing and Imaging of Metal Ions: Recent Advances and Future Perspectives. *Nano Today* **2016**, *11*, 309–329.
- (21) Saha, K.; Agasti, S. S.; Kim, C.; Li, X.; Rotello, V. M. Gold Nanoparticles in Chemical and Biological Sensing. *Chem. Rev.* **2012**, *112*, 2739–2779.
- (22) Zheng, K.; Setyawati, M. I.; Leong, D. T.; Xie, J. Antimicrobial Gold Nanoclusters. *ACS Nano* **2017**, *11*, 6904–6910.

- (23) Murphy, C. J.; Sau, T. K.; Gole, A. M.; Orendorff, C. J.; Gao, J.; Gou, L.; Hunyadi, S. E.; Li, T. Anisotropic Metal Nanoparticles: Synthesis, Assembly, and Optical Applications. *J. Phys. Chem. B* **2005**, *109*, 13857–13870.
- (24) Nikoobakht, B.; El-Sayed, M. A. Preparation and Growth Mechanism of Gold Nanorods (NRs) Using Seed-Mediated Growth Method. *Chem. Mater.* **2003**, *15*, 1957–1962.
- (25) Oldenburg, S. J.; Averitt, R. D.; Westcott, S. L.; Halas, N. J. Nanoengineering of Optical Resonances. *Chem. Phys. Lett.* **1998**, *288*, 243–247.
- (26) Prodan, E.; Radloff, C.; Halas, N. J.; Nordlander, P. A Hybridization Model for the Plasmon Response of Complex Nanostructures. *Science* **2003**, *302*, 419–422.
- (27) Jaque, D.; Martínez Maestro, L.; del Rosal, B.; Haro-Gonzalez, P.; Benayas, A.; Plaza, J. L.; Martín Rodríguez, E.; García Solé, J. Nanoparticles for Photothermal Therapies. *Nanoscale* **2014**, *6*, 9494–9530.
- (28) Conde, J.; Oliva, N.; Zhang, Y.; Artzi, N. Local Triple-Combination Therapy Results in Tumour Regression and Prevents Recurrence in a Colon Cancer Model. *Nature Mater* **2016**, *15*, 1128–1138.
- (29) Chen, J.; Li, X.; Zhao, X.; Wu, Q.; Zhu, H.; Mao, Z.; Gao, C. Doxorubicin-Conjugated pH-Responsive Gold Nanorods for Combined Photothermal Therapy and Chemotherapy of Cancer. *Bioact. Mater.* **2018**, *3*, 347–354.
- (30) Kang, P.; Chen, Z.; Nielsen, S. O.; Hoyt, K.; D'Arcy, S.; Gassensmith, J. J.; Qin, Z. Molecular Hyperthermia: Spatiotemporal Protein Unfolding and Inactivation by Nanosecond Plasmonic Heating. *Small* **2017**, *13*, 1700841–1700847.

- (31) Ali, M. R. K.; Wu, Y.; Tang, Y.; Xiao, H.; Chen, K.; Han, T.; Fang, N.; Wu, R.; El-Sayed, M. A. Targeting Cancer Cell Integrins Using Gold Nanorods in Photothermal Therapy Inhibits Migration Through Affecting Cytoskeletal Proteins. *Proc. Natl. Acad. Sci. U.S.A.* **2017**, *114*, E5655–E5663.
- (32) Zharov, V. P.; Mercer, K. E.; Galitovskaya, E. N.; Smeltzer, M. S. Photothermal Nanotherapeutics and Nanodiagnostics for Selective Killing of Bacteria Targeted with Gold Nanoparticles. *Biophys. J.* **2006**, *90*, 619–627.
- (33) Lapotko, D. O.; Lukianova, E.; Oraevsky, A. A. Selective Laser Nano-Thermolysis of Human Leukemia Cells with Microbubbles Generated Around Clusters of Gold Nanoparticles. *Lasers Surg. Med.* **2006**, *38*, 631–642.
- (34) Zharov, V. P.; Letfullin, R. R.; Galitovskaya, E. N. Microbubbles-Overlapping Mode for Laser Killing of Cancer Cells with Absorbing Nanoparticle Clusters. *J. Phys. D: Appl. Phys.* **2005**, *38*, 2571–2581.

CHAPTER 2

SELECTIVE ELIMINATION OF CANCER STEM CELLS BY GOLD NANOROD MEDIATED HYPERTHERMIA

2.1 Introduction

Despite advances in cancer treatment, cancer recurrence, metastasis, and therapy resistance lead to cancer remaining as one of the most fatal diseases. Several studies for a few decades have identified that a small population of cancer cells, which are called cancer stem cells (CSCs), are implicated with a poor prognosis of cancer.¹ Recent studies have strongly supported the CSC hypothesis, which demonstrates that a minor population of CSCs are capable of self-renewal, differentiation, proliferation and immune regulation, thereby playing important roles in tumor initiation, recurrence, metastasis, and therapy resistance.²⁻⁴ The first experimental evidence for the CSC hypothesis was reported in 1997 from Dick's group.⁵ They provided the evidence that human leukemias were driven from a small population of leukemic stem cells. This hypothesis has been extended by providing specific CSC surface markers CD44⁺/CD24⁻/lin⁻ in human breast cancers.⁶⁻⁸ Afterward, in many cancers including melanoma, prostate cancer, brain cancer, colon, pancreatic, and head and neck cancers, the biomarkers to identify CSCs have been validated *in vitro* and in mouse models.⁹⁻¹⁴ In recent studies, distinct properties of CSCs compared to non-CSCs have been discovered, such as improvement of DNA damage repair, epithelial-mesenchymal transition, enhanced resistance to physiologic oxidative stress, metabolic reprogramming, and immune invasion and suppression.^{4,15-23} Therefore, successful targeting of CSC is an ultimate goal to overcome challenges of current cancer treatments.

CSCs have been identified as therapeutic targets to overcome the limitations of current cancer drugs and they have inspired the innovative designs of drugs and treatment strategies.

Identifying signaling pathways and functional regulators of CSCs in human cancers have contributed to the development of CSC targeted drug design and therapeutic strategies. Direct targeting of CSCs is one of the strategies to eliminate CSC populations. Advanced techniques, such as fluorescence-activated cell sorting (FACS)-based transplantation, barcode-tagging and tracing, lineage tracing, and other biological assays, have identified markers of CSCs.^{1,4,24} For instances, nerve growth factor receptor (CD271) was identified a specific marker of human melanoma.²⁵ Pascual *et al.* found CD36, the fatty acid receptor, as a target of melanoma and breast cancer.²⁶ As mentioned above, heterogeneous CSC markers, CD44⁺/CD24⁻, are closely associated with breast cancer stem cells. Based on CSC markers, antibody-drug conjugate (ADC) targeting markers of CSCs have been emerged as one of the most promising therapeutic strategies to eliminate CSCs, and many anti-CSC ADCs have been studied and some of these are currently being in clinical trials.^{27,28} For example, cell surface leucine-rich repeat-containing G protein-coupled receptor 5 (LGR5) is a well characterized CSC marker in colon cancer.²⁹ Junttila *et al.* conjugated monomethyl auristatin E (MMAE; a potent microtubule inhibitor) or NMS818 (topoisomerase-inhibiting anthracycline PNU159682) to human LGR5 antibody. The anti-LGR5 ADC efficiently shrank tumor size and extended the survival of an aggressive *APC*^{min};*Kras*^{G12D} model due to the decrease of the CSC populations.²⁹ Besides, inhibition of mitochondrial oxidative phosphorylation (OxPhos) diminished CSC populations and overcame multidrug resistance in melanoma and pancreatic cancer.^{1,30,31}

Identified signaling pathways of CSCs have been facilitated for the development of CSC therapeutic strategies. The well-known CSC pathways are Notch, DLL-3, DDL-4, Wnt, STAT3, Hedgehog, FAK and Nanog.^{2,32,33} Some CSC signaling pathway-targeted therapies are currently

being evaluated in clinical trials. Among them, Hedgehog pathway inhibitor, Vismodegib, has received FDA approval and is in Phase II clinical trials for treating basal cell carcinoma (BCC).³⁴

Although tremendous research has been devoted to developing therapeutic tools targeting CSC regulators or signaling pathways, several concerns have surfaced concerning safety, efficacy, mutational process, and clinical impact. In the case of CSC-directed therapies, even the same type of cancer can display variability in CSC markers and signaling pathways. In other words, there is a lack of universal CSC-specific markers. Therefore, targeting every CSC in all patients is limited.³⁵ In addition, because expression of genes and signaling pathways of CSCs overlap with normal stem cells, these approaches may damage normal stem cells and induce mis-regulation of gene expression.^{3,36}

Since elimination of CSCs is still a challenging goal in conventional therapies, extensive research has been carried out to develop novel therapeutic strategies. The clinical field of hyperthermia therapy has been a focus due to its potency of direct cancer cell killing, radiosensitizer, and promotion of tumor reoxygenation.³⁷⁻³⁹ Increasing the temperature approximately greater than 41-50 °C halts cellular functions and causes cell death.⁴⁰ Hyperthermia therapy has shown advances in several cancers. Recently, clinical trials have clearly demonstrated that combined hyperthermia and radiation therapy and/or chemotherapy for treatment of recurrent melanoma, breast cancer, prostate cancer, cervix, head and neck cancer.^{38,41-54}

The efficiency of hyperthermia may also have a great potential to eliminate CSCs and sensitize them to conventional therapies, such as radiotherapy and chemotherapy. Activated heat shock protein by hyperthermia can trigger protein unfolding, thereby inducing cell death.⁵⁵ Stein *et al.* reported that the combination of hyperthermia and drug treatment abrogated drug resistance

of colon cancer by inactivation of ATP-driven efflux transporters, which are overexpressed in CSCs.⁵⁶ It has been studied that hyperthermia treatment can impede DNA damage repair pathway so that under the hyperthermia treatment, DNA damaging agent and/or radiotherapy can induce excessive DNA damage and can kill CSCs.^{57,58} Furthermore, hyperthermia can stimulate blood flow, resulting in a decrease of hypoxia. This re-oxygenation changes the microenvironment and decreases the number of quiescent CSCs.⁵⁹ Despite conventional hyperthermia therapy has been showing promising results to treat cancer and eradicate CSCs, there are only a few case of hyperthermia therapy in clinical practice possibly due to inadequate hyperthermia applicator tips and delivery systems. Thus, improved technology is necessary for making hyperthermia therapy possible to achieve therapeutic gain.

Comprehensive research of nanotechnologies has progressed and has identified nanoparticles, such as gold nanomaterials, iron oxide nanoparticles, and carbon-based nanomaterials, possessing unique capabilities to enable generation of heat in a desired site.⁶⁰⁻⁶³ Plasmonic gold nanomaterials have attracted more attention because they have shown a unique combination of thermal and optical properties. Plasmonic gold nanomaterials convert absorb light into heat, called the photothermal effect. With this consideration, gold nanomaterials with various shapes, such as gold nanorods, gold nanoshells, gold nanoprism, gold nanocages have been studied in the field of photothermal CSCs therapy.⁶⁴⁻⁶⁸ Atkinson *et al.* reported that gold nanoshell-mediated hyperthermia therapy can sensitize breast cancer stem cells to radiation therapy.⁶⁹

However, there exists limitation in CSC targeted nanomaterials-mediated photothermal therapies. This could be the lack of absolute biomarkers and the need for a combination of multiple markers to target the CSCs. For this reason, many studies have tried to deliver their nanomaterials

through an enhanced permeability and retention (EPR) effect, but this can also lead to side effects through non-specific targeting.^{65,69} In 2018, our research group have reported a synthetic ligand that selectively binds to CSC subpopulation over non-CSC subpopulation.⁷⁰ Through cell-based screening using on bead one compound library we identified the ligand. The ligand showed that it can selectively bind to CD24⁻/CD44⁺/ALDH⁺ CSC population of breast cancer cells, MCF-7 and MDA-MB-231. It is noteworthy that the ligand alone is sufficient to identify the CSC population, whereas the combination of multiple markers was required for it.⁷⁰

In this dissertation, CL-1-19-1 was employed to develop the novel strategy for CSC elimination. The AuNR conjugated with CL-1-19-1 and mPEG was explored its capacity *in vitro*. This AuNR exhibited high selectivity toward to ALDH⁺ subpopulation, considered CSCs. Under the nanosecond laser irradiation (532 nm), MCF cells showed more than 50% decreased number of ALDH⁺ cell populations versus control groups, suggesting that the #1-AuNR can selectively eliminate CSC subpopulation from pool of cancer cells.

2.2 Experimental section

2.2.1 Reagents and materials

We purchased citrated-coated gold nanorod (Peak λ 800 nm, 55 nm x 15 nm) from nanoComposix. *N,N*-Dimethylformamide (DMF), methanol (MeOH), acetonitrile (ACN), dimethyl sulfoxide (DMSO), *N*-Methyl-2-pyrrolidone (NMP), ethyl ether and dichloromethane (DCM) were all HPLC grade, and were purchased from Thermo Fisher Scientific. ALDEFLUORTM assay kit was purchased from STEMCELL Technologies. Citrate-stabilized gold nanorod was purchased from nanoComposix. Hoechst 33342 solution was purchased from BD

Pharmingen™. DMEM (Dulbecco's modified Eagle's medium), streptomycin-penicillin and L-glutamine were purchased from GE Healthcare HyClone. Methoxypolyethylene glycol thiol (mPEG-SH) (MW 1000) was purchased from Laysan Bio, Inc. 3-(4,5-Dimethylthiazol-2-yl)-2,5-Diphenyltetrazolium Bromide (MTT), Trifluoroacetic acid (TFA), N,N-diisopropylethylamine (DIPEA), and piperidine were obtained from Sigma-Aldrich. Fmoc-Cys(trt)-OH, Fmoc-Ser(tBu)-OH, Rink Amide MBHA resin (100-200 mesh) and 2-(1H-benzotriazol-1-yl)-1,1,3,3-tetramethyluronium hexafluorophosphate (HBTU) were purchased from Novabiochem. 1-hydroxybenzotriazole hydrate (HOBt·H₂O) was obtained from Creosalus. Biotech RC Dialysis tubing (20 KDa cutoff) was obtained from Spectrum Laboratories, Inc. Fetal bovine serum (FBS) was purchased from Atlas Biologicals. BCA assay kit was purchased from Thermo Fisher Scientific. We purchased primary antibodies of C-Myc, KFL4, Nanog, and Sox2 (Rabbit mAB) from Cell Signaling Technology. Ultrapure water (18.2 MΩcm, Millipore Co.) was used in all experiments.

2.2.2 Synthesis of ligands

CL-1-19-1 (#1) and control ligands were synthesized using Rink Amide MBHA resin (loading level 0.59 mmol/g). 1 g of RINK amide MBHA resin was swelled in 5 mL of DMF for 1 h and followed by deprotection with 20% piperidine (20% in DMF v/v). After a full wash 5 times with DMF, 2 times with MeOH, 2 times with DCM, and 3 times DMF, pre-mixed 5 equivalents of Fmoc-Cys(Trt)-OH, HOBt·H₂O, HBTU, and 10 equivalents of DIPEA in dry DMF were added in the resin and shaken at RT for 3 h. Resins were fully washed after each reaction and Fmoc deprotection step. Resins were deprotected with 20% piperidine and were shaken with pre-mixed

cocktail solution of Fmoc-6-Ahx-OH (6-(Fmoc-amino)caproic acid), HOBt·H₂O, HBTU, and DIPEA for 3 h. After the full wash, reactions of Fmoc-6-Ahx-OH and Fmoc deprotection were repeated twice. For peptoid sub-monomer addition, 2.84 mL of 0.4 M chloroacetic acid in dry DMF and 0.67 mL of 2 M *N,N'*-diisopropylcarbodiimide in dry DMF were added into resins, and resins were shaken at 35 °C for 6 min. Resins were washed with 3 times with DMF, 2 times MeOH, 2 times, DCM, and 3 times with NMP. 4 mL of 2 M Boc-1,4-diaminobutane in dry NMP was added to the beads and the beads were shaken at 35 °C for 3 h. After full wash, the resins were divided equally into 2 fritted cartridges. Afterward, peptoids were synthesized using the sub-monomer approach. The appropriate amine was added to resins (2 mL of a 2.0 M in NMP), and the reaction was performed at 35 °C for 1.5 h. After 7th amine addition, the peptoids were cleaved and deprotected in TFA solution (95% TFA, 2.5% TIS, 2.5% H₂O) for 2 h and additional 20 min with the fresh TFA cocktail solution. The resulting products were dissolved in acetonitrile and water with 0.1% TFA, and structures were analyzed by MALDI-TOF mass spectroscopy. Crude peptoids were purified by preparative HPLC (using C18 reverse phase column) and characterized by analytical HPLC and MALDI-TOF mass spectroscopy.

2.2.3 Preparation and characterization of the ligand-modified AuNRs

For the mPEG conjugation, 100 µL of 0.2 mg/mL of mPEG-SH in water was added to 1 mL of citrate-coated AuNRs (0.17 nM) with an average size of 55 nm x 15 nm (length x width), and the mixture was reacted for 6 h at RT. To remove unbound mPEG-SH, the solution was dialyzed in H₂O using a 20 kDa cutoff membrane by following the manufacturer's instructions. For the conjugation of peptoids on mPEGylated AuNRs, 10 µL of 5 mM peptoids (in DMSO) was

added to 1 mL of the purified mEPGylated AuNRs and mixed at RT for 24 h. After the conjugation, extra peptoids were removed by centrifuge at 4 °C with 4,500g for 30 min, and the AuNR pellet was resuspended in water.

Transmission electron microscopy (120 kV, JEOL, JEM-1400) was used to examine AuNR size and shape. A drop of the AuNR solution (0.2 nM) was deposited on a carbon-coated Cu grid and analyzed. Dynamic light scattering and ζ -potential (DLS, Nano-ZS, Malvern Instrument) were used to examine AuNR size and homogeneity. 0.2 nM of each AuNR in water was analyzed. UV-Vis spectra were measured using microplate reader (Synergy HTX, Biotek).

2.2.4 Cell lines

Human breast cancer cells, MCF-7 and MDA-MB-231 (from American Type Culture Collection) were cultured in a complete medium (DMEM (Dulbecco's modified Eagle's medium) with 10% fetal bovine serum (FBS), 1% streptomycin-penicillin, and 1% L-glutamine) at 37 °C with 5% CO₂.

2.2.5 Silver staining

12,000 cells MCF-7 and MDA-MB-231 were seeded in a 96-well plate. 24 h later cells were treated with AuNRs for 30 min at 37 °C with 5% CO₂. After 3 times washing with PBS (pH 7.4 1 mM MgCl₂ and 1mM CuCl₂), cells were fixed by adding 100 μ L of 4% formaldehyde solution and were incubated 10 min at RT. After removing the solution, the formaldehyde was quenched by incubating with 50 mM glycine solution in PBS (pH 7.4) for 5 min. The cells were rinsed with H₂O before LI silver enhancement reagents are applied.

To prepare the developer, we mixed equal amounts of the enhancer and initiator immediately before use. Silver precipitate was developed during 20 min and washed with H₂O 2 times. The stained AuNRs on cells were visualized a optical microscope.

2.2.6 Cell viability assay

To determine the effect of the AuNR-mediated hyperthermia on breast cancer cell viability, a 3-(4,5-dimethylthiazol-2-yl)-2,5-diphenyltetrazolium bromide (MTT) assay was performed. For MTT assay, 15,000/well MCF-7 cells were seeded on 96 well plate and cultured for 24 h. The cells were treated with varying concentration (0.025 – 0.4 nM) of the AuNRs for 30 min at 37 °C with 5% CO₂. After 3 times washing with PBS (pH 7.4, 1 mM MgCl₂, and 1mM CuCl₂), the cells in PBS were irradiated by a nanosecond laser pulses, which is operated at 532 nm from a ND:YAG laser (Quantel Q-smart). The duration of single laser pulse is 6 ns laser pulse with a Gaussian profile (100 mJ cm⁻²) and the repetition rate is 10 Hz. After 10 laser pulses exposure, PBS was exchanged with 100 μL of phenol red-free complete medium then cultured the cells 24 h. 10 μL of MTT reagent (5 mg/mL) was added to each well, including controls and placed the plate in cell culture incubator for 3 h. Afterward, 100 μL of 10% SDS in 0.01 M HCl (solubilization solution) was added to each well to dissolve formazan. The plate was incubated in cell culture incubator for 4 h to allow the purple formazan crystals to be dissolved in the solution. The absorbances of product were read at 590 nm using microplate reader.

2.2.7 In situ ALDEFLUOR assay

To assess the effect of the AuNR-mediated hyperthermia on elimination of breast cancer stem cell population, the ALDEFLUOR™ assay was performed. 70 μ L of MCF-7 cell suspension (15,000 cells) on middle of glass bottom dishes (35 mm). Following the incubation for 90 min in cell culture incubator to allow the cells to seed on the plate, 1 mL of the complete medium was added to the dishes. After the cell growth reached 70% confluence, the culture medium was replaced with fresh medium containing 0.2 nM #1-AuNR or Ctrl-AuNR. After incubation in cell culture incubator for 30 min, unbound AuNRs were washed out using PBS (pH = 7.4, 1 mM CuCl_2 and 1 mM MgCl_2) 3 times. The cells were irradiated by nanosecond laser and subsequently the PBS was replaced by fresh medium. The cells were maintained for 3 h at 37 °C with 5% CO_2 . We stained the cell nucleus with Hoechst 33342 for 30 min, in the meantime, ALDEFLUOR™ substrate (BAAA) was prepared. 800 μ L of ALDEFLUOR™ assay buffer was added to the microtube where 4 μ L of ALDEFLUOR™ substrate was placed on. 200 μ L of the mixed solution was immediately transferred to another microtube containing 1 μ L of diethylaminobenzaldehyde (DEAB) reagent, which is a commonly used as selective inhibitor of aldehyde dehydrogenase isoenzymes. After staining of cell nucleus, the cells were washed with PBS 2 times and incubated with 70 μ L of ALDEFLUOR™ substrate solution or the substrate solution including DEAB for 45 min at 37 °C. The stained cells were then washed with cold ALDEFLUOR™ assay buffer 2 times and kept dishes on the ice with 1 mL of ALDEFLUOR™ assay buffer until obtaining laser scanning confocal fluorescence images.

2.2.8 Isolation of breast CSCs using FACS

A single cell suspension was prepared for the ALDEFLUOR™ assay by following manufacturer's protocol with minor modifications. Briefly, when the MCF-7 cells growth reached 80% confluence in T75 flask, the cells were detached using trypsin. After washing the cells with Dulbecco's phosphate-buffered saline (DPBS) 2 times, the cells were suspended in ALDEFLUOR™ assay buffer. To obtain a uniform single cell suspension, the cells were passed through a cell strainer (40 μm) 4 times. After determining the cell density, 1 mL of suspension (10^6 cells/mL) in ALDEFLUOR™ assay buffer was prepared. For preparation of negative control, 5 μL of ALDEFLUOR™ substrate was added to the suspension and 0.5 mL of cell suspension was immediately transferred to another tube containing 5 μL of DEAB, which was used to determine the baseline of fluorescence to distinguish the ALDH⁺ and ALDH⁻ population. The tubes were incubated at 37 °C for 45 min, following washing with cold ALDEFLUOR™ assay buffer. ALDH⁺ population and ALDH⁻ population were sorted using FACS.

2.2.9 Western blot analysis

After incubation with each AuNR for 30 min, the MCF-7 cells on 35 mm glass bottom dish were exposed to nanosecond laser, which was identical with the condition for MTT assay and in situ ALDEFLUOR assay. Subsequently, PBS was replaced by the fresh complete medium, and the cells were maintained in cell culture incubator for 24 h. Following washing the cells with DPBS 2 times, cell lysates were prepared by directly adding the Triton X-100 lysis buffer (50 mM Tris, 150 mM NaCl, pH 8.0, 1% Triton X-100, protease inhibitor mixture) to the cells. After 30 min incubation on the ice, lysates were vortexed for 1 min and centrifuged at 12,000 g for 10 min at 4

°C. Bicinchoninic acid (BCA) assay was conducted to measure the protein concentration, and equal concentration of samples was prepared. After boiling the lysate with sample buffer at 100 °C for 5 min, equal volume of samples was loaded on a 10% sodium dodecyl sulfate/polyacrylamide gel electrophoresis (SDS/PAGE) gel. After the protein separation, the gel was transferred to polyvinylidene fluoride (PVDF) membrane for 1 h. Subsequently, the membrane was blocked with 5% milk in tris-buffered saline with Tween[®] 20 (TBS-T) for 1 h. The primary antibodies (1:1000 dilution in TBS-T including 5% bovine serum albumin (BSA)) were incubated with the membranes overnight at 4 °C. After 3 times washing with TBS-T, secondary antibody (1:1500 dilution) in 5% milk was incubated for 1 h at RT. Following washing unbound secondary antibodies with TBS-T 3 times, the proteins were then detected for chemiluminescent signal using 1:1 mixture of SuperSignal[™] West Femto Maximum Sensitivity Substrate and ECL Western Blotting Substrate (Thermo Scientific).

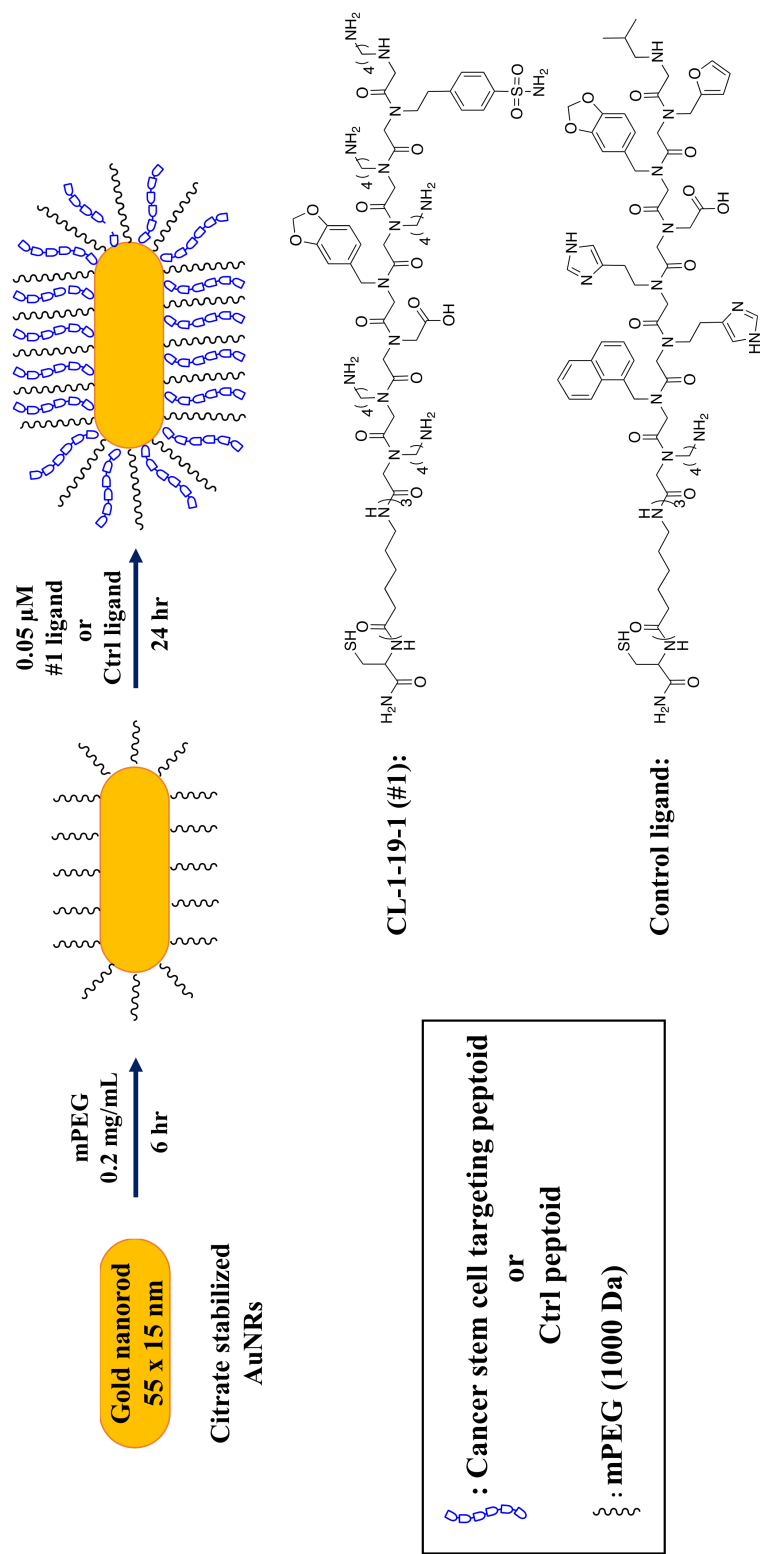
2.2.10 Two-photon luminescence imaging

16,000 MCF-7 cells were seeded on 35 mm glass bottom dish and were grown in cell culture incubator to 75% confluency. The medium was replaced with a pre-prepared fresh complete medium containing #1-AuNR and incubated for 30 min in cell culture incubator. Unbound AuNRs were washed using PBS (pH = 7.4, 1 mM CaCl₂ and 1 mM MgCl₂) 3 times. The imaging was performed using Olympus MPE-RS TWIN microscope with a femtosecond Ti-sapphire laser (InSight DS-OL) with a 40x water immersion objective lens with excitation at 850 nm wavelength. 0.65 mW of excitation power was used for obtaining images. Luminescence signal was detected in red and green channel. X and Y dimensions of images are 318.2 μm for each.

2.3 Result and discussion

2.3.1 Preparation and characterization of AuNRs

Because citrate is known to be less toxic to cells and animals than CTAB, citrate-coated AuNR having maximum localized surface plasmon resonance at 808 nm was employed as the starting AuNR.⁷¹ The procedure for the preparation of ligand-conjugated AuNRs is showed in Scheme 2.1. To improve biocompatibility, we conjugated mPEG on the AuNR surface by ligand exchange. According to the calculation of ligand coverage per gold nanoparticle's surface,⁷² 0.02 mg/mL of mPEG could occupy 30% of 2,590 nm² AuNR's surface. AuNRs modified with varying concentrations of mPEG (from 0.01 to 0.2 mg/mL) were mixed with 0.2 M NaCl to find the optimal concentration for dual conjugations on the surface. Although all AuNRs with different concentrations of mPEG exhibited excellent stability in high salt solution, we have selected 0.02 mg/mL of mPEG to save the space for #1-ligand conjugation (Figure 2.1 a). Afterward, we conjugated them with CSC targeting #1-ligand. In this study, we synthesized #1 ligand containing thiol in cysteine at N-terminal, allowing a strong interaction with the surface of AuNR. Additionally, the #1 ligand contains spacers between the cysteine and the binding ligand. The presence of spacers could allow for an increase in the accessibility to a binding site. To find optimal concentration of #1-ligand, we added varying amount of #1-ligand to mPEGylated AuNRs. After #1-ligand modification, ζ -potential were change from negative to positive due to the existence of primary amine in #1-ligand (Figure 2.1 b). Since we obtained highest positive charge from 0.05 mM #1 ligand, we chose this concentration as an optimal condition. We applied this condition to the synthesis of control ligand-conjugated AuNR (Ctrl-AuNR). We observed that resulting AuNRs maintained their stability in high salt solution (Figure 2.1 c and d).



Scheme 2.1. Schematic illustration of the ligand-conjugated AuNRs preparation procedure.

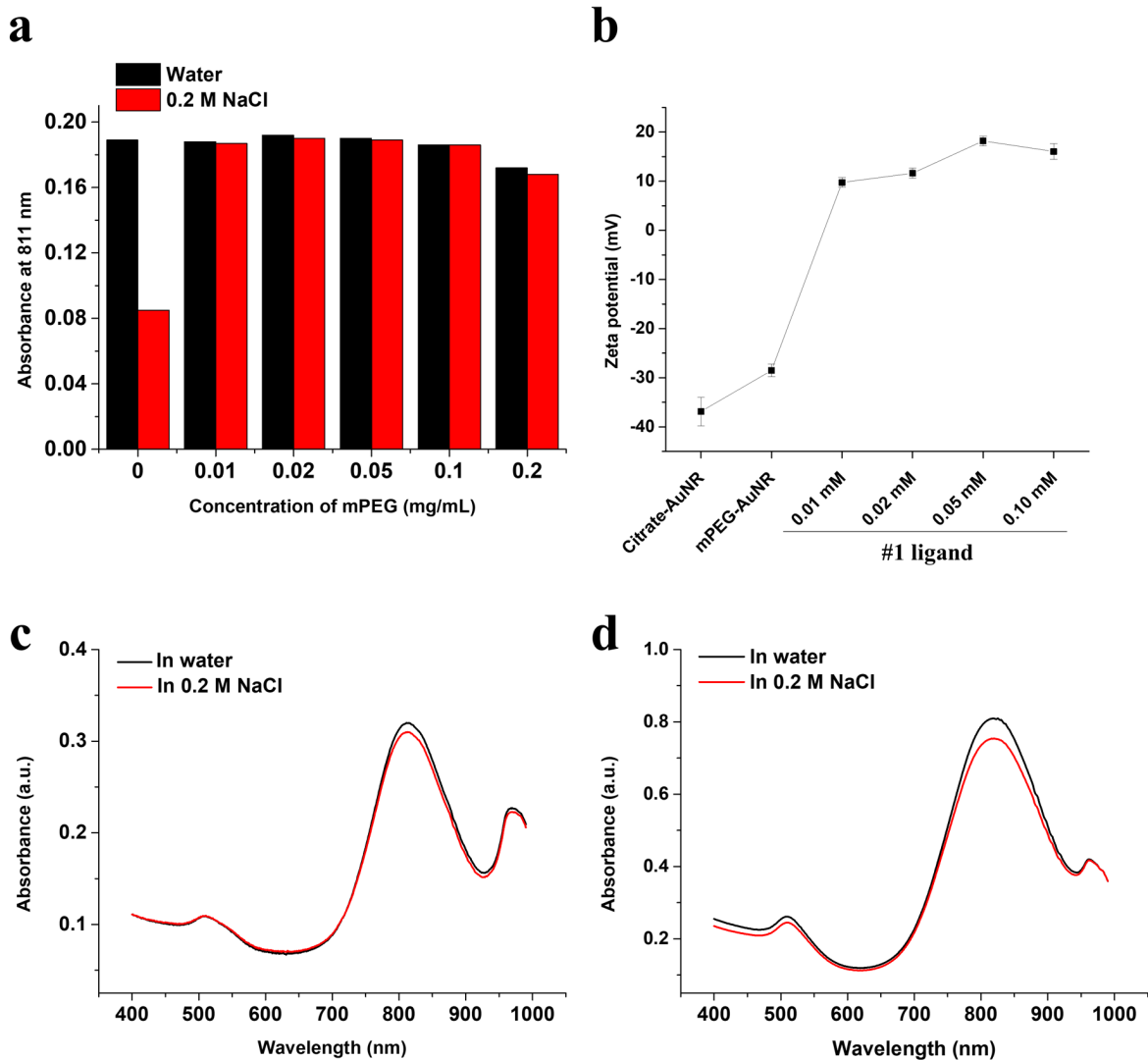


Figure 2.1. Optimization of ligand concentrations and stability of AuNRs in high salt solution. (a) Stability of AuNRs with different concentration of mPEG in 0.2 M NaCl solution. (b) ζ -potential values after/before conjugation and mPEGylated #1-AuNRs with different concentration of #1 ligand. Stability of #1- (c) and Ctrl-AuNRs (d) in 0.2 M NaCl solution, respectively.

The longitudinal surface plasmon resonance red shifted in UV-Vis spectra (Figure 2.2 a and Table 2.1), because the ligand conjugation changed the dielectric constant of the surrounding environment of AuNRs.⁷³ Compared to #1-ligand, Ctrl-ligand has less number of primary amine,

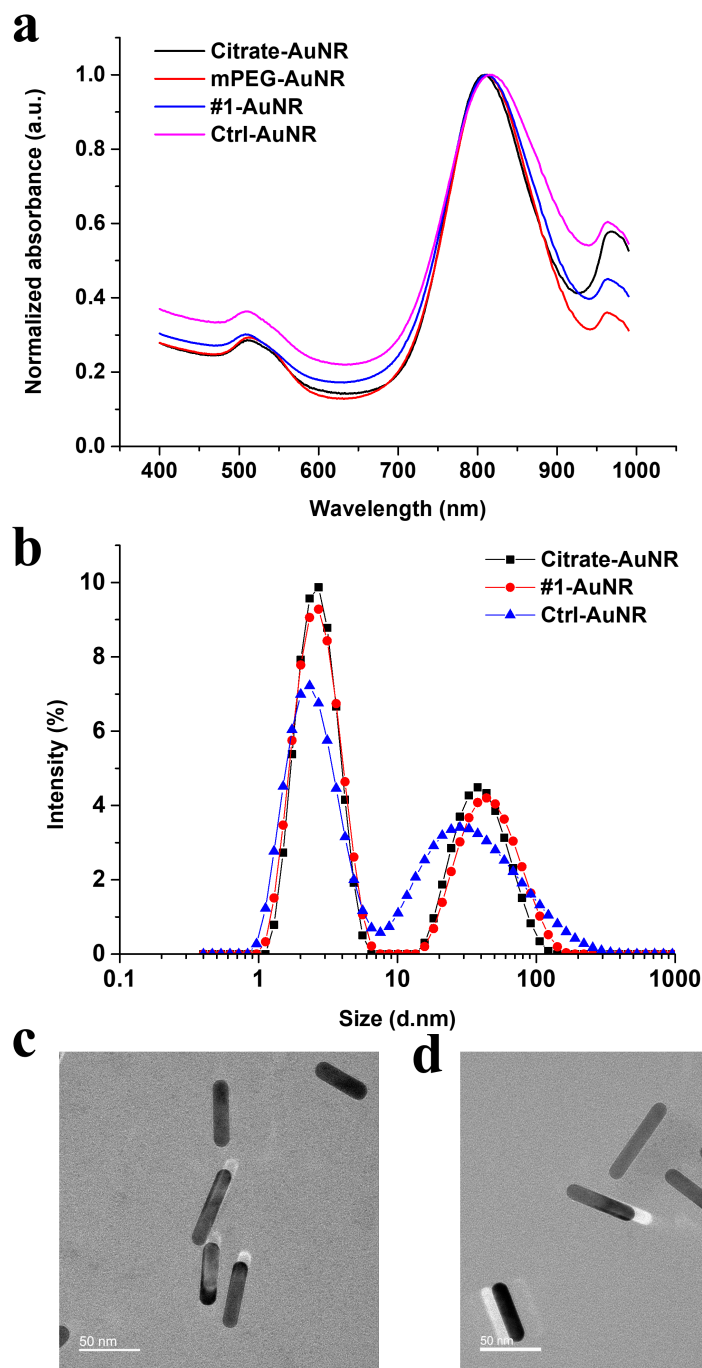


Figure 2.2. Characterization of AuNRs. (a) UV-Vis spectra of AuNRs with different ligand conjugations. Each absorption peak was normalized to the maximum absorbance value. (b) Hydrodynamic diameter distribution of AuNRs before and after conjugation with #1 and Ctrl ligands. (c) and (d) TEM images of #1- and Ctrl-AuNRs, respectively.

Table 2.1. Summary of wavelength at maximum OD and ζ -potential with different surface

AuNRs	Wavelength at Maximum OD (nm)	Zeta potential (mV)
Citrate-AuNRs	808	-36.87 \pm 2.90
mPEG-AuNRs	811	-28.53 \pm 1.27
#1-AuNRs	812	11.37 \pm 1.45
Con-AuNRs	815	1.30 \pm 0.62

resulting in a neutral ζ -potential (Table 2.1). As-prepared AuNRs sustained good stability in aqueous condition (Figure 2.2 b) and consistent physical shape after modification (Figure 2.2 c and d).

2.3.2 Cell binding study

The binding ability of #1-AuNR was then evaluated in breast cancer cells. Silver enhancement reagent was employed to visualize AuNR in cells. The identical conditions of silver staining were applied to MDA-MB-231 and MCF-7 cell lines. In Figures 2.3 b and e, the blue dots indicate positions where the AuNRs are present. It observed that MDA-MB-231 and MCF-7 cells treated by #1-AuNR showed blue dots under the microscope. On the contrary, only negligible number of blue dots was observed in the cell treated with the Ctrl-AuNRs. In addition to silver staining, we also conducted two-photon luminescence microscope in MCF-7 by utilizing intrinsic two-photon-induced photoluminescence of AuNR to investigate intact binding distribution of AuNRs. The strong luminescence of AuNR was observed at a power as low as 0.65 mW without

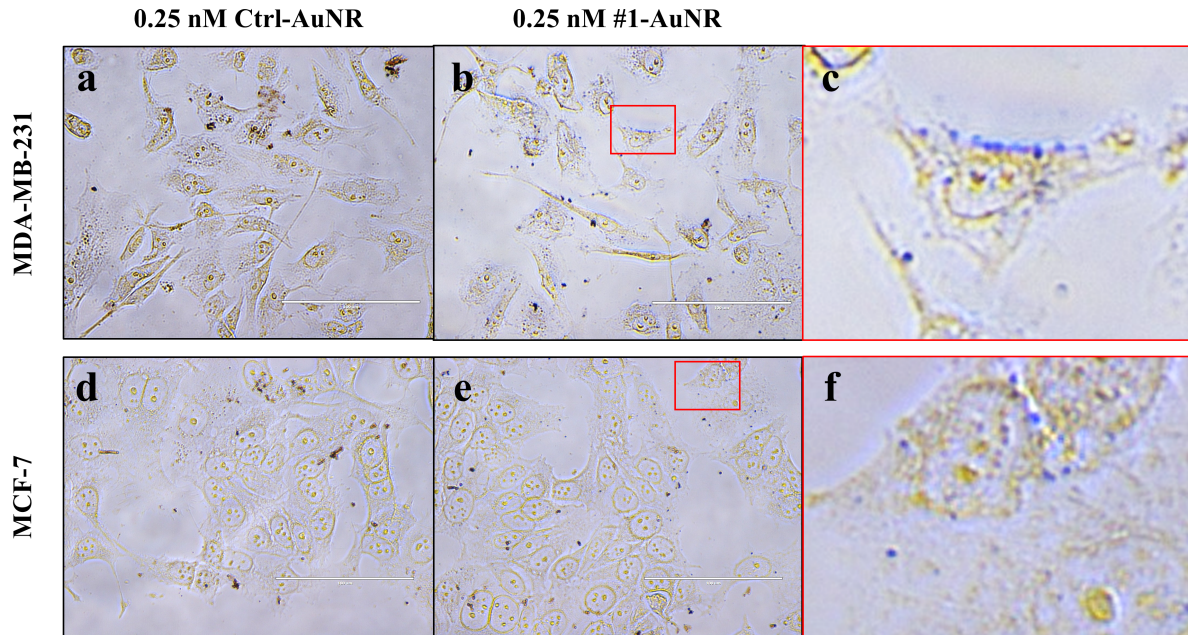


Figure 2.3. Binding distribution of AuNRs in breast cancer cells. MDA-MB-231 (a, b, and c) and MCF-7 (d, e, and f). Images of cells treated with 0.25 nM Ctrl-AuNR (a and d) and #1-AuNR (b and e). Red box is zoom-in images of cells treated with #1-AuNR (c and f). Blue dot is corresponding the position of AuNR.

autofluorescence, which can be detected above 0.6 mW (Data not shown). In accordance with the result of silver enhancement staining, the cells treated by #1-AuNR showed high density of AuNR but not in Ctrl-AuNR (Figure 2.4).

2.3.3 Cytotoxicity of AuNR mediated hyperthermia

To examine the photothermal effect of AuNRs on the elimination of CSCs, we employed a nanosecond pulse laser because pulsed radiation generates high heat bubble formation and following cavitation within nano- and microscale causing single cell ablation. According to Ungureanu *et al.* a laser illumination at longitudinal plasmon absorption peak between 650 and 950 nm did not result in lethal damage to the cells because the thermal reshaping of AuNRs is

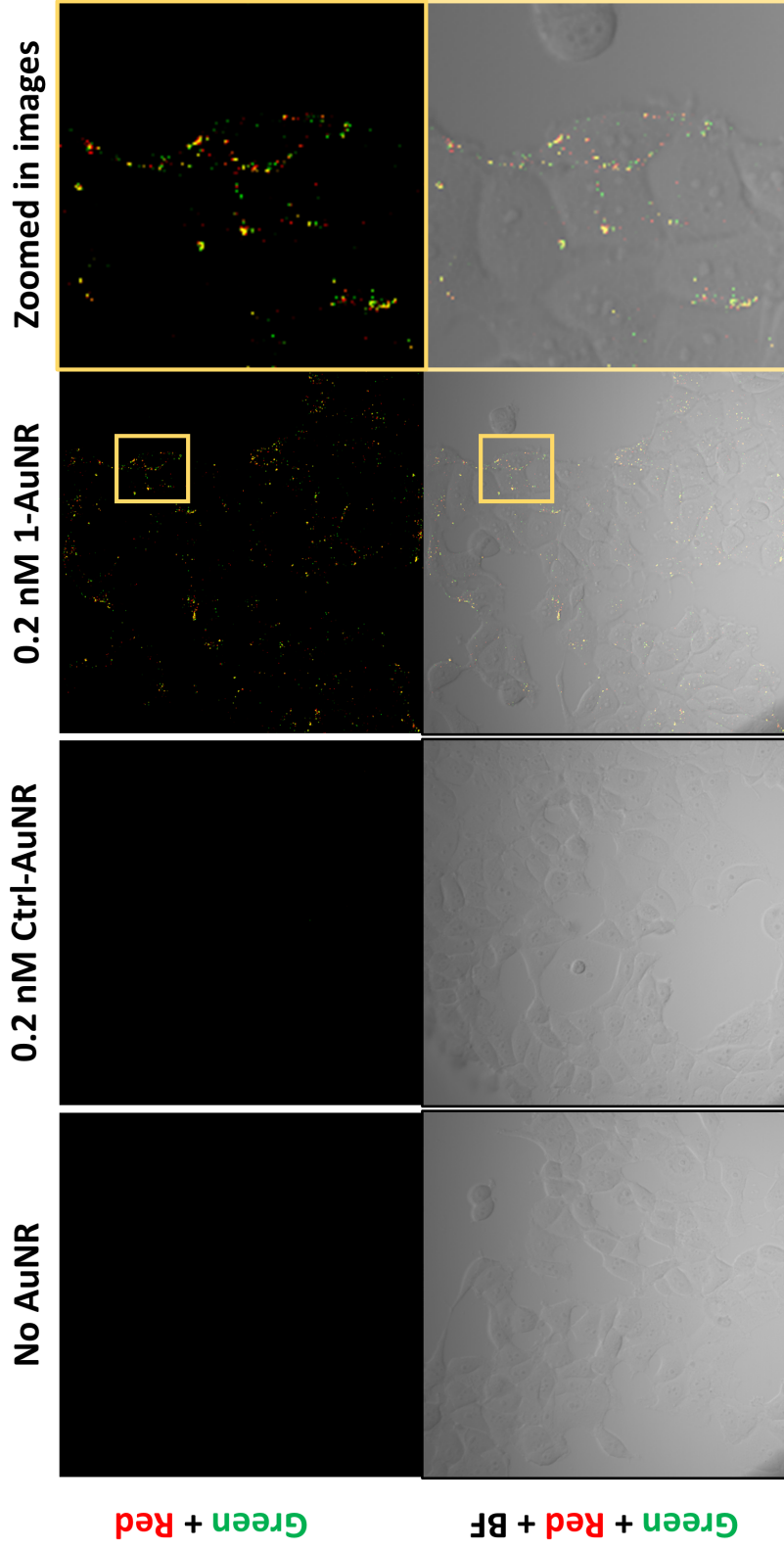


Figure 2.4. Intact cell binding distribution of AuNRs in MCF-7. Two-photon luminescence images of cells treated with ctrl, 0.2 nM Ctrl- and #1-AuNRs. Luminescence of AuNR is green, red and yellow colors.

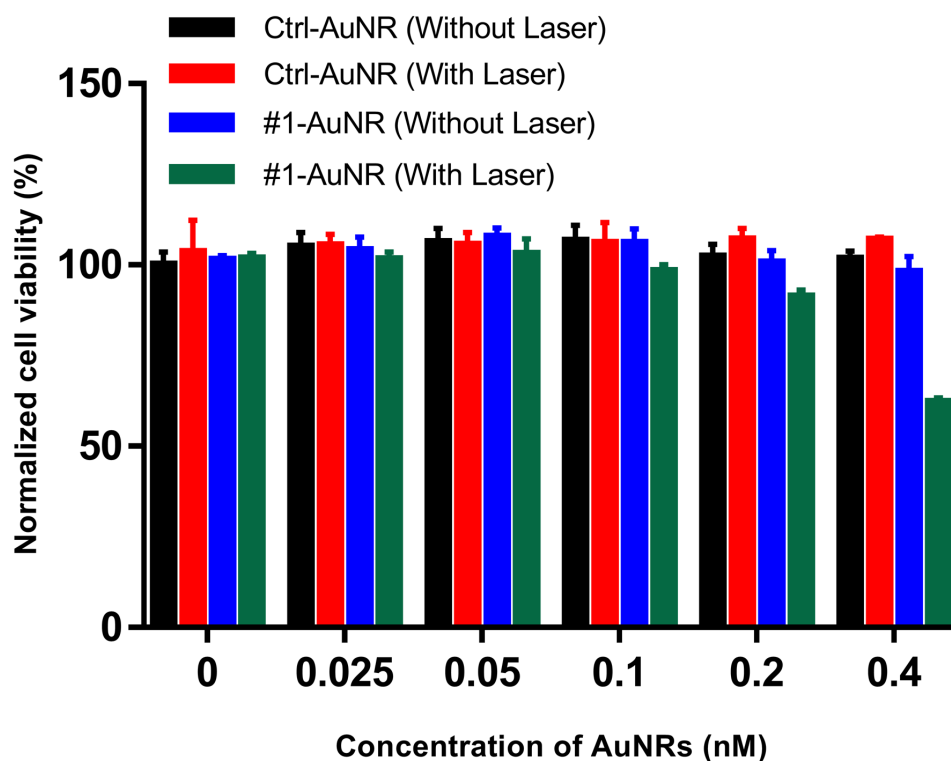


Figure 2.5. Effect of the AuNR-mediated hyperthermia on cell viability. MCF-7 cells after 24 h of laser irradiation or non-irradiation. The cells incubated with increasing concentration of AuNRs (0-0.4 nM). Error bars indicate standard deviation of three samples.

occurred in 100 ps resulting in which laser pulse will no longer be absorbed by the AuNRs.⁷⁴ On the contrary, green laser, the transverse peak (532 nm), caused the cell-death with moderate change of shape. Based on these results, we decided to utilize a nanosecond pulsed laser at 532 nm at 100 mJ cm⁻² per pulse to investigate the photothermal treatment of the CSCs mediated by AuNRs.

We performed MTT assay to examine whether the laser irradiation condition is sufficient to kill the cells. For this, the MCF-7 cells after incubation with different concentrations of #1-AuNR or Ctrl-AuNR (equal to 0.025, 0.05, 0.1, 0.2, and 0.4 nM) were irradiated by nanosecond laser. We also contained non-irradiation control groups to examine the cytotoxicity of AuNRs. Irradiated and non-irradiated cells were maintained with fresh medium for 24 hr. We observed that the cells

treated by only higher concentrations of #1-AuNRs (0.2 and 0.4 nM) with laser irradiation decreased viable cells by 8.7% and 37.8% respectively, whereas other groups did not show any cell death (Figure 2.5). These results are indicating that the condition of laser irradiation is suitable to kill cells and AuNRs themselves do not have a cytotoxicity. Thus, considering that the population of cancer stem cells in MCF-7 cells is around 2%, the cell death of 8% from treatment of 0.2 nM #1-AuNR was determined to be the optimal concentration for the elimination of cancer stem cells with minimized non-specific cell death.

2.3.4 Targeting ability of #1-AuNR to CSCs

Next, we designed the experiment to validate that #1 ligand still maintains CSC targeting activity even on the surface of AuNR. If it does, the AuNRs will be able to bind selectively to the CSC subpopulation than non-CSC subpopulation. For this, we isolated ALDH⁺ (aldehyde dehydrogenase) subpopulation, which has been identified as cancer stem cells, being capable of self-renewal and of initiating tumor growth.⁸ For isolating ALDH⁺ subpopulation, MCF-7 cells were stained using ALDELFUORTM assay, and ALDH⁺ subpopulation was sorted via FACS. As shown in Figure 2.6 b, population of ALDH⁺ was 1.8 % in MCF-7 cells, which is consistent with previous studies.^{65,75} To confirm whether sorted subpopulation is cancer stem cell population, we conducted Western blot analysis to see the expression of cancer stem cell markers (Figure 2.6 b). Levels of KLF4 and Nanog were much higher in ALDH⁺ subpopulation than whole MCF-7 population and ALDH⁻ subpopulation, which is also consistent with previous studies.⁷⁵ After sorting the ALDH⁺ and ALDH⁻ subpopulations, each populations including whole MCF-7 cells (16,000 cell per dishes) were seeded on 35 mm glass bottom dishes and incubated for 12 h at 37

°C. Afterward, the cells were incubated with 0.2 nM AuNR for 30 min, and two photon luminescence images of each sample were obtained. The highest density of #1-AuNRs was observed in the ALDH⁺ cells. In contrast, the ALDH⁻ cells and whole MCF-7 cells showed very few luminescence signal (Figure 2.7 a). To quantify the fluorescence signal of each sample, the area occupied with AuNRs was divided by cell surface area in each image using imageJ software, and the values were normalized to the value of whole MCF-7. The ALDH⁺ cells had more than 9

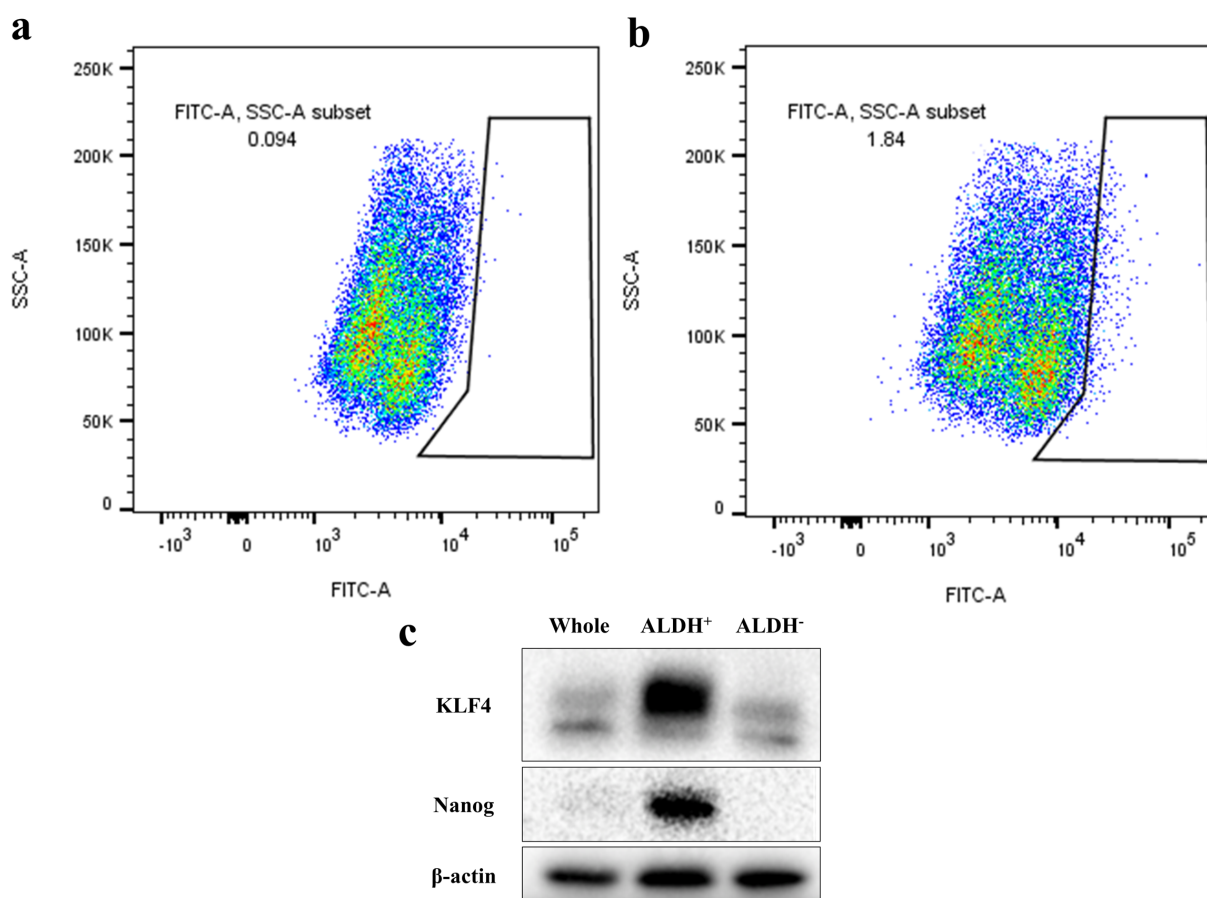


Figure 2.6. FACS analysis of ALDH⁺ subpopulation in MCF-7 cells using the ALDEFLUOR™ assay. (a) FACS analysis MCF-7 cells treated by DEAB, aldehyde dehydrogenase inhibitor (negative control). This sample was used to establish the baseline of FITC fluorescence to determine the region for ALDH⁺ subpopulation. (b) FACS analysis of MCF-7 cells treated by ALDELFUOR substrate (BAAA). (c) Western blotting analysis of expressions of stemness transcription factors in MCF-7 whole population, sorted ALDH⁺ and ALDH⁻.

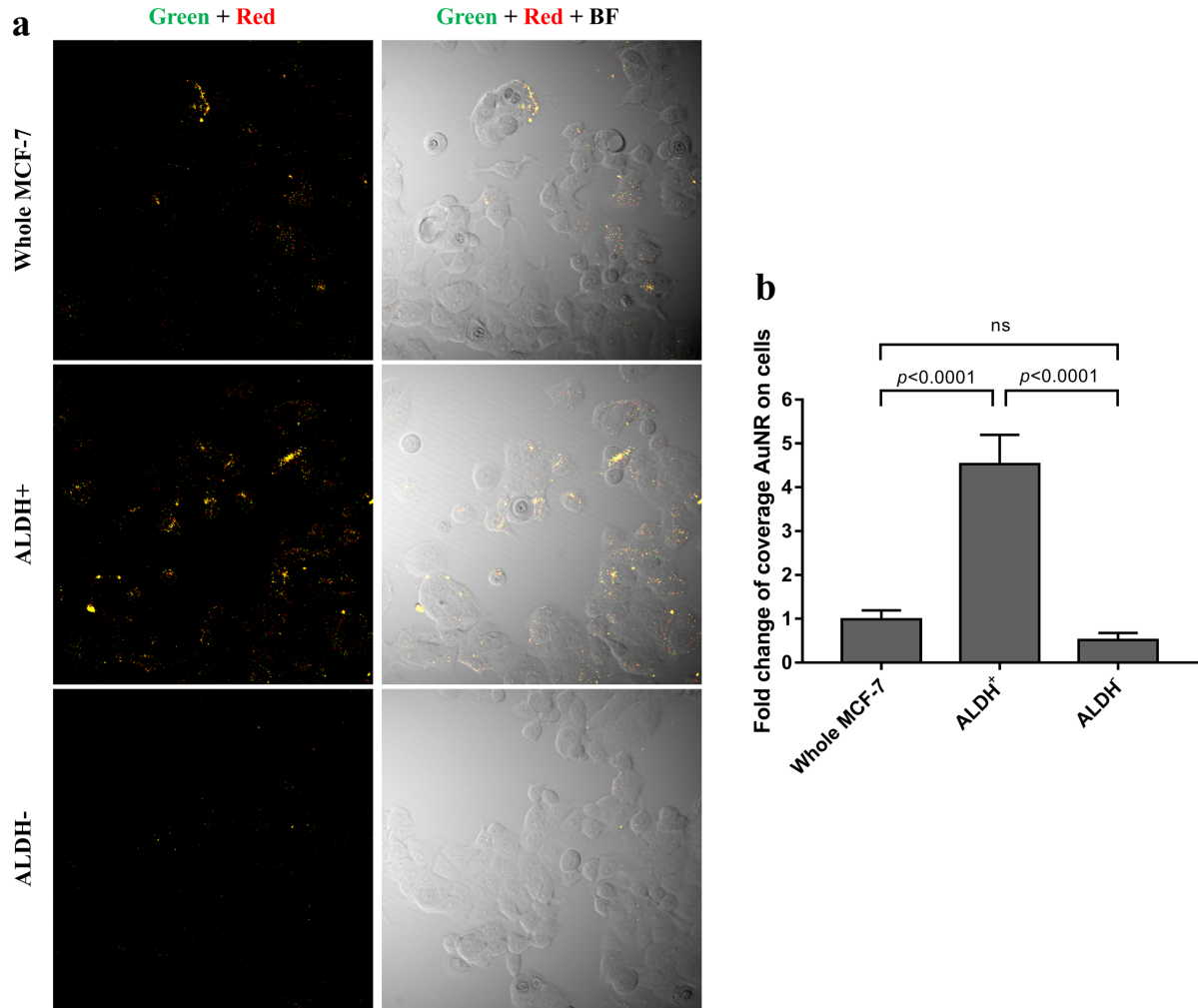


Figure 2.7. Examination of selectivity of #1-AuNR toward CSCs. (a) Two-photon luminescence images of whole-MCF-7, ALDH⁺ and ALDH⁻ subpopulation after incubation with 0.2 nM #1-AuNRs. (b) Quantification of the AuNR on cell surface. Error bars indicate standard deviation from 8 different locations in two samples. Statistical significance was evaluated using ANOVA. ns = not significant.

times the AuNRs than the ALDH⁻ cells. In the case of whole MCF-7 cells, 2 times more AuNRs were detected than ALDH⁻ cells, and 5 times less AuNRs were observed than the ALDH⁺ cells (Figure 2.7 b). Thus, it is noteworthy that this noble of AuNR can be suitable mediator for photothermal therapy of CSCs.

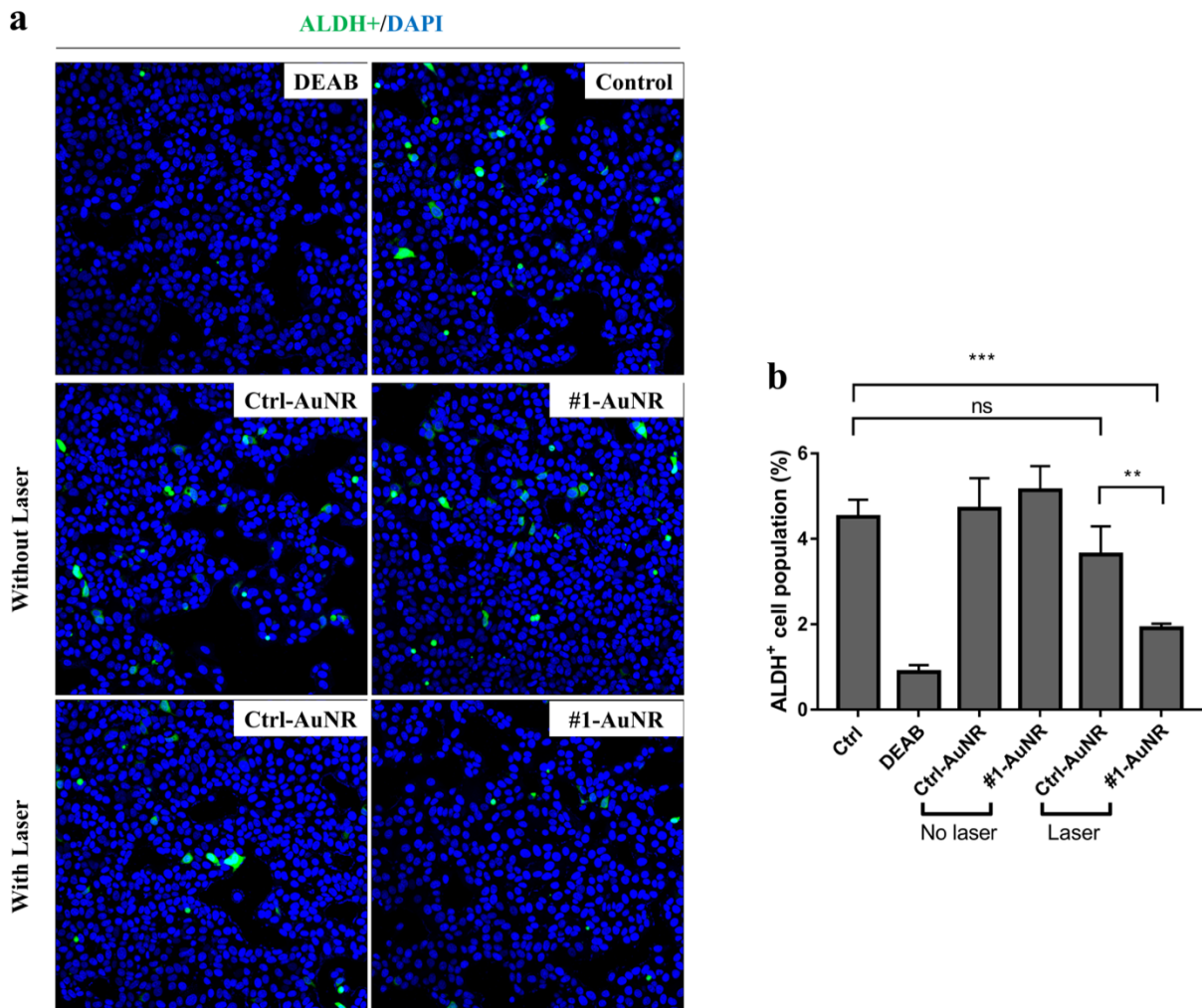


Figure 2.8. Analysis of CSC subpopulation in MCF-7 under the AuNR-mediated hyperthermia via in situ ALDELFUOR assay. (a) Laser scanning confocal microscope images of MCF-7 cells treated with Ctrl- and #1-AuNR with or without laser irradiation. (b) Quantification of ALDH⁺ subpopulation in each group (**P = 0.001, ***P < 0.001, ns = not significant).

2.3.5 Effect of the AuNR-mediated hyperthermia on CSC

To evaluate the hyperthermia effect of AuNR on CSCs, we conducted in situ ALDELFUORTM assay for visualizing CSCs in six different groups (cells only, cells-laser, Ctrl-AuNR, Ctrl-AuNR-laser, #1-AuNR, #1-AuNR-laser). As shown in Figure 2.8 a, the validity of

CSCs labeling by ALDEFLUOR™ assay kit was confirmed by observing diminished green fluorescence upon treatment of DEAB. Fluorescence images in Figure 2.8 a demonstrated that Ctrl-AuNR or laser irradiation itself does not affect the fate of CSCs, whereas following treatment of #1-AuNRs and laser irradiation, the CSCs population in the cells was dramatically decreased versus the control groups. To quantify the number of ALDH⁺ cells, we counted ALDH⁺ cells and DAPI-stained cells, and then we divided ALDH⁺ cell by total number of cells in each image. The ALDH⁺ cell population is around 4% in the control group, which are higher than the result from FACS analysis because FACS excludes small particles that cannot pass the threshold such as cell debris, cell doublets, and dead cells. We observed that the ALDH⁺ cells were decreased by > 50% in #1-AuNR-laser group versus control group (Figure 2.8 b). We also carried out Western blot analysis to assess CSC associated transcription factors, KLF4, c-Myc, Nanog and Sox2 after treatments. The results showing in Figure 2.9 are very correlated with the result of ALDEFLUOR™ assay. Taken together, the results indicate that #1-AuNR-mediated photo-induced hyperthermia affects the fate of CSCs.

2.4 Conclusions

In summary, we have successfully designed and fabricated cancer stem cell-targeting AuNR by conjugating the #1 ligand identified from high-throughput screening. The resulting AuNR possess high selectivity toward CSCs population and the capacity to serve as mediator photothermal treatment upon irradiation of nanosecond laser. Our results demonstrate that the #1-AuNR selectively binds to ALDH⁺ subpopulation, which is considered as CSCs population and upon the laser irradiation the heat generated from the AuNR diminished CSC population. Furthermore,

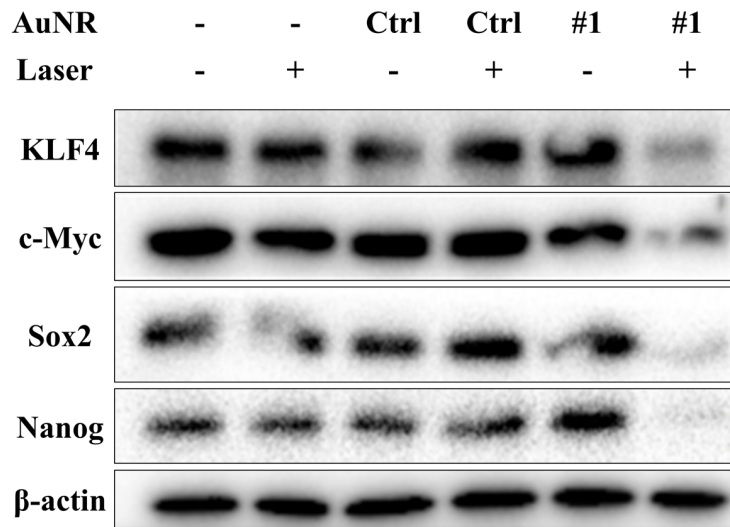
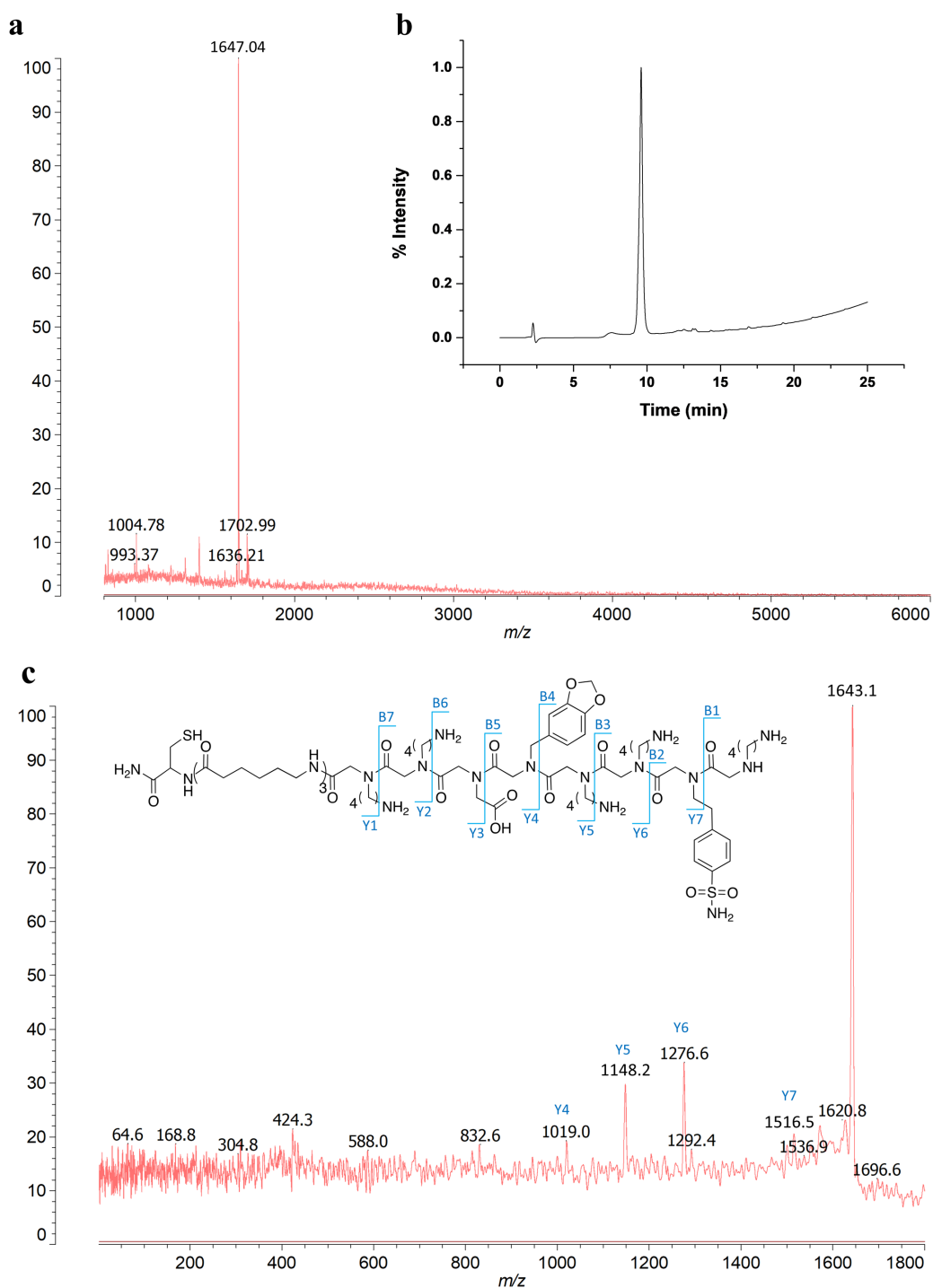


Figure 2.9. Effect of AuNR-mediated hyperthermia on expression of stemness-associated transcription factors. Western blot analysis of CSC-associated transcription factors in MCF-7 cells treated with or without AuNRs and with or without laser irradiation.

levels of proteins that closely related with stemness of cancer were significantly decreased after #1-AuNR mediated heat treatment. Taken together, this study introduced a novel therapeutic potential of the AuNR-mediated hyperthermia treatment in elimination of breast CSCs. We believed that in combination with conventional chemo- or radio-therapy, this novel nanotherapeutic system could lead to significant reduction of metastasis, recurrence, and resistance of cancer.

2.5 Supplementary information



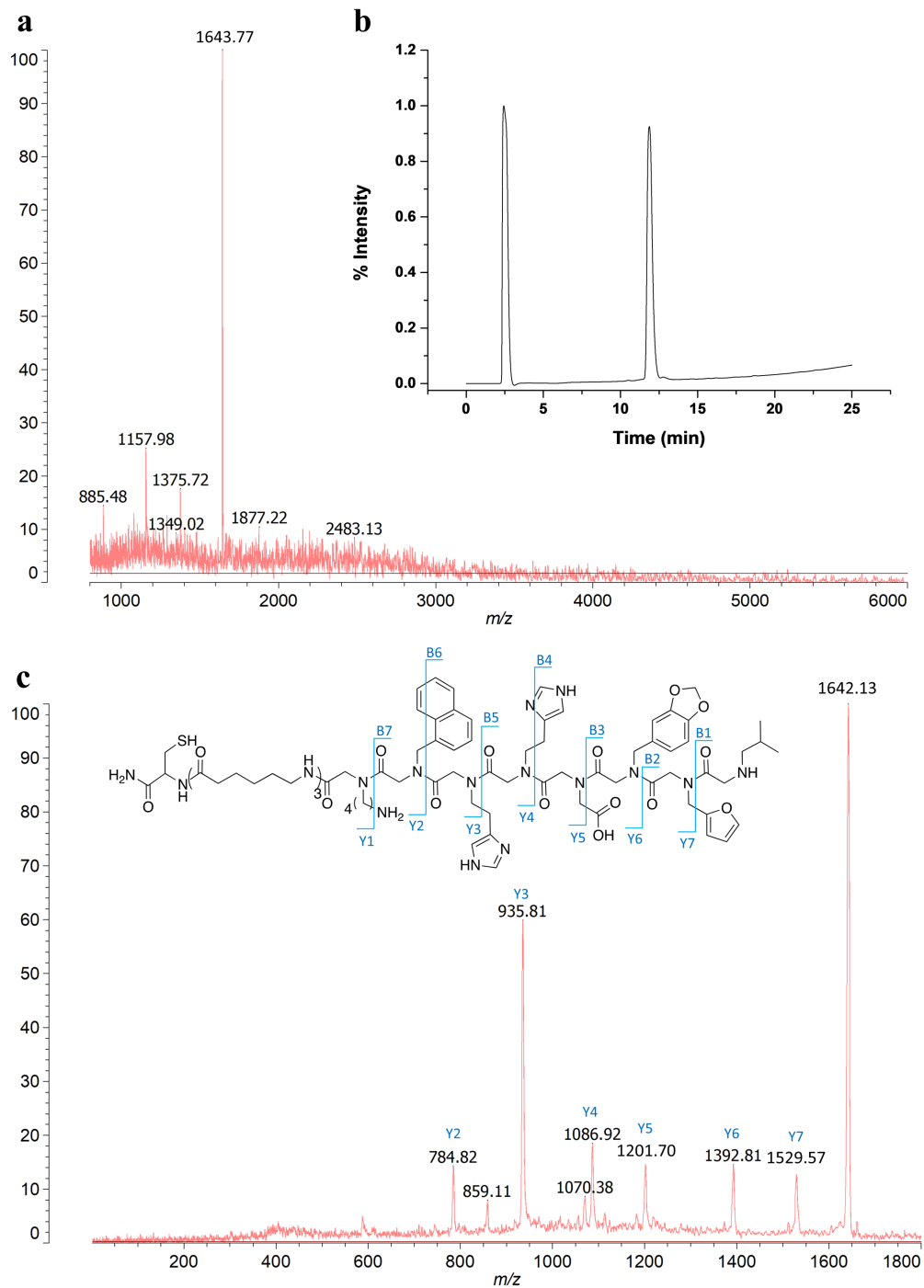


Figure S.2.2. Characterization of the Ctrl ligand. (a) MALDI-TOF data of the Ctrl ligand. (b) Analytical HPLC chromatogram of the Ctrl ligand. (c) Sequence analysis of the Ctrl ligand.

2.6 References

- (1) Sancho, P.; Burgos-Ramos, E.; Tavera, A.; Kheir, T. B.; Jagust, P.; Schoenhals, M.; Barneda, D.; Sellers, K.; Campos-Olivas, R.; Graña, O.; Viera C. R.; Yuneva, M.; Sainz, B. Jr.; Heeschen, C. MYC/PGC-1 α Balance Determines the Metabolic Phenotype and Plasticity of Pancreatic Cancer Stem Cells. *Cell Metab.* **2015**, *22*, 590–605.
- (2) Borah, A.; Raveendran, S.; Rochani, A.; Maekawa, T.; Kumar, D. S. Targeting Self-Renewal Pathways in Cancer Stem Cells: Clinical Implications for Cancer Therapy. *Oncogenesis* **2015**, *4*, 1–11.
- (3) Batlle, E.; Clevers, H. Cancer Stem Cells Revisited. *Nat. Med.* **2017**, *23*, 1124–1134.
- (4) Ye, X.; Tam, W. L.; Shibue, T.; Kaygusuz, Y.; Reinhardt, F.; Ng Eaton, E.; Weinberg, R. A. Distinct EMT Programs Control Normal Mammary Stem Cells and Tumour-Initiating Cells. *Nature* **2015**, *525*, 256–260.
- (5) Bonnet, D.; Dick, J. E. Human Acute Myeloid Leukemia Is Organized as a Hierarchy That Originates From a Primitive Hematopoietic Cell. *Nat. Med.* **1997**, *3*, 730–738.
- (6) Al-Hajj, M.; Wicha, M. S.; Benito-Hernandez, A.; Morrison, S. J.; Clarke, M. F. Prospective Identification of Tumorigenic Breast Cancer Cells. *Proc. Natl. Acad. Sci. U.S.A.* **2003**, *100*, 3983–3988.
- (7) Dontu, G.; Abdallah, W. M.; Foley, J. M.; Jackson, K. W.; Clarke, M. F.; Kawamura, M. J.; Wicha, M. S. In Vitro Propagation and Transcriptional Profiling of Human Mammary Stem/Progenitor Cells. *Genes Dev.* **2003**, *17*, 1253–1270.

- (8) Ginestier, C.; Hur, M. H.; Charafe-Jauffret, E.; Monville, F.; Dutcher, J.; Brown, M.; Jacquemier, J.; Viens, P.; Kleer, C. G.; Liu, S.; Schott, A.; Hayes, D.; Birnbaum, D.; Wicha, M. S.; Dontu, G. ALDH1 Is a Marker of Normal and Malignant Human Mammary Stem Cells and a Predictor of Poor Clinical Outcome. *Cell Stem Cell* **2007**, *1*, 555–567.
- (9) Fang, D.; Nguyen, T. K.; Leishear, K.; Finko, R.; Kulp, A. N.; Hotz, S.; Van Belle, P. A.; Xu, X.; Elder, D. E.; Herlyn, M. A Tumorigenic Subpopulation with Stem Cell Properties in Melanomas. *Cancer Research* **2005**, *65* (20), 9328–9337.
- (10) Collins, A. T.; Berry, P. A.; Hyde, C.; Stower, M. J.; Maitland, N. J. Prospective Identification of Tumorigenic Prostate Cancer Stem Cells. *Cancer Research* **2005**, *65*, 10946–10951.
- (11) Wilson, R. J.; Thomas, C. D.; Fox, R.; Roy, D. B.; Kunin, W. E. Spatial Patterns in Species Distributions Reveal Biodiversity Change. *Nature* **2004**, *432*, 393–396.
- (12) O’Brien, C. A.; Pollett, A.; Gallinger, S.; Dick, J. E. A Human Colon Cancer Cell Capable of Initiating Tumour Growth in Immunodeficient Mice. *Nature* **2006**, *445*, 106–110.
- (13) Li, C.; Heidt, D. G.; Dalerba, P.; Burant, C. F.; Zhang, L.; Adsay, V.; Wicha, M.; Clarke, M. F.; Simeone, D. M. Identification of Pancreatic Cancer Stem Cells. *Cancer Research* **2007**, *67*, 1030–1037.
- (14) Prince, M. E.; Sivanandan, R.; Kaczorowski, A.; Wolf, G. T.; Kaplan, M. J.; Dalerba, P.; Weissman, I. L.; Clarke, M. F.; Ailles, L. E. Identification of a Subpopulation of Cells with Cancer Stem Cell Properties in Head and Neck Squamous Cell Carcinoma. *Proc. Natl. Acad. Sci. U.S.A.* **2007**, *104*, 973–978.

- (15) Skvortsov, S.; Debbage, P.; Lukas, P.; Skvortsova, I. Crosstalk Between DNA Repair and Cancer Stem Cell (CSC) Associated Intracellular Pathways. *Seminars in Cancer Biology* **2015**, *31*, 36–42.
- (16) Maugeri-Sacca, M.; Bartucci, M.; De Maria, R. DNA Damage Repair Pathways in Cancer Stem Cells. *Molecular Cancer Therapeutics* **2012**, *11*, 1627–1636.
- (17) Tothova, Z.; Kollipara, R.; Huntly, B. J.; Lee, B. H.; Castrillon, D. H.; Cullen, D. E.; McDowell, E. P.; Lazo-Kallanian, S.; Williams, I. R.; Sears, C.; Armstrong, S. A.; Passegué, E.; DePinho, R. A.; Gilliland, D. G. FoxOs Are Critical Mediators of Hematopoietic Stem Cell Resistance to Physiologic Oxidative Stress. *Cell* **2007**, *128*, 325–339.
- (18) Ryall, J. G.; Dell’Orso, S.; Derfoul, A.; Juan, A.; Zare, H.; Feng, X.; Clermont, D.; Koulis, M.; Gutierrez-Cruz, G.; Fulco, M.; Sartorelli, V. The NAD⁺-Dependent SIRT1 Deacetylase Translates a Metabolic Switch into Regulatory Epigenetics in Skeletal Muscle Stem Cells. *Stem Cell* **2015**, *16*, 171–183.
- (19) Simsek, T.; Kocabas, F.; Zheng, J.; DeBerardinis, R. J.; Mahmoud, A. I.; Olson, E. N.; Schneider, J. W.; Zhang, C. C.; Sadek, H. A. The Distinct Metabolic Profile of Hematopoietic Stem Cells Reflects Their Location in a Hypoxic Niche. *Stem Cell* **2010**, *7*, 380–390.
- (20) Rodríguez-Colman, M. J.; Schewe, M.; Meerlo, M.; Stigter, E.; Gerrits, J.; Pras-Raves, M.; Sacchetti, A.; Hornsveld, M.; Oost, K. C.; Snippert, H. J.; Verhoeven-Duif, N.; Fodde, R.; Burgering, B. M. T. Interplay Between Metabolic Identities in the Intestinal Crypt Supports Stem Cell Function. *Nature* **2017**, *543*, 424–427.

- (21) Beerling, E.; Seinstra, D.; de Wit, E.; Kester, L.; van der Velden, D.; Maynard, C.; Schäfer, R.; van Diest, P.; Voest, E.; van Oudenaarden, A.; Vrisekoop, N.; van Rheenen, J. Plasticity Between Epithelial and Mesenchymal States Unlinks EMT From Metastasis-Enhancing Stem Cell Capacity. *Cell Reports* **2016**, *14*, 2281–2288.
- (22) Spranger, S.; Bao, R.; Gajewski, T. F. Melanoma-Intrinsic B-Catenin Signalling Prevents Anti-Tumour Immunity. *Nature* **2015**, *523*, 231–235.
- (23) Tan, I.; Storelvmo, T.; Zelinka, M. D. Observational Constraints on Mixed-Phase Clouds Imply Higher Climate Sensitivity. *Science* **2016**, *352*, 224–227.
- (24) Driessens, G.; Beck, B.; Caauwe, A.; Simons, B. D.; Blanpain, C. Defining the Mode of Tumour Growth by Clonal Analysis. *Nature* **2012**, *488*, 527–530.
- (25) Boiko, A. D.; Razorenova, O. V.; van de Rijn, M.; Swetter, S. M.; Johnson, D. L.; Ly, D. P.; Butler, P. D.; Yang, G. P.; Joshua, B.; Kaplan, M. J.; Longaker, M. T.; Weissman, I. L. Human Melanoma-Initiating Cells Express Neural Crest Nerve Growth Factor Receptor CD271. *Nature* **2010**, *466*, 133–137.
- (26) Pascual, G.; Avgustinova, A.; Mejetta, S.; Martín, M.; Castellanos, A.; Attolini, C. S.-O.; Berenguer, A.; Prats, N.; Toll, A.; Hueto, J. A.; Bescós, C.; Di Croce, L.; Benitah, S. A. Targeting Metastasis-Initiating Cells Through the Fatty Acid Receptor CD36. *Nature* **2017**, *541*, 41–45.
- (27) de Goeij, B. E.; Lambert, J. M. ScienceDirect New Developments for Antibody-Drug Conjugate-Based Therapeutic Approaches. *Curr. Opin. Immunol.* **2016**, *40*, 14–23.
- (28) Mullard, A. Maturing Antibody–Drug Conjugate Pipeline Hits 30. *Nat. Rev. Drug Discov.* **2013**, *12*, 329–332.

- (29) Junttila, M. R.; Mao, W.; Wang, X.; Wang, B.-E.; Pham, T.; Flygare, J.; Yu, S.-F.; Yee, S.; Goldenberg, D.; Fields, C.; Eastham-Anderson, J.; Singh, M.; Vij, R.; Hongo, J.-A.; Firestein, R.; Schutten, M.; Flagella, K.; Polakis, P.; Polson, A. G. Targeting LGR5+ Cells with an Antibody-Drug Conjugate for the Treatment of Colon Cancer. *Sci. Transl. Med.* **2015**, *7*, 314ra186.
- (30) Roesch, A.; Vultur, A.; Bogeski, I.; Wang, H.; Zimmermann, K. M.; Speicher, D.; Körbel, C.; Laschke, M. W.; Gimotty, P. A.; Philipp, S. E.; Krause, E.; Pätzold, S.; Villanueva, J.; Krepler, C.; Fukunaga-Kalabis, M.; Hoth, M.; Bastian, B. C.; Vogt, T.; Herlyn, M. Overcoming Intrinsic Multidrug Resistance in Melanoma by Blocking the Mitochondrial Respiratory Chain of Slow-Cycling JARID1B^{high} Cells. *Cancer Cell* **2013**, *23*, 811–825.
- (31) Viale, A.; Pettazzoni, P.; Lyssiotis, C. A.; Ying, H.; Sánchez, N.; Marchesini, M.; Carugo, A.; Green, T.; Seth, S.; Giuliani, V.; Kost-Alimova, M.; Muller, F.; Colla, S.; Nezi, L.; Genovese, G.; Deem, A. K.; Kapoor, A.; Yao, W.; Brunetto, E.; Kang, Y.; Yuan, M.; Asara, J. M.; Wang, Y. A.; Heffernan, T. P.; Kimmelman, A. C.; Wang, H.; Fleming, J. B.; Cantley, L. C.; DePinho, R. A.; Draetta, G. F. Oncogene Ablation-Resistant Pancreatic Cancer Cells Depend on Mitochondrial Function. *Nature* **2014**, *514*, 628–632.
- (32) Takebe, N.; Miele, L.; Harris, P. J.; Jeong, W.; Bando, H.; Kahn, M.; Yang, S. X.; Ivy, S. P. Targeting Notch, Hedgehog, and Wnt Pathways in Cancer Stem Cells: Clinical Update. *Nat. Rev. Clin. Oncol.* **2015**, *12*, 1–20.

- (33) Saunders, L. R.; Bankovich, A. J.; Anderson, W. C.; Aujay, M. A.; Bheddah, S.; Black, K.; Desai, R.; Escarpe, P. A.; Hampl, J.; Laysang, A.; Liu, D.; Lopez-Molina, J.; Milton, M.; Park, A.; Pysz, M. A.; Shao, H.; Slingerland, B.; Torgov, M.; Williams, S. A.; Foord, O.; Howard, P.; Jassem, J.; Badzio, A.; Czapiewski, P.; Harpole, D. H.; Dowlati, A.; Massion, P. P.; Travis, W. D.; Pietanza, M. C.; Poirier, J. T.; Rudin, C. M.; Stull, R. A.; Dylla, S. J. A DLL3-Targeted Antibody-Drug Conjugate Eradicates High-Grade Pulmonary Neuroendocrine Tumor-Initiating Cells in Vivo. *Sci. Transl. Med.* **2015**, *7*, 302ra136–302ra136.
- (34) Hoff, Von, D. D.; LoRusso, P. M.; Rudin, C. M.; Reddy, J. C.; Yauch, R. L.; Tibes, R.; Weiss, G. J.; Borad, M. J.; Hann, C. L.; Brahmer, J. R.; Mackey, H. M.; Lum, B. L.; Darbonne, W. C.; Marsters, J. C., Jr.; de Sauvage, F. J.; Low, J. A. Inhibition of the Hedgehog Pathway in Advanced Basal-Cell Carcinoma. *N. Engl. J. Med.* **2009**, *361*, 1164–1172.
- (35) Frank, N. Y.; Schatton, T.; Frank, M. H. The Therapeutic Promise of the Cancer Stem Cell Concept. *J. Clin. Invest.* **2010**, *120*, 41–50.
- (36) Ramos, E. K.; Hoffmann, A. D.; Gerson, S. L.; Liu, H. New Opportunities and Challenges to Defeat Cancer Stem Cells. *Trends Cancer* **2017**, *3*, 1–17.
- (37) Qin, Z.; Bischof, J. C. Thermophysical and Biological Responses of Gold Nanoparticle Laser Heating. *Chem. Soc. Rev.* **2012**, *41*, 1191–1217.

- (38) Rasulov, A. O.; Gordeyev, S. S.; Barsukov, Y. A.; Tkachev, S. I.; Malikhov, A. G.; Balyasnikova, S. S.; Fedyanin, M. Y. Short-Course Preoperative Radiotherapy Combined with Chemotherapy, Delayed Surgery and Local Hyperthermia for Rectal Cancer: a Phase II Study. *Int. J. Hyperthermia* **2016**, *33*, 465–470.
- (39) Dewhirst, M. W.; Vujaskovic, Z.; Jones, E.; Thrall, D. Re-Setting the Biologic Rationale for Thermal Therapy. *Int. J. Hyperthermia* **2011**, *21*, 779–790.
- (40) Pantano, P.; Harrison, C. D.; Poulouse, J.; Urrabazo Jr, D.; Norman, T. Q.; Braun, E. I.; Draper, R. K.; Overzet, L. J. Factors Affecting the 13.56-MHz Radio-Frequency-Mediated Heating of Gold Nanoparticles. *Appl. Spectrosc. Rev.* **2017**, *0*, 1–16.
- (41) van Valenberg, H.; Colombo, R.; Witjes, F. Intravesical Radiofrequency-Induced Hyperthermia Combined with Chemotherapy for Non-Muscle-Invasive Bladder Cancer. *Int. J. Hyperthermia* **2016**, *32*, 351–362.
- (42) Hurwitz, M. D.; Kaplan, I. D.; Hansen, J. L.; Prokopios-Davos, S.; Topulos, G. P.; Wishnow, K.; Manola, J.; Bornstein, B. A.; Hynynen, K. Hyperthermia Combined with Radiation in Treatment of Locally Advanced Prostate Cancer Is Associated with a Favourable Toxicity Profile. *Int. J. Hyperthermia* **2009**, *21*, 649–656.
- (43) MD, M.-S. C.; MD, K.-L. Y.; PhD, Y.-C. C.; MD, H.-L. K.; MD, Y.-H. L.; Huang, S.-C.; Huang, Y.-Y.; PhD, K.-W. L.; PhD, M. K. M.; MD, K.-H. C. Comparing the Effectiveness of Combined External Beam Radiation and Hyperthermia Versus External Beam Radiation Alone in Treating Patients with Painful Bony Metastases: a Phase 3 Prospective, Randomized, Controlled Trial. *Int. J. Radiat. Oncol. Biol. Phys.* **2018**, *100*, 78–87.

- (44) Overgaard, J.; Gonzalez Gonzalez, D.; Hulshof, M. C. C. H.; Arcangeli, G.; Dahl, O.; Mella, O.; Bentzen, S. M. Hyperthermia as an Adjuvant to Radiation Therapy of Recurrent or Metastatic Malignant Melanoma. a Multicentre Randomized Trial by the European Society for Hyperthermic Oncology. *Int. J. Hyperthermia* **2009**, *25*, 323–334.
- (45) Hurwitz, M. D.; Hansen, J. L.; Prokopios-Davos, S.; Manola, J.; Wang, Q.; Bornstein, B. A.; Hynynen, K.; Kaplan, I. D. Hyperthermia Combined with Radiation for the Treatment of Locally Advanced Prostate Cancer. *Cancer* **2010**, *117*, 510–516.
- (46) Datta, N. R.; Rogers, S.; Klingbiel, D.; Gómez, S.; Puric, E.; Bodis, S. Hyperthermia and Radiotherapy with or Without Chemotherapy in Locally Advanced Cervical Cancer: a Systematic Review with Conventional and Network Meta-Analyses. *Int. J. Hyperthermia* **2016**, *32*, 809–821.
- (47) K, Z.; P, B.; U, L.; D, Z.; C, G. External Validation of a Rectal Cancer Outcome Prediction Model with a Cohort of Patients Treated with Preoperative Radiochemotherapy and Deep Regional Hyperthermia. *Int. J. Hyperthermia* **2019**, *34*, 455–460.
- (48) Harima, Y.; Ohguri, T.; Imada, H.; Sakurai, H.; Ohno, T.; Hiraki, Y.; Tuji, K.; Tanaka, M.; Terashima, H. A Multicentre Randomised Clinical Trial of Chemoradiotherapy Plus Hyperthermia Versus Chemoradiotherapy Alone in Patients with Locally Advanced Cervical Cancer. *Int. J. Hyperthermia* **2016**, *32*, 801–808.
- (49) Refaat, T.; Sachdev, S.; Sathiaseelan, V.; Helenowski, I.; Abdelmoneim, S.; Pierce, M. C.; Woloschak, G.; Small, W., Jr; Mittal, B.; Kiel, K. D. Hyperthermia and Radiation Therapy for Locally Advanced or Recurrent Breast Cancer. *The Breast* **2015**, *24*, 418–425.

- (50) Mantso, T.; Vasileiadis, S.; Anestopoulos, I.; Voulgaridou, G. P.; Lampri, E.; Botaitis, S.; Kontomanolis, E. N.; Simopoulos, C.; Goussetis, G.; FRANCO, R.; *et al.* Hyperthermia Induces Therapeutic Effectiveness and Potentiates Adjuvant Therapy with Non-Targeted and Targeted Drugs in an in Vitro Model of Human Malignant Melanoma. *Sci Rep* **2018**, *8*, 1–16.
- (51) Hoopes, P. J.; Wagner, R. J.; Duval, K.; Kang, K.; Gladstone, D. J.; Moodie, K. L.; Crary-Burney, M.; Ariaspulido, H.; Veliz, F. A.; Steinmetz, N. F.; Fiering, S. N. Treatment of Canine Oral Melanoma with Nanotechnology-Based Immunotherapy and Radiation. *Mol. Pharmaceutics* **2018**, *15*, 3717–3722.
- (52) M, V. G.; de Wee E M; Z, R.; P, T.; U, H. J. A.; Hove I, ten; M, F.; van Rhoon G C; M, P. M. Deep Hyperthermia with the HYPERcollar System Combined with Irradiation for Advanced Head and Neck Carcinoma – a Feasibility Study. *Int. J. Hyperthermia* **2019**, *34*, 994–1001.
- (53) Mu, C.; Wu, X.; Zhou, X.; Wolfram, J.; Shen, J.; Zhang, D.; Mai, J.; Xia, X.; Holder, A. M.; Ferrari, M.; Liu, X.; Shen, H. Chemotherapy Sensitizes Therapy-Resistant Cells to Mild Hyperthermia by Suppressing Heat Shock Protein 27 Expression in Triple-Negative Breast Cancer. *Clin. Cancer Res.* **2018**, *24*, 4900–4912.
- (54) Ozhinsky, E.; Salgaonkar, V. A.; Diederich, C. J.; Rieke, V. MR Thermometry-Guided Ultrasound Hyperthermia of User-Defined Regions Using the ExAblate Prostate Ablation Array. *J. Ther. Ultrasound* **2018**, *6*, 1–10.

- (55) Dubois, M. F.; Hovanessian, A. G.; Bensaude, O. Heat-Shock-Induced Denaturation of Proteins. Characterization of the Insolubilization of the Interferon-Induced P68 Kinase. *J. Biol. Chem.* **1991**, *266*, 9707–9711.
- (56) Stein, U.; Jürchott, K.; Walther, W.; Bergmann, S.; Schlag, P. M.; Royer, H. D. Hyperthermia-Induced Nuclear Translocation of Transcription Factor YB-1 Leads to Enhanced Expression of Multidrug Resistance-Related ABC Transporters. *J. Biol. Chem.* **2001**, *276*, 28562–28569.
- (57) Oei, A. L.; Vriend, L. E. M.; Crezee, J.; Franken, N. A. P.; Krawczyk, P. M. Effects of Hyperthermia on DNA Repair Pathways: One Treatment to Inhibit Them All. *Radiat. Oncol.* **2015**, *10*, 1–13.
- (58) Pelicci, P. G.; Dalton, P.; Orecchia, R. Heating Cancer Stem Cells to Reduce Tumor Relapse. *Breast Cancer Res.* **2011**, *13*, 105–2.
- (59) Carnero, A.; Leonart, M. The Hypoxic Microenvironment: a Determinant of Cancer Stem Cell Evolution. *Inside the Cell* **2015**, *1*, 96–105.
- (60) Zhang, Z.; Wang, J.; Chen, C. Near-Infrared Light-Mediated Nanoplatfoms for Cancer Thermo-Chemotherapy and Optical Imaging. *Adv. Mater.* **2013**, *25*, 3869–3880.
- (61) Li, J.-L.; Bao, H.-C.; Hou, X.-L.; Sun, L.; Wang, X.-G.; Gu, M. Graphene Oxide Nanoparticles as a Nonbleaching Optical Probe for Two-Photon Luminescence Imaging and Cell Therapy. *Angew. Chem. Int. Ed.* **2012**, *51*, 1830–1834.
- (62) Jin, G.; He, R.; Liu, Q.; Dong, Y.; Lin, M.; Li, W.; Xu, F. Theranostics of Triple-Negative Breast Cancer Based on Conjugated Polymer Nanoparticles. *ACS Appl. Mater. Interfaces* **2018**, *10*, 10634–10646.

- (63) Yao, H.-J.; Zhang, Y.-G.; Sun, L. The Effect of Hyaluronic Acid Functionalized Carbon Nanotubes Loaded with Salinomycin on Gastric Cancer Stem Cells. *Biomaterials* **2014**, *35*, 9208–9223.
- (64) Zhang, L.; Su, H.; Cai, J.; Cheng, D.; Ma, Y.; Zhang, J.; Zhou, C.; Liu, S.; Shi, H.; Zhang, Y.; Zhang, C. A Multifunctional Platform for Tumor Angiogenesis-Targeted Chemothermal Therapy Using Polydopamine-Coated Gold Nanorods. *ACS Nano* **2016**, *10*, 10404–10417.
- (65) Xu, Y.; Wang, J.; Li, X.; Liu, Y.; Dai, L.; Wu, X.; Chen, C. Selective Inhibition of Breast Cancer Stem Cells by Gold Nanorods Mediated Plasmonic Hyperthermia. *Biomaterials* **2014**, *35*, 4667–4677.
- (66) Pérez-Hernández, M.; del Pino, P.; Mitchell, S. G.; Moros, M.; Stepien, G.; Pelaz, B.; Parak, W. J.; Gálvez, E. M.; Pardo, J.; la Fuente, de, J. M. Dissecting the Molecular Mechanism of Apoptosis During Photothermal Therapy Using Gold Nanoprisms. *ACS Nano* **2015**, *9*, 52–61.
- (67) Sun, T.; Wang, Y.; Wang, Y.; Xu, J.; Zhao, X.; Vangveravong, S.; Mach, R. H.; Xia, Y. Using SV119-Gold Nanocage Conjugates to Eradicate Cancer Stem Cells Through a Combination of Photothermal and Chemo Therapies. *Adv. Healthcare Mater.* **2014**, *3*, 1283–1291.
- (68) Sun, T.-M.; Wang, Y.-C.; Wang, F.; Du, J.-Z.; Mao, C.-Q.; Sun, C.-Y.; Tang, R.-Z.; Liu, Y.; Zhu, J.; Zhu, Y.-H.; Yang, X.-Z.; Wang, J. Cancer Stem Cell Therapy Using Doxorubicin Conjugated to Gold Nanoparticles via Hydrazone Bonds. *Biomaterials* **2014**, *35*, 836–845.

- (69) Atkinson, R. L.; Zhang, M.; Diagaradjane, P.; Peddibhotla, S.; Contreras, A.; Hilsenbeck, S. G.; Woodward, W. A.; Krishnan, S.; Chang, J. C.; Rosen, J. M. Thermal Enhancement with Optically Activated Gold Nanoshells Sensitizes Breast Cancer Stem Cells to Radiation Therapy. *Sci. Transl. Med.* **2010**, *2*, 55ra79–55ra79.
- (70) Chen, L.; Long, C.; Tran, K. A. M.; Lee, J. A Synthetic Binder of Breast Cancer Stem Cells. *Chem. Eur. J.* **2018**, *24*, 3694–3698.
- (71) Alkilany, A. M.; Nagaria, P. K.; Hexel, C. R.; Shaw, T. J.; Murphy, C. J.; Wyatt, M. D. Cellular Uptake and Cytotoxicity of Gold Nanorods: Molecular Origin of Cytotoxicity and Surface Effects. *Small* **2009**, *5*, 701–708.
- (72) Conde, J.; Oliva, N.; Artzi, N. Implantable Hydrogel Embedded Dark-Gold Nanoswitch as a Theranostic Probe to Sense and Overcome Cancer Multidrug Resistance. *Proc. Natl. Acad. Sci. U.S.A.* **2015**, *112*, E1278–E1287.
- (73) Ali, M. R. K.; Wu, Y.; Tang, Y.; Xiao, H.; Chen, K.; Han, T.; Fang, N.; Wu, R.; El-Sayed, M. A. Targeting Cancer Cell Integrins Using Gold Nanorods in Photothermal Therapy Inhibits Migration Through Affecting Cytoskeletal Proteins. *Proc. Natl. Acad. Sci. U.S.A.* **2017**, *114*, E5655–E5663.
- (74) Ungureanu, C.; Kroes, R.; Petersen, W.; Groothuis, T. A. M.; Ungureanu, F.; Janssen, H.; van Leeuwen, F. W. B.; Kooyman, R. P. H.; Manohar, S.; van Leeuwen, T. G. Light Interactions with Gold Nanorods and Cells: Implications for Photothermal Nanotherapeutics. *Nano Lett.* **2011**, *11*, 1887–1894.

- (75) Yu, F.; Li, J.; Chen, H.; Fu, J.; Ray, S.; Huang, S.; Zheng, H.; Ai, W. Kruppel-Like Factor 4 (KLF4) Is Required for Maintenance of Breast Cancer Stem Cells and for Cell Migration and Invasion. *Oncogene* **2011**, *30*, 2161–2172.

\

CHAPTER 3

TYROSINE-ASSISTED GOLD NANOCUSTER FOR SENSING FERRIC AND COPPER IONS

3.1 Introduction

Ultrasmall gold nanoclusters (AuNCs) comprising of several gold atoms have been gained wide popularity in the field of catalysis, bioimaging, optical sensing, and biomedicine due to their unique physical and optoelectronic properties, such as ultrasmall sizes, large Stokes shift, longer fluorescence lifetimes, photostability, biocompatibility, and feasibility of surface functionalization.¹⁻⁷ When the size of AuNC approaches the Fermi wavelength (~ 1 nm) of the electrons, the continuous band of energy breaks into discrete electron transition energy levels, exhibiting the single molecule-like fluorescence.⁸⁻¹¹ The electrons filled in $5d^{10}$ of the valence band are excited to $6sp^1$ of the conduction band, thereby possessing a strong fluorescence emission from the visible to the near-infrared region.¹⁰

There are two common strategies, bottom-up and top-down, for preparation of fluorescent AuNCs. The bottom-up approach is to reduce the Au ions to the Au atom through chemical, biological, optical, and electrochemical reduction of the Au ions. However, due to the aggregation propensity of as-prepared AuNCs, suitable surface ligands acting as stabilizers, such as small thiol molecules, polymers, peptides, and proteins are essential for the preparation of stable AuNCs. In the top-down approach, on the other hand, larger gold nanoparticles (~ 100 nm) are etched by adding excess etching agents, such as polyethylenimine (PEI), dihydrolipoic acid (DHLA), or glutathione (GSH).¹²⁻¹⁴

Several synthetic methods for generating fluorescent AuNCs have been developed through the use of ligands acting as both reducing agents and stabilizers. Such ligands include proteins,

peptides, polymers, and DNA.¹⁵⁻¹⁹ For example, AuNCs accommodating proteins including tyrosine and cysteine residues have been found to form fluorescent AuNCs. The thiol group in cysteine residue binds to Au precursor (Au^{3+}) via strong Au-S bonds. Afterwards, the phenolic group of tyrosine reduces the Au^{3+} into Au^0 under alkaline condition. By electron transfer, the phenolic group of tyrosine is transformed to a quinone.²⁰⁻²³

AuNCs have become known as promising tools for the development of chemical sensors. The straightforward detection, high responsiveness, minimum sample requirement, and real time monitoring with fast response time capabilities enable them to make excellent sensing systems for detecting highly mutagenic metal ions such as Hg^{2+} , Fe^{3+} , Cu^{2+} , Pb^{2+} , and Cr^{3+} .²⁴⁻²⁹ Most of the detections were based on the fluorescence quenching of AuNCs in presence of target metal ions.^{24,30,31} In sensing mechanisms known to date, an electron transfer phenomenon is commonly found in the Hg^{2+} sensing system. Because Hg^{2+} strongly binds to Au^0 , the core of AuNC, energy transfer takes place as the excited electron of Au is transferred to Hg^{2+} .³¹ Besides Hg^{2+} sensing, the fluorescence quenching can occur *via* the aggregation of AuNCs. Under the existence of metal ions such as Fe^{3+} , Cu^{2+} , and Pb^{2+} , metal ions are strongly coordinated with the ligand on the adjacent AuNCs, inducing aggregation, thereby attenuating the fluorescence.^{24-26,28}

In this chapter, we introduce fluorescent AuNCs composing of tyrosine containing two different tripeptides – tyrosine-cysteine-tyrosine (YCY) and serine-cysteine-tyrosine (SCY). A cysteine residue was employed to utilize thiol group for S-Au bonding, and tyrosine residues were located at C-terminal and N-terminal. In addition, tyrosine residue at N-terminal was replaced with serine to examine the reduction capability in terms of the number of tyrosine. Blue- and red-emission AuNC from the YCY peptide and blue-emission SCY-AuNC were obtained.

Subsequently, we investigated the metal ions sensing ability of these AuNCs, and observed that only Blue-YCY-AuNC and Blue-SCY-AuNC sensitively lost their fluorescence signals in the presence of Fe^{3+} and Cu^{2+} . Interestingly, two tyrosine-residues containing Blue-YCY-AuNC exhibited higher sensitive sensing of Fe^{3+} and Cu^{2+} than the Blue-SCY-AuNC. Moreover, we found that fluorescence quenching under the presence of target metal ion occurred due to the aggregation of AuNC, so that we investigated the chelation behavior of surface ligands and their effects on the AuNC aggregation under the presence of their target. Corresponding with the sensitivity of AuNCs, Blue-YCY-AuNC formed larger complexes than complexes of Blue-SCY-AuNC.

3.2 Experimental section

3.2.1 Reagents and materials

N,N-Dimethylformamide (DMF), methanol (MeOH), acetonitrile (ACN), dimethyl sulfoxide (DMSO), ethyl ether and dichloromethane (DCM) were all HPLC grade, and were purchased from Thermo Fisher Scientific. Trifluoroacetic acid (TFA), glutathione (GSH), *N,N*-diisopropylethylamine (DIPEA), and piperidine were obtained from Sigma-Aldrich. Nitrate salts of metal ions (AgNO_3 , $\text{Al}(\text{NO}_3)_3$, $\text{Ba}(\text{NO}_3)_2$, $\text{Ca}(\text{NO}_3)_2$, $\text{Co}(\text{NO}_3)_2$, $\text{Cu}(\text{NO}_3)_2$, $\text{Fe}(\text{NO}_3)_3$, KNO_3 , $\text{Mg}(\text{NO}_3)_2$, NaNO_3 , $\text{Ni}(\text{NO}_3)_2$, $\text{Pb}(\text{NO}_3)_2$, and $\text{Zn}(\text{NO}_3)_2$) were purchased from Sigma-Aldrich. Auric chloride ($\text{HAuCl}_4 \cdot 3\text{H}_2\text{O}$) was obtained from Aldrich. Fmoc-Tyr(*t*Bu)-OH, Fmoc-Cys(*trt*)-OH, Fmoc-Ser(*t*Bu)-OH, Rink Amide MBHA resin (100-200 mesh) and 2-(1*H*-benzotriazol-1-yl)-1,1,3,3-tetramethyluronium hexafluorophosphate (HBTU) were purchased from Novabiochem. 1-hydroxybenzotriazole hydrate (HOBt· H_2O) was obtained from Creosalus. Sephadex™ G-25 was

purchased from GE Healthcare. Dialysis membrane kit (Slide-A-Lyzer[®]Dialysis Cassette G2; 3.5 KDa cutoff) was obtained from Thermo Scientific. Ultrapure water (18.2 MΩcm, Millipore Co.) was used in all experiments.

3.2.2 Synthesis of tripeptides

Tyrosine-cysteine-tyrosine (YCY) and serine-cysteine-tyrosine (SCY) peptides were synthesized using Rink Amide MBHA resin. 600 mg of Rink Amide MBHA was swelled in 3 mL of DMF for 1 h and followed by deprotection with 20% piperidine (20% in DMF v/v). After a full wash with 5 times with DMF, 2 times with MeOH, 2 times with DCM, and 3 times with DMF, pre-mixed 5 equivalents of Fmoc-Try(tBU)-OH, HOBt·H₂O, HBTU, and 10 equivalents of DIPEA in dry DMF were added in the resins and mixed at room temperature for 3h. All the beads were fully washed after each reaction step. The beads were deprotected with 20% piperidine and were mixed with cocktail solution of Fmoc-Cys(Trt)-OH for 3 h. Followed by the addition of 20% piperidine, the beads were divided equally into 2 fritted cartridges. Two individual cartridges were mixed with the cocktail solution of Fmoc-Try(tBu)-OH and Fmoc-Ser(tBu)-OH. After the peptide coupling reaction, the Fmoc protecting group was removed using 20% piperidine. The peptides were cleaved and deprotected in TFA solution (95% TFA, 2.5% TIS, 2.5% H₂O) for 2 h and additional 20 min with the fresh TFA solution. The solution was collected and evaporated using argon gas. When the solution left 10% out of initial volume, chilled ethyl ether was added to remove the protecting groups. The precipitation was centrifuged down at 4,000g and discard the supernatant. This step was repeated two times more. After removing protecting groups, the peptides were dried under vacuum. The resulting powders were dissolved in water with 0.1% TFA

and purified by preparative RP-HPLC. Pure fractions were identified by HPLC-MS/MS (HPLC: Agilent, 1100 Series, MS/MS: Sciex, 4000 Q Trap) and collected in tubes. After purification, pure tripeptides were validated by analytical HPLC-MS/MS. The resulting solutions were lyophilized and kept in -20 °C before using.

3.2.3 Preparation of YCY- and SCY-templated fluorescent AuNCs.

The exact concentration of the YCY and SCY aqueous solutions was determined by Ellman's reagent (DTNB). Glutathione was used as a standard reagent. The glass vial was cleaned using Aqua regia (HCl:HNO₃, 3:1 v/v) and thoroughly rinsed with H₂O prior to use. In the typical method for the synthesis of peptide-templated AuNCs, 0.5 mL of peptide solution (25 mM in H₂O) was slowly added to 0.5 mL of HAuCl₄·3H₂O (25 mM in H₂O) under stirring. After mixing the solution for 15 min at 70 °C, the pH of the solution was adjusted to pH 10 by addition of NaOH (1 M). The mixed solution was then kept stirring at 70 °C for 8 h. The solution was cooled to room temperature, and it was transferred to 1.5 mL individual microtube following by centrifugation at 16,000 g for 10 min to remove the sediment and other impurities. The blue-emitting YCY- and SCY-AuNCs were in the supernatant and the red-emitting YCY-AuNCs were trapped inside of the precipitation after centrifugation. The red-emitting YCY-AuNCs were extracted by 1:1 of DMSO and 10% acetic acid aqueous solution. After 10 min sonication, the solution was centrifuged down at 16,000g for 30 min to remove the precipitation. The yellow clear supernatants were transferred in the new tubes. Afterward, each of AuNC solutions was purified via a SephadexTM G-25 column equilibrated and eluted with H₂O (1 mL/min). 0.5 mL fractions were collected and analyzed by a UV-Vis absorption and fluorescence using a microplate reader.

Fractions containing fluorescent AuNC were collected and dialyzed in H₂O using a 3.5 kDa cutoff membrane kit to separate the AuNCs from any unreacted species and to adjust pH to be a neutral. The AuNC solutions were stored at 4 °C in dark for further the characterization and experiment.

3.2.4 Characterization of AuNCs

UV-Vis spectra of the AuNC solution were measured with a microplate reader (Spark 20M; Tecan). Fluorescence spectra were obtained with Horiba Fluorolog fluorometer (Horiba Scientific). The measurement was conducted with 1 cm quartz cuvette at room temperature. The slit for the excitation and the emission was set to 5 nm. TEM images were taken using the JEM-2100F (JEOL). A drop of the AuNC solution (0.1 mg/mL) was deposited on a carbon-coated Cu grid and analyzed. Dynamic light scattering (DLS) and zeta-potential were measured by Nano-ZS (Malvern Instrument).

3.2.5 The influence of pH and NaCl on fluorescence intensity

The pH and the salt sensitivity of the AuNCs were characterized by mixing 100 µL of each AuNC solutions (Blue-YCY-AuNC and Blue-SCY-AuNC: 0.5 mg/mL, Red-YCY-AuNC: 0.15 mg/mL) with 400 µL of the different buffer solutions and NaCl solutions. The fluorescence spectra were achieved by 325 nm excitation and 400 nm excitation for blue-emitting and red-emitting AuNC, respectively.

3.2.6 Fluorescent detections of metal ions

The following metal salts were used: Ag^+ , Al^{3+} , Ba^{2+} , Ca^{2+} , Co^{2+} , Cu^{2+} , Fe^{3+} , K^+ , Mg^{2+} , Na^+ , Ni^{2+} , Pb^{2+} , and Zn^{2+} . These metal salts were dissolved in H_2O . 300 μL of each AuNC solution (Blue-YCY-AuNC and Blue-SCY-AuNC: 0.2 mg/mL, Red-YCY-AuNC: 0.06 mg/mL) and 300 μL of particular metal ion solutions (100 μM) were mixed and the mixture was left to be equilibrated at room temperature for 2 min. 500 μL of the solution was placed on the cuvette and the fluorescence quenching spectra were measured from appropriate excitation wavelength (Blue-YCY-AuNC and Blue-SCY-AuNC: 325 nm, Red-YCY-AuNC: 400 nm). Serial dilutions of Fe^{3+} and Cu^{2+} solutions were also mixed with each AuNC solution and incubated for 2 min before the measurement.

3.2.7 Quantum yield (QY) measurement of AuNCs

Quantum yields of each AuNC were calculated using the formula,

$$\Phi_X = \Phi_{ST} \left(\frac{\text{Grad}_X}{\text{Grad}_{ST}} \right) \left(\frac{\eta^2_X}{\eta^2_{ST}} \right),$$

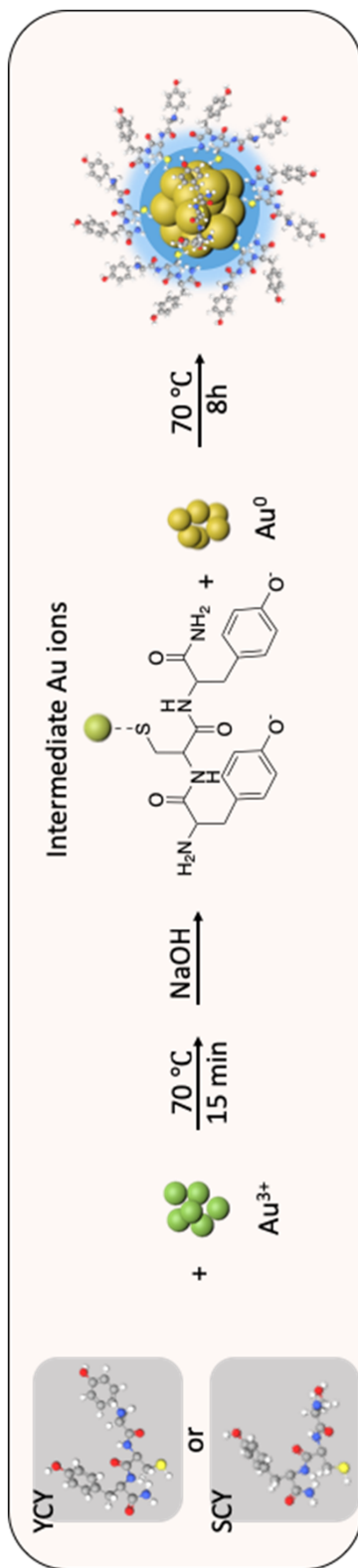
where the subscripts ST and X denote standard and sample respectively, Φ is the fluorescence quantum yield, Grad the gradient from the plot of integrated fluorescence intensity versus absorbance, and η is the refractive index of the solvent. We hired quinine sulfate (QY: 0.54) in 0.1 M H_2SO_4 (η : 1.33) as a fluorescence standard for the calculation of the QY of Blue-YCY- and Blue-SCY-AuNCs. For the measurement of the QY of Red-YCY-AuNC, 9,10-diphenyl anthracene (QY: 0.90) in cyclohexane (η : 1.44) was used as a reference fluorophore. We recorded the UV-vis absorbance spectrum of five serial solutions of each sample including solvent

background for the chosen references. Afterward, the fluorescence spectra of the same solution in the 1 cm fluorescence cuvette were measured. Graphs of integrated fluorescence intensity versus absorbance were plotted.

3.3 Results and discussion

3.3.1 Preparation of AuNCs

In this study, we synthesized fluorescent AuNCs by employing tyrosine-containing tripeptides as both a reducing and capping agent. The phenolic OH group in tyrosine reduced Au³⁺ to Au⁰ through electron oxidation resulting in forming of the *o*-hydroquinone derivative (Scheme 3.1).^{25,32} We increased the temperature to accelerate the reduction of Au³⁺ ions. The key to utilizing the reduction capability of tyrosine for synthesis of AuNC is pH.^{15,33} In order to optimize a pH condition for synthesizing peptide-templated AuNCs, we added different amounts of 1 M NaOH to the mixture of HAuCl₄ and the pure peptide (the purity of as-synthesized peptides was shown in Figures S.3.1 and S.3.2). Glutathione, natural tripeptide, was used as a control peptide, due to the absence of the tyrosine and the feasibility of synthesizing the fluorescent AuNC.^{28,34} After 8 h reaction at 70 °C, the strong emission peak at 415 nm for both of YCY- and SCY-AuNCs appeared with 325 nm excitation when the pH of the mixture was greater than 7 (Figures 3.1 a and c). The strongest emission peak of YCY- and SCY-AuNCs was achieved at pH 10. Interestingly, an additional emission peak of YCY-AuNC was observed at 670 nm from 400 nm excitation (Figure 3.1 d), but not in the SCY-AuNC. Under the acidic and neutral pH conditions, on the other hand, the GSH-AuNC gave fluorescence spectra with two distinct peaks at 390 nm and 800 nm from 325 nm excitation and with one obvious peak at 800 nm from 400 nm excitation (Figures 3.1 e and f).



Scheme 3.1. Schematic illustration of the preparation of fluorescent AuNC via tyrosine-assisted reduction.

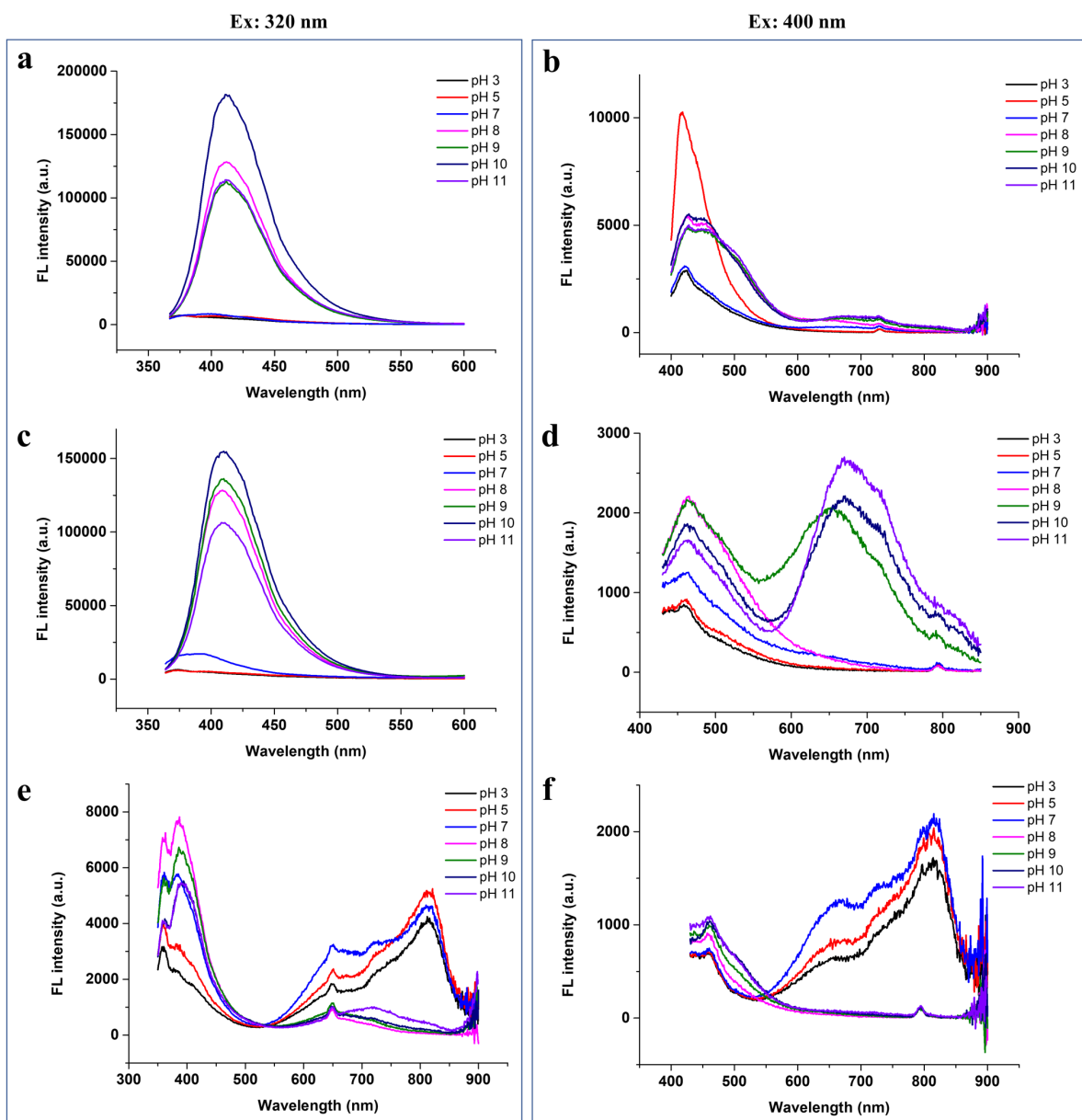


Figure 3.1. Effect of pH on the synthesis of tyrosine-assisted AuNCs. Fluorescence emission spectra of the crude AuNC solutions prepared by mixing with different peptides at the different pH condition with 325 nm and 400 nm excitations. (a) and (b) SCY peptide. (c) and (d) YCY peptide. (e) and (f) glutathione.

From this result, we found that the optimal pH condition for the synthesis of fluorescent AuNCs was pH 10, in which the tyrosine further facilitated the formation of AuNCs.

Under optimal condition, the color of YCY solution changed from clear to red, and the color of SCY solution changed from clear to brown during the reaction. Solutions of YCY- and SCY-AuNC were centrifuged down to remove the sediment and agglomerated particles. The strong blue emitting light was observed under the 365 nm UV lamp in supernatants of YCY- and SCY-AuNC solutions. Interestingly, the precipitate of the centrifuged YCY-AuNC solution emitted deep-red fluorescence under the 365 nm UV lamp. We obtained red-emitting YCY-AuNCs from the precipitate using 10% acetic acid and DMSO (1:1 v/v). Afterward, we purified AuNCs using a size exclusion column to remove unreacted peptides, gold ions, and non-fluorescent gold nanoparticles, which are not removed by the centrifugation (Figure S.3.2 c). After the dialysis, the AuNC solutions exhibited neutral pH (~ pH 7).

3.3.2 The optical and physical characteristics of AuNCs.

Photo images in Figure 3.2 are Blue-YCY-AuNC, Blue-SCY-AuNC, and Red-YCY-AuNC under 365nm UV lamp showing uniform dispersity of the AuNCs in aqueous solution with slight yellow under visible light. In UV-vis spectra (Figure 3.2 blue curve), the absence of surface plasmon resonance peak (520-530 nm) indicated that the as-synthesized AuNCs had a smaller diameter than 2.5 nm.³⁵ A distinct peak at 325 nm appeared in the UV-Vis absorption spectra of Blue-YCY-AuNC and Blue-SCY-AuNC. However, the absorption spectra of YCY and SCY peptides appeared at 278 nm (data not shown). Maxima excitation peaks of Blue-YCY-AuNC and Blue-SCY-AuNC were exhibited the same wavelength, 325 nm, with no overlap with the absorption of *o*-quinone (285 nm).³² Minor peaks of Blue-YCY-AuNC and Blue-SCY-AuNC were observed at 350 nm and 380 nm, respectively. The strongest blue emission wavelength (415 nm)

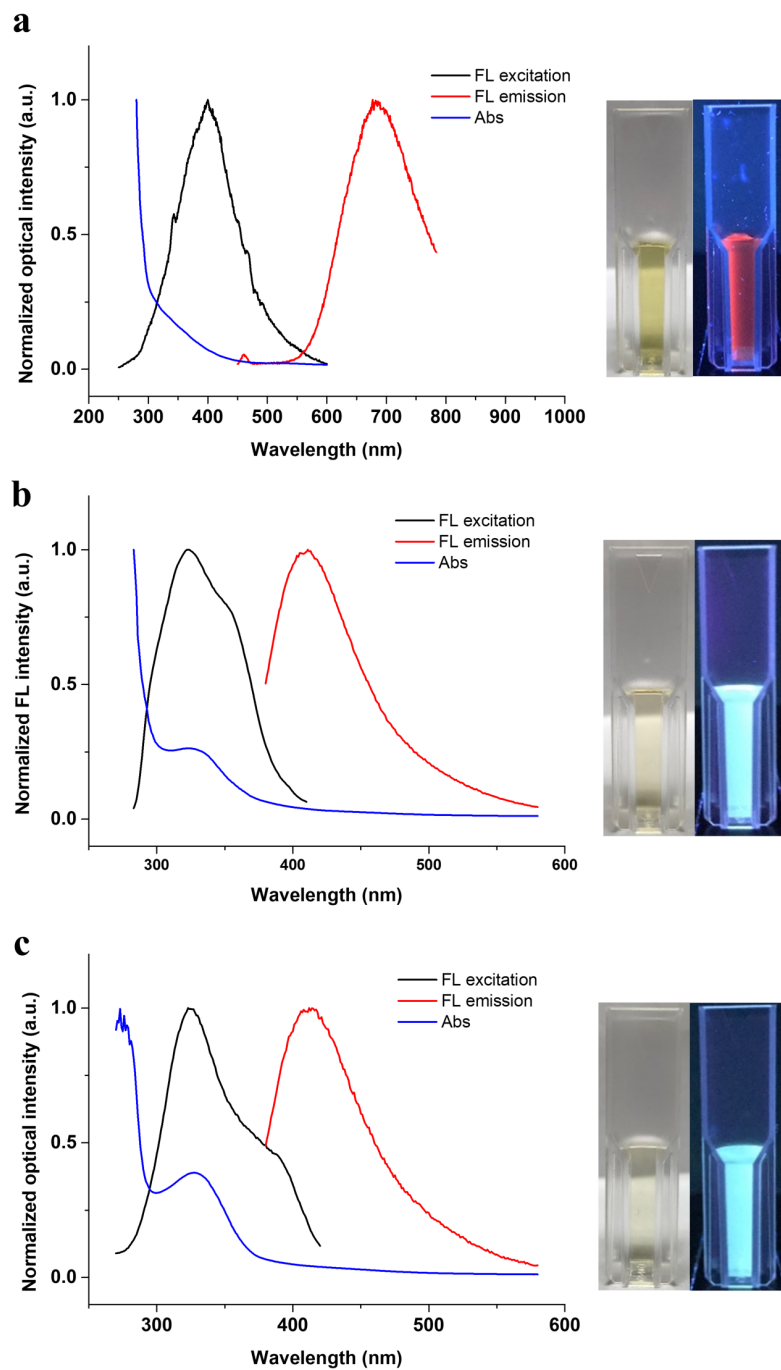


Figure 3.2. UV-Vis and fluorescence spectra of AuNCs. The UV-Vis, fluorescence emission and excitation spectra of (a) Red-YCY-AuNC, (b) Blue-YCY-AuNC, and (c) Blue-SCY-AuNC [Photographs: AuNC solutions under visible light (left) 365 nm UV lamp (right)]

of Blue-YCY-AuNC and Blue-SCY-AuNC was achieved when excited by 325 nm (Figure 3.2 b and c). The Red-YCY-AuNC showed broad absorption peak, suspecting that this broad absorption is resulted from the multiple absorption of the AuNCs. However, a single strong excitation peak was detected at 400 nm. The emission peak of Red-YCY-AuNC appeared at 670 nm (Figure 3.2

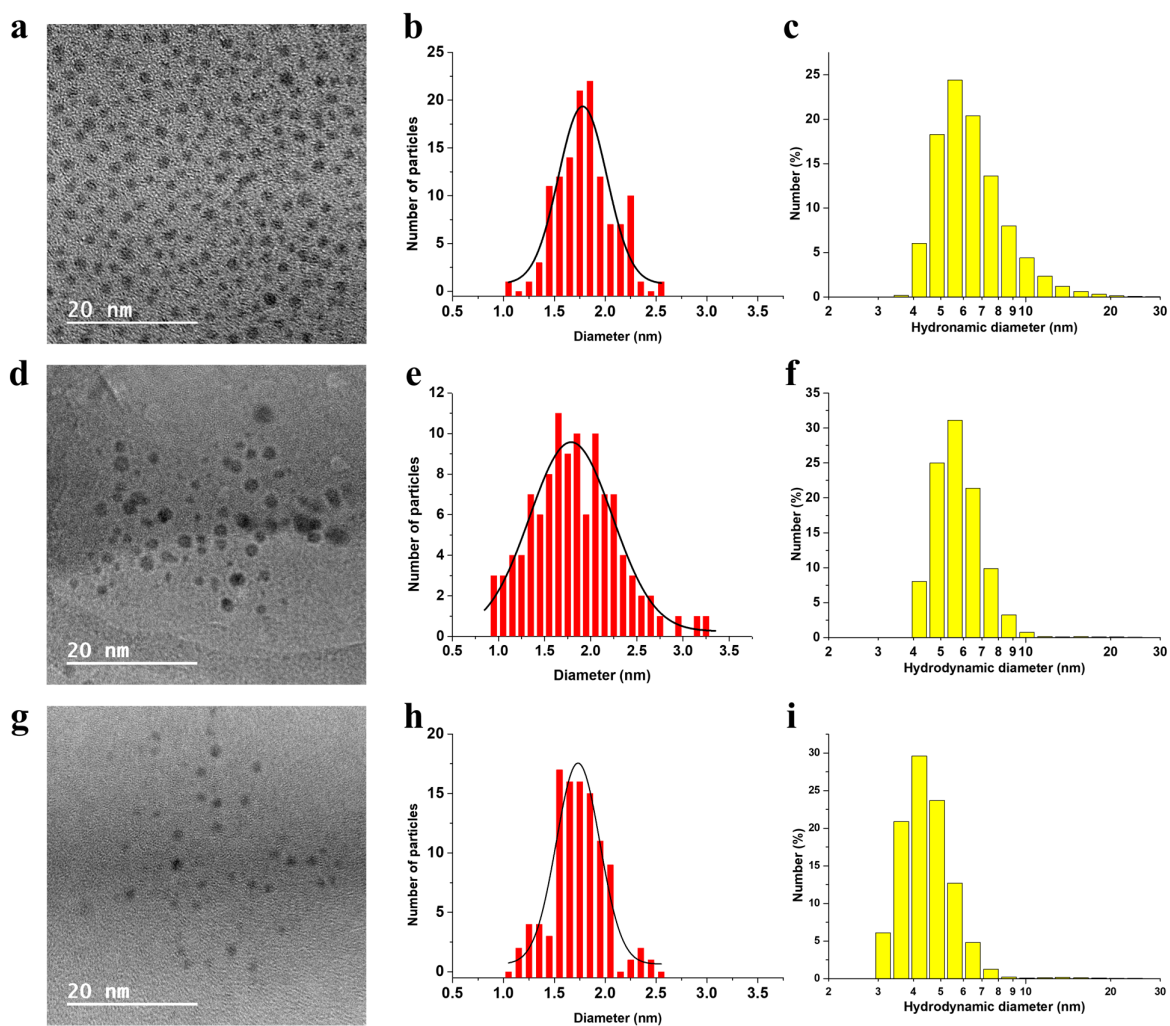


Figure 3.3. Size analysis of AuNCs using TEM and DLS. Red-YCY-AuNC: (a) TEM image, (b) size distribution histogram and (c) DLS histogram. Blue-YCY-AuNC: (d) TEM image, (e) size distribution histogram and (f) DLS histogram. Blue-SCY-AuNC: (g) TEM image, (h) size distribution histogram and (i) DLS histogram.

a). Fluorescence quantum yields of Red-YCY-AuNC, Blue-YCY-AuNC, and Blue-SCY-AuNC are 0.8%, 1.2%, and 1.5%, respectively.

As shown in Figure 3.3, high resolution TEM images indicated that all peptide-templated AuNCs were monodispersed with uniformity in size and spherical shape. Size distribution histograms of each peptide-templated AuNCs were constructed by measuring diameters of 100 individual AuNCs. The average size of the Blue-SCY-AuNC was found to be 1.72 ± 0.25 nm. Interestingly, Blue- and Red-YCY-AuNCs exhibited almost identical size, 1.82 ± 0.47 nm and 1.81 ± 0.26 nm, respectively. According to DLS results, hydrodynamic diameters of all peptide-templated AuNCs were larger than those obtained from TEM analysis (Figure 3.3 c, f and i). This discrepancy can be explained by the external immobilization and the hydration of peptides on nanoclusters. Taken together, these experimental results demonstrate that we successfully prepared fluorescent peptide-templated AuNCs without requiring any chemical reducing agent.

As shown in Figure 3.4 a, all AuNCs were stable under high ionic strength conditions. To investigate the fluorescent response of the AuNCs to pH value, we measured fluorescence intensities of the AuNCs after mixing with different pH buffer solution. As shown in Figure 3.4 b red circle and blue triangle, fluorescence intensities of blue-YCY- and SCY-AuNCs decreased from pH 7 to pH 3. On the contrary, in the alkaline condition the fluorescence of the AuNCs showed the enhanced signals. Interestingly, Red-YCY-AuNCs exhibited the complete opposite trend of blue-emitting AuNCs (Figure 3.4 b black square). These results speculate that the YCY and SCY peptides on the surface of Blue-YCY-AuNC and Blue-YCY-AuNC may have the same surface configurations to Au atoms while the configuration of Red-YCY-AuNC is different. This notion can be supported by the results of zeta potential of each AuNC. Blue-YCY- and SCY-

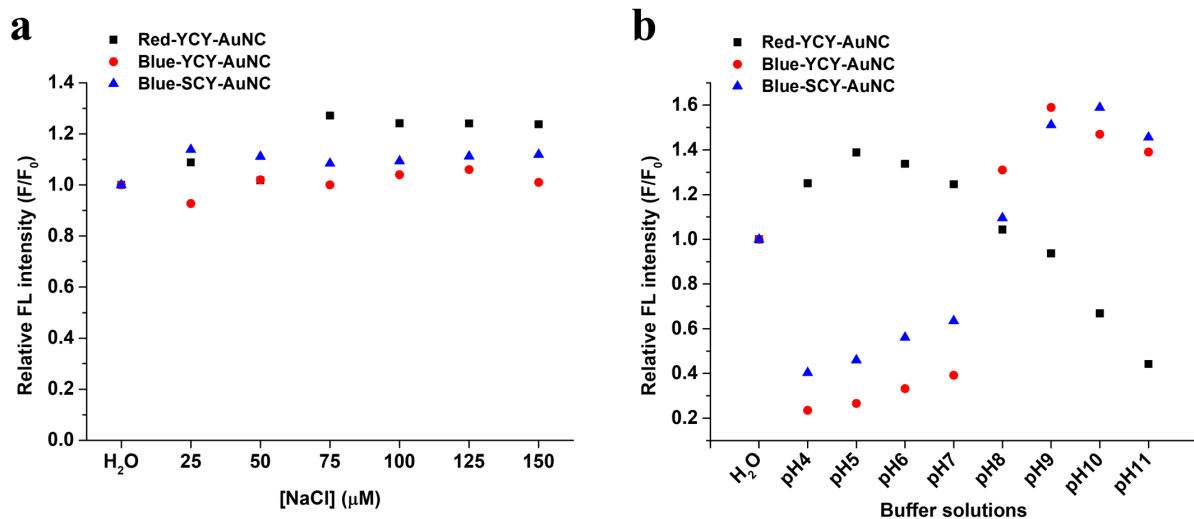


Figure 3.4. Stability of AuNCs in high salt solution and different pH buffer. (a) Fluorescence intensity of Blue-YCY-AuNC, Blue-SCY-AuNC (λ_{ex} : 325 nm, λ_{em} : 415 nm) and Red-YCY-AuNC (λ_{ex} : 400 nm, λ_{em} : 675 nm) after mixing with increasing concentration of NaCl. (b) Fluorescence intensity of Blue-YCY-AuNC, Blue-SCY-AuNC (λ_{ex} : 325 nm, λ_{em} : 415 nm) and Red-YCY-AuNC (λ_{ex} : 400 nm, λ_{em} : 675 nm) at different pH values.

AuNCs exhibited -13.0 mV and -11.8 mV in H₂O at room temperature, while Red-YCY-AuNC exhibited +45.6 mV. The possible explanation is that the Red-YCY-AuNC can have the different coordination bonding with Blue-emitting AuNC between the O⁻ group of the unoxidized tyrosine and Au atoms.³⁶ Conversely, in the case of blue-emitting AuNCs, the coordination bonding is between -SH at cysteine and Au atoms. With these observations, it is assumed that Blue-emitting AuNCs shows weak negative charge, while Red-YCY-AuNC shows strong positive charge in zeta potential measurement. Overall, the AuNCs in H₂O (labeled as blank) were relatively stable when compared to the fluorescence intensity in different pH conditions. Furthermore, to scrutinize the change of the fluorescence of the AuNCs without interference, such as ions and chemicals, we chose H₂O to conduct further experiment.

3.3.3 Metal ion selectivity and sensitivity of AuNCs

Tyrosine residue in the peptide side chain has shown strong interaction with the transition metal ion by forming a square planar complex in which the C-terminal carboxylate, amide nitrogens, and N-terminal amine bound to metal ions.^{36,37} In addition, studies have shown that *o*-quinone, the oxidized form of tyrosine resulting from the reduction of Au³⁺ to Au⁰, can form complexes with Fe³⁺ and Cu²⁺.^{38,39} Therefore, we explored the sensing capability of as-synthesized

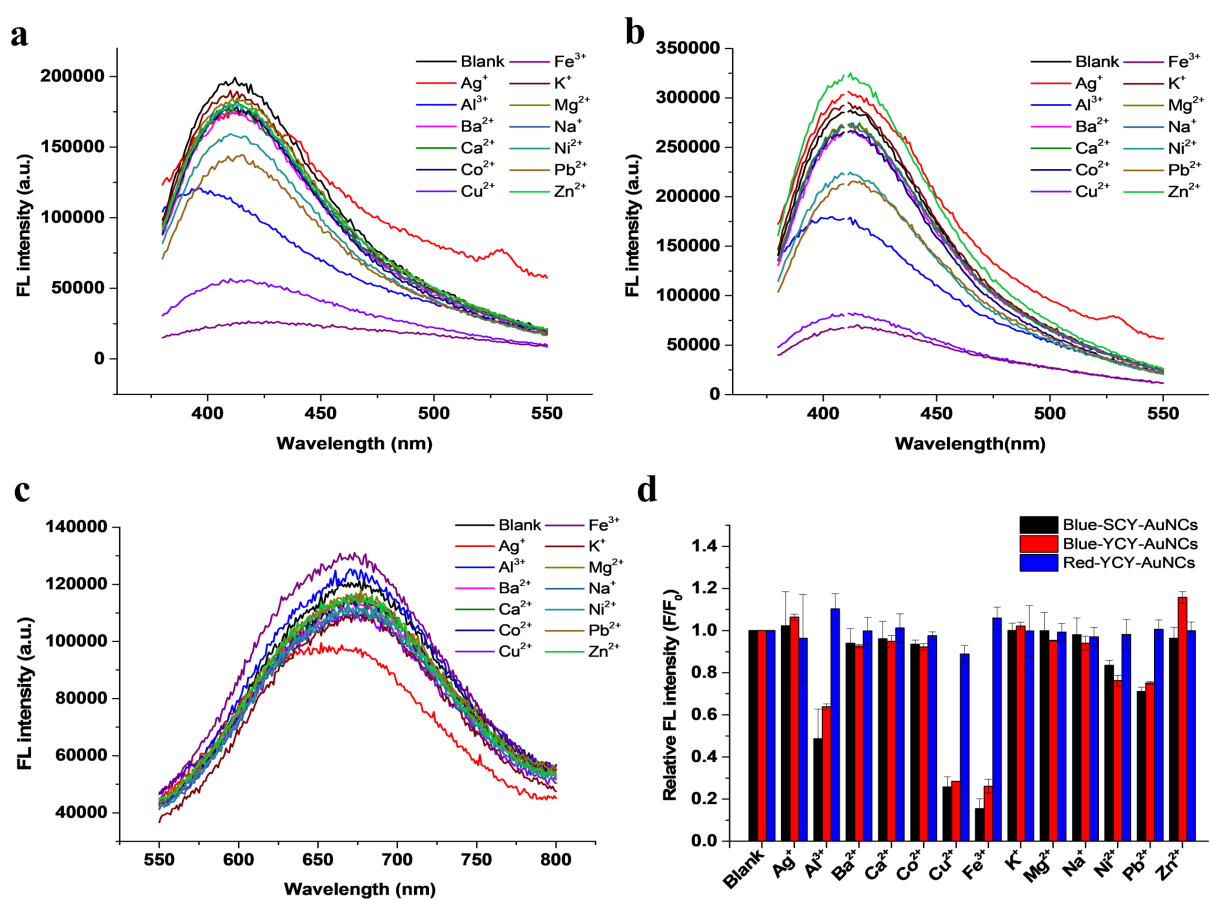


Figure 3.5. Effect of metal ions on fluorescence intensities of AuNCs. Fluorescence spectra of (a) the Blue-YCY-AuNC, (b) the Blue-SCY-AuNC, and (c) the Red-YCY-AuNC after mixing with 13 different metal ions. (c) Histogram plot of fluorescence quenching of each AuNC caused by 13 different metal ions (50 μ M) (excitation at 325 nm and 400 nm for blue-emitting AuNCs and red-emitting AuNC respectively; incubation time was 2 min. The error bars represent standard deviations obtained from three independent measurements.).

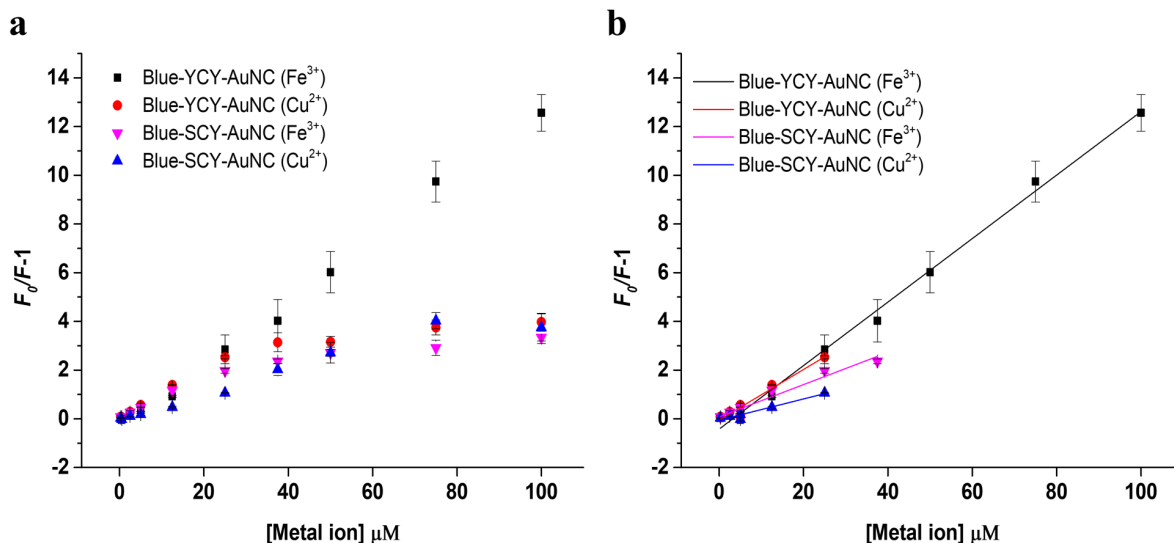


Figure 3.6. Fluorescence responses of Blue-YCY- and SCY-AuNCs upon addition of increasing concentration of Fe^{3+} and Cu^{2+} . (a) Plot of the values of $F_0/F-1$ at 415 nm versus the concentrations of Fe^{3+} and Cu^{2+} (b) Stern-Volmer plot of Blue-YCY-AuNC and Blue-SCY-AuNC against Fe^{3+} (Blue-YCY-AuNC: 0.25-100 μM , Blue-SCY-AuNC: 0.25-37.5 μM) and Cu^{2+} (Blue-YCY-AuNC: 0.25-25 μM , Blue-SCY-AuNC: 0.25-25 μM) (excitation at 325 nm; incubation time was 2 min. The error bars represent standard deviations obtained from three independent measurements.).

AuNCs to various metal ions. To pursue this, we incubated the same volume of the AuNC solution and 13 different metal ion solutions (100 μM) and measured fluorescence intensities. In Figure 3.5 a, a significant fluorescence quenching ($\sim 85\%$) of Blue-YCY-AuNC was found in the presence of 50 μM Fe^{3+} , and also 75% fluorescence quenching of Blue-SCY-AuNC was observed by comparing the blank sample (Figure 3.5 b). Furthermore, Blue-YCY- and SCY-AuNCs responded to Cu^{2+} and Al^{3+} with $\sim 75\%$ and $\sim 45\%$ quenching efficiency, respectively (Figure 3.5 a and b). On the other hand, Ag^+ , Ba^{2+} , Ca^{2+} , Co^{2+} , K^+ , Mg^{2+} , Na^+ , Ni^+ , Pb^{2+} , and Zn^{2+} ions did not significantly affect fluorescence signals of Blue-YCY- and SCY-AuNCs. Interestingly, the fluorescence signals of Red-YCY-AuNCs are stable for all 13 different metal ions (Figure 3.5 d). Figure 3.5 d displays the corresponding histogram plot of fluorescence quenching caused by individual metal ions. We

Table 3.1. Comparison sensing activity of Blue-YCY-AuNC and Blue-SCY-AuNC for Fe³⁺ and Cu²⁺

Sample	Detection metal ion	Slope & intercept	R ²	Linear detection range (μM)	Limit of Detection (μM)
Blue-YCY-AuNC	Fe ³⁺	Y=0.128x – 0.314	0.995	0.25 - 100	3.2
	Cu ²⁺	Y=0.101x + 0.0533	0.997	0.25 - 25	0.77
Blue-SCY-AuNC	Fe ³⁺	Y=0.0646x + 0.144	0.965	0.25 - 37.5	4.1
	Cu ²⁺	Y=0.0424x – 0.0144	0.993	0.25 -25	1.3

observed that both Blue-emitting AuNCs exhibit selective quenching toward Fe³⁺, Cu²⁺, and Al³⁺, but the Red-YCY-AuNC sustained the fluorescence signal for all 13 individual metal ions. Since both of blue-emitting AuNCs are more sensitive to Fe³⁺ and Cu²⁺, we further evaluated the interaction between blue-emitting AuNCs and two metal ions. We monitored changes in fluorescence under various concentrations of Fe³⁺ and Cu²⁺. The fluorescence quenching data was fitted to the Stern-Volmer equation:^{21,40}

$$F_0/F = 1 + K_{sv}[Q],$$

where K_{sv} is the Stern-Volmer quenching constant, $[Q]$ is the analyte quenchers (Fe³⁺ or Cu²⁺), and F_0 and F are the fluorescence intensities of the AuNCs at 415 nm in the absence and presence of metal ions. As observed in Figure 3.6 a, the intensities of the fluorescence emission at 415 nm gradually decreased as the concentrations of Fe³⁺ and Cu²⁺ increased, until approximately 40 μM when the emission begins to plateau (summarized in Table 3.1). Blue-YCY-AuNC for Fe³⁺ sensing, on the other hands, did not exhibit this plateautrend. Instead, fluorescence intensity continued to increase with Fe³⁺ and Cu²⁺ concentration, with a strong linear correlation R² of 0.995 and 0.997 at concentrations ranging from 0.25 μM to 100 μM and from 0.25 μM to 25 μM,

respectively (Figure 3.6 b). In addition, the Blue-YCY-AuNC also has a strong linear relationship with Fe^{3+} ($R^2=0.965$) and Cu^{2+} ($R^2=0.993$) from 0.25 μM to 37.5 μM and from 0.25 μM to 25 μM . Furthermore, Blue-YCY-AuNC exhibits higher sensitivity to Fe^{3+} and Cu^{2+} than the Blue-SCY-AuNC (Table 1), possibly due to the additional tyrosine residue in Blue-YCY-AuNC. The limit of detection (LOD) was calculated from the slope of the plot of the Stern-Volmer equation versus concentrations of Fe^{3+} and Cu^{2+} . The LOD value was calculated according to the assumption of LOD equal to $3\text{SD}/\text{S}$, where SD represents standard deviation of intercept and S represents the slope of linear curve.²⁸ We obtained 3.2 μM and 0.77 μM of LOD values for Blue-YCY-AuNC on sensing for Fe^{3+} and Cu^{2+} , respectively. The LODs for Blue-SCY-AuNC are 4.1 μM and 1.3 μM for sensing of Fe^{3+} and Cu^{2+} (Table 3.1). Therefore, two-tyrosine containing peptide (YCY)-templated AuNC has better optical sensor ability toward to Fe^{3+} .

3.3.4 Sensing mechanism

According to previous papers,^{36,38,39} ligands containing *o*-quinone can chelate Fe^{3+} and Cu^{2+} ions so that we examined the sensing mechanism by monitoring the hydrodynamic diameter of AuNCs after adding the Fe^{3+} and Cu^{2+} to AuNC solutions. In addition to Fe^{3+} and Cu^{2+} , we also tested Ni^{2+} as a control to validate that the aggregation of AuNCs would be occurred in presence of some specific target ions. The size-distribution histogram of each AuNC with Fe^{3+} and Cu^{2+} in Figure 3.7 revealed that the Blue-YCY-AuNC exceptionally tended to aggregate in the presence of Fe^{3+} ions, resulting in the formation of huge agglomerates (hydrodynamic diameter $\sim 1,200$ nm). Similarly, when the Blue-YCY-AuNC was mixed with Cu^{2+} , they formulated ~ 25 nm complexes,

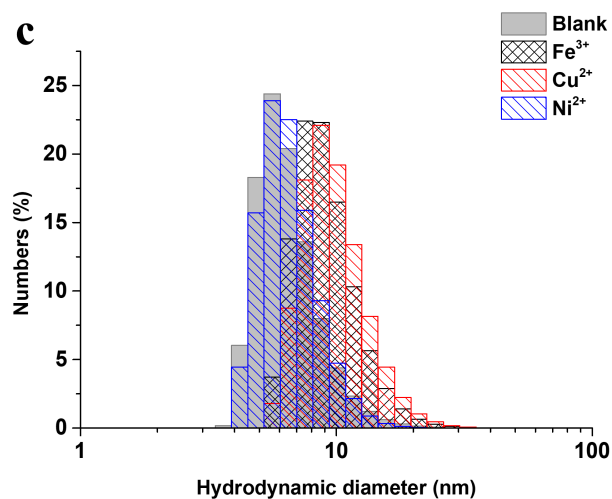
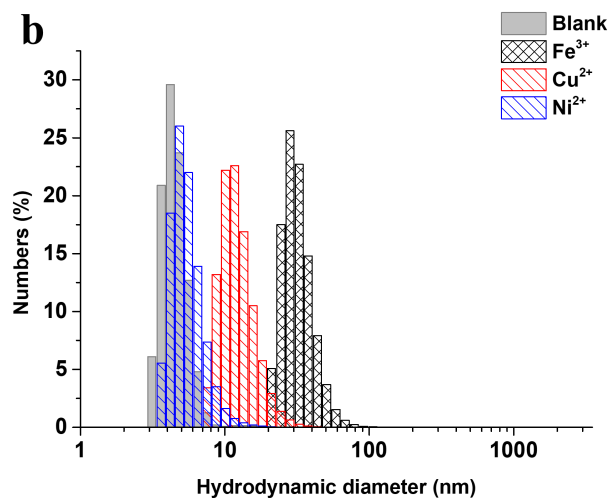
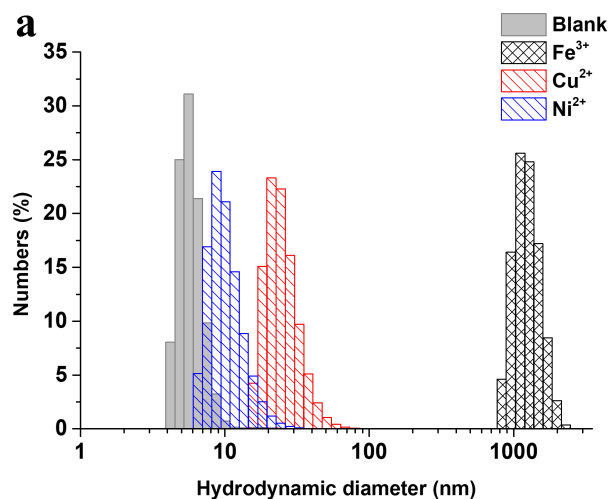


Figure 3.7. Hydrodynamic diameter analysis of AuNCs in the presence of metal ions. (a) the Blue-YCY-AuNC, (b) the Blue-SCY-AuNC, and (c) the Red-YCY-AuNC before and after adding of Ni²⁺, Fe³⁺ and Cu²⁺.

smaller than the complexes form from the Blue-YCY-AuNC and Fe^{3+} (Figure 3.7 a). The results strongly correlate with the tendency of the quenching efficiency of the Blue-YCY-AuNC towards Fe^{3+} and Cu^{2+} (Figure 3.5 d). With the identical circumstance, Fe^{3+} and Cu^{2+} induced the aggregation of Blue-SCY-AuNC forming ~ 33 nm and ~ 12 nm complexes, respectively (Figure 3.7 b). Whereas, there is no aggregation in the presence of Ni^{2+} in both of Blue-YCY- and SCY-AuNCs. In addition to these results, the DLS histogram of the Red-YCY-AuNC exhibits no aggregation even in the presence of Fe^{3+} and Cu^{2+} (Figure 3.7 c). The results of DLS measurement further provide evidence that the peptides on blue-emitting AuNCs and Red-YCY-AuNC have different binding configuration to Au atoms. Because of the absence of side chain groups, phenol group of tyrosine and $-\text{COOH}$ at C-terminal in YCY peptide on the Red-YCY-AuNC, the AuNC cannot form complexes with metal ions. In contrast, *o*-quinone of tyrosine residue and $-\text{NH}_2$ at N-terminal of YCY and SCY peptides on Blue-YCY- and SCY-AuNC may form complexes with Fe^{3+} and Cu^{2+} , resulting in aggregation-induced fluorescence quenching.^{25,41,42} Therefore, these findings indicate that *o*-quinones on the surface of AuNCs creates aggregation by forming complexes with the other ligands of adjacent AuNCs . In addition, based on the DLS results, the aggregation propensity and the sensing capacity of AuNC strongly correlate with the number of *o*-quinones of AuNCs.

3.4 Conclusion

In summary, by employing tyrosine-containing tripeptides with different number of tyrosine residue, we successfully synthesized fluorescent AuNCs with emission wavelength 415 nm and 670 nm in the absence of strong reducing agents. The as-prepared AuNCs displayed

ultrasmall size (< 2.5 nm), mono-dispersity, and uniform sphere shape in TEM images and DLS results. When the Blue-YCY-AuNC and Blue-SCY-AuNC were used to probe 13 kinds of common metal ions, only Fe^{3+} and Cu^{2+} ions could share a significant fluorescence quenching of AuNCs. On the contrary, Red-YCY-AuNC displayed stable fluorescence signal under the presence of 13 different metal ions. The Blue-YCY-AuNC showed more sensitive and wide sensing range of Fe^{3+} and Cu^{2+} than the Blue-SCY-AuNC with a lower detection limit of $3.2 \mu\text{M}$ and $0.77 \mu\text{M}$, respectively. The interaction mechanism and sensing performance of AuNCs were systematically investigated by fluorescence spectra and DLS. Corresponding to the fluorescence response of AuNCs to metal ions, the Fe^{3+} induced the aggregation of Blue-YCY-AuNC and formed larger complexes compared to complexes formed with Cu^{2+} . Furthermore, the Blue-SCY-AuNC induced aggregation under the presence of Fe^{3+} and Cu^{2+} , though these complexes are smaller than those of Blue-YCY-AuNC. Overall, although the number of tyrosine residue may not be considered to have a significant impact on the formation of AuNCs, the number of *o*-quinones, an oxidized form of tyrosine, on the surface of AuNC plays a critical role in the detection of target metal ions. These results not only provide a simple synthesis method of fluorescent AuNC with tyrosine containing peptides, but they also provide key design principles for understanding the coordination of peptide-templated AuNCs with metal ions. We strongly believe that this study will be helpful for the design of small molecule targeting metal ions as well as small biomolecules.

3.6 Supplementary information

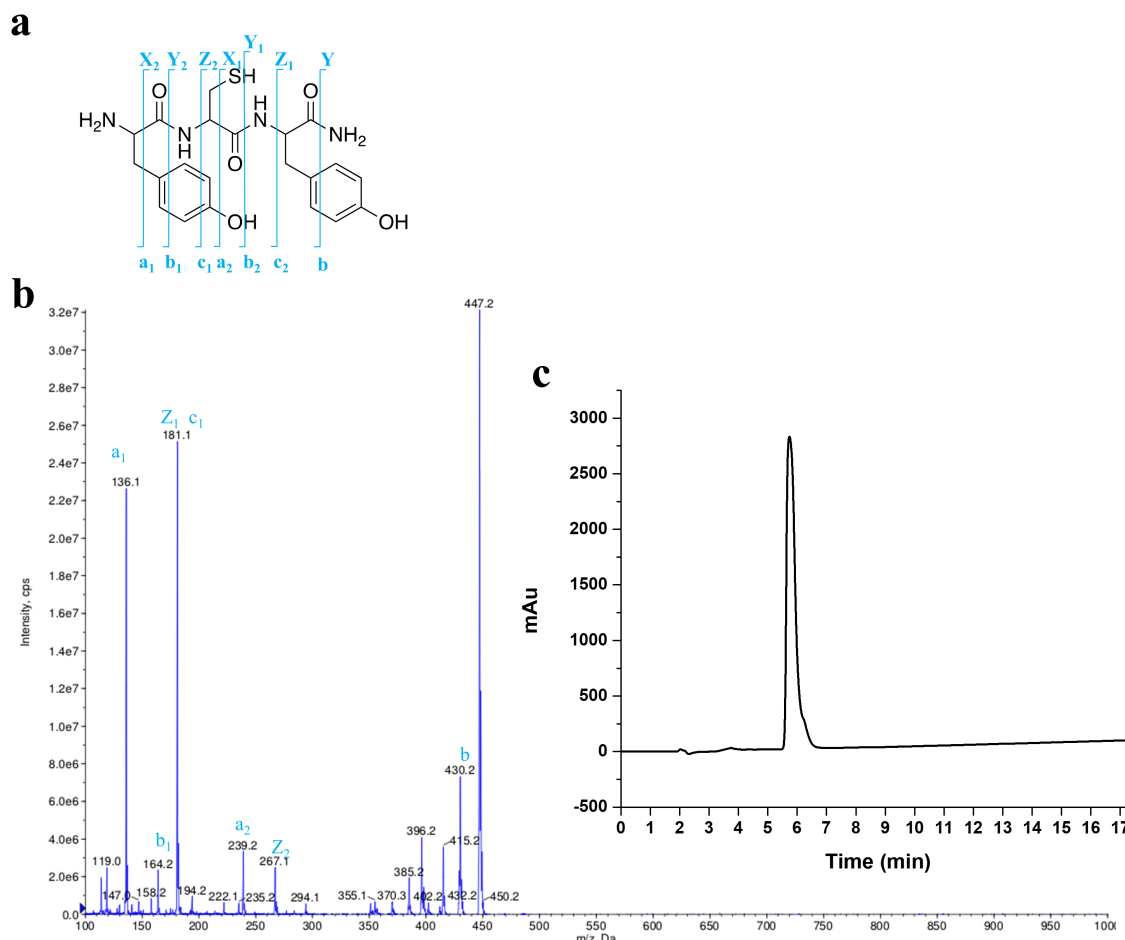


Figure S.3.1. Characterization of YCY peptide. (a) Structure of YCY peptide. (b) HPLC-MS/MS of YCY. (c) HPLC chromatogram of YCY peptide. The LC gradient for YCY was run at 0% to 30% solvent B (acetonitrile) over 20 min, then from 30% to 100% over 5 min, followed by 100% over 5 min, finally from 100% to 0% over 5 min.

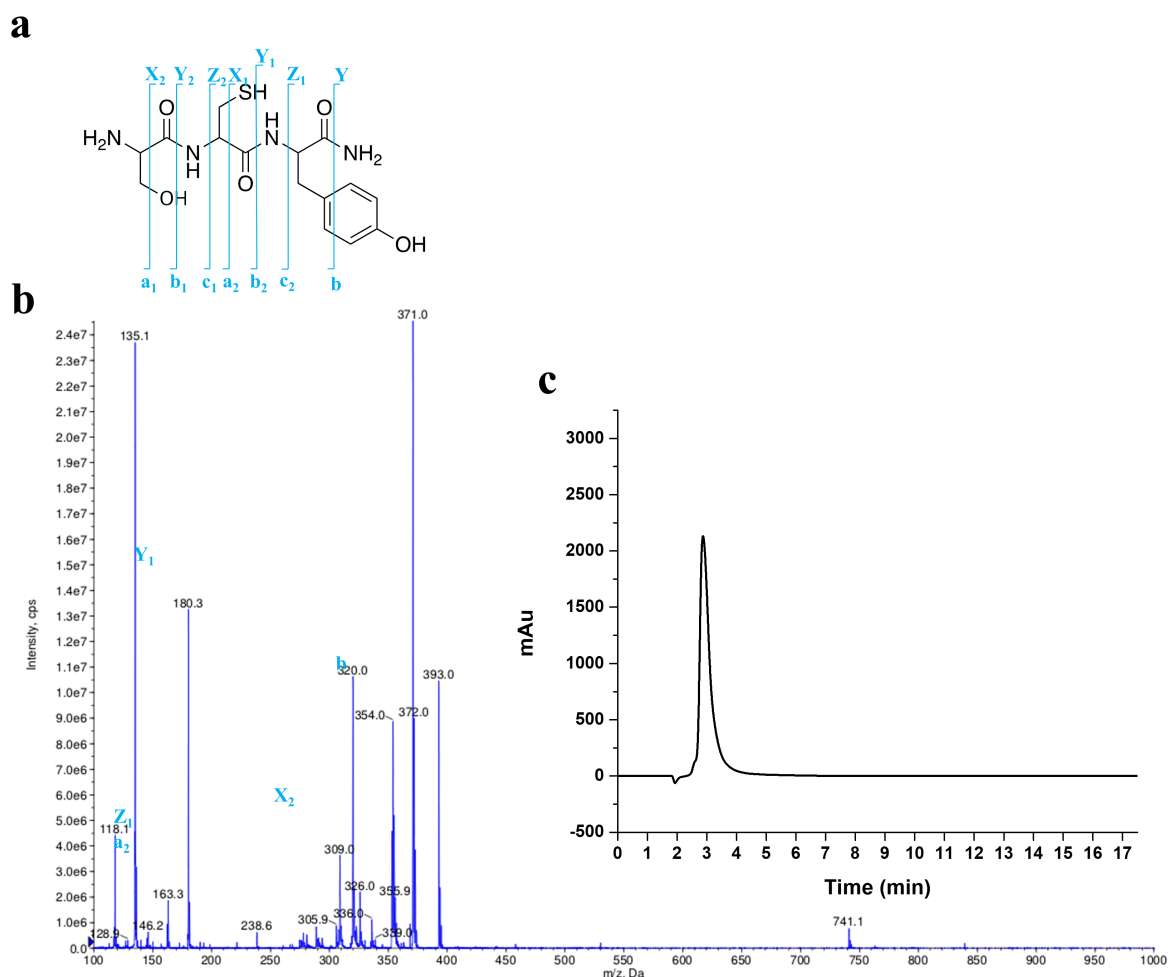


Figure S.3.2. Characterization of SCY peptide. (a) Structure of SCY peptide. (b) HPLC-MS/MS of SCY. (c) HPLC chromatogram of SCY peptide. The LC gradient for SCY peptide was run at 0% solvent B (acetonitrile) over 20 min, then from 0% to 100% over 5 min, followed by 100% over 5 min, finally from 100% to 0% over 5 min.

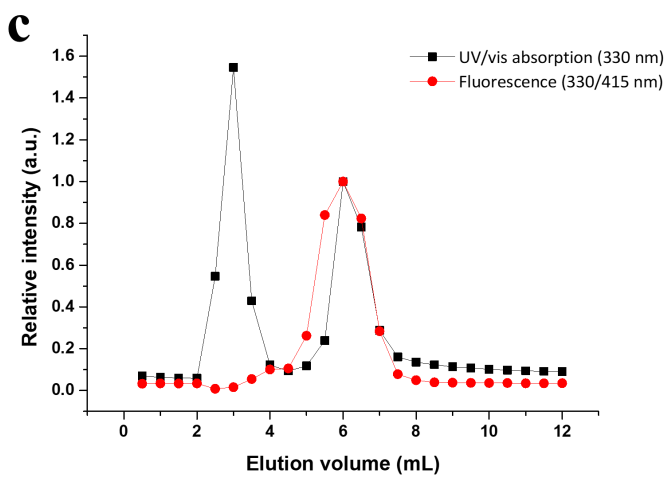
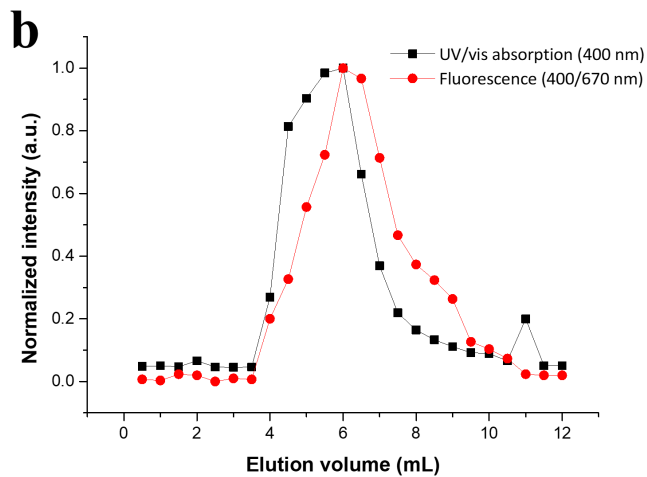
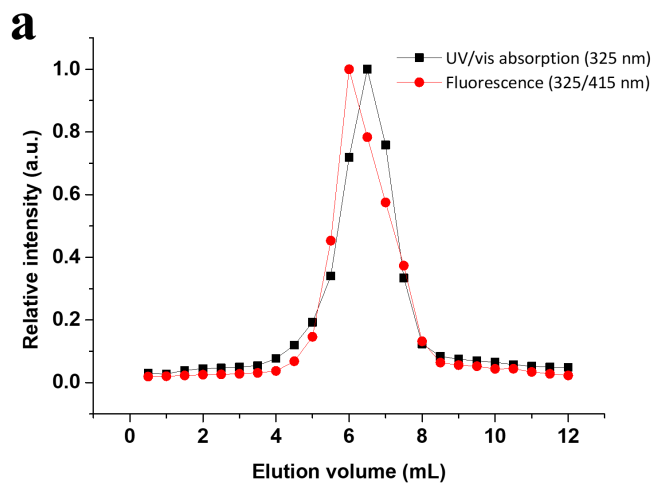


Figure S.3.3. Purification of the AuNCs vis size exclusion column. UV-vis absorption and fluorescence intensity of individual fractions from size exclusion chromatography (SephadexTM G-25): (a) Red-YCY-AuNC, (b) Blue-YCY-AuNC, and (c) Blue-SCY-AuNC.

3.6.1 Cell viability test

To determine a cytotoxicity of the AuNCs, WST-1 assay was performed. For WST-1 assay, we seeded 12,000 cells MCF-7 on 96 well plate and cultured for 24 h. The culture medium was change with the fresh medium containing varying concentration (10 – 1000 $\mu\text{g/mL}$) of the AuNCs. After 21 h, we added 10 μL WST-1 into each well and incubated for 3.5 h in cell incubator. The absorbances of product were read at 480 nm using microplate reader.

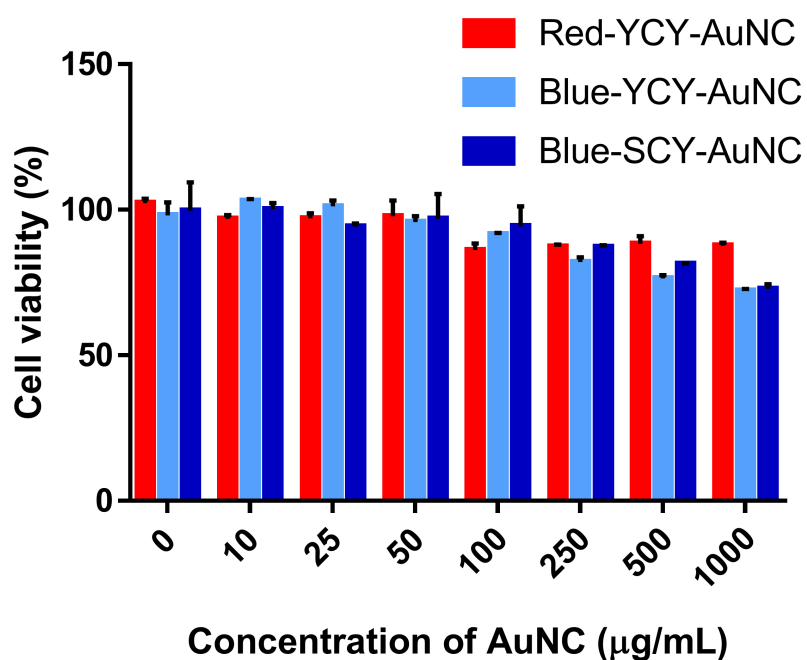


Figure S.3.4. Cytotoxicity of AuNCs. Cytotoxicity results of the AuNCs on MCF-7 cells in 24 h. Error bars indicate standard deviation of three samples.

3.6 References

- (1) Fang, J.; Li, J.; Zhang, B.; Yuan, X.; Asakura, H.; Tanaka, T.; Teramura, K.; Xie, J.; Yan, N. The Support Effect on the Size and Catalytic Activity of Thiolated Au 25nanoclusters as Precatalysts. *Nanoscale* **2015**, *7*, 6325–6333.
- (2) Yahia-Ammar, A.; Sierra, D.; Mérola, F.; Hildebrandt, N.; Le Guével, X. Self-Assembled Gold Nanoclusters for Bright Fluorescence Imaging and Enhanced Drug Delivery. *ACS Nano* **2016**, *10*, 2591–2599.
- (3) Ju, E.; Liu, Z.; Du, Y.; Tao, Y.; Ren, J.; Qu, X. Heterogeneous Assembled Nanocomplexes for Ratiometric Detection of Highly Reactive Oxygen Species in Vitro and in Vivo. *ACS Nano* **2014**, *8*, 6014–6023.
- (4) Zhang, C.; Li, C.; Liu, Y.; Zhang, J.; Bao, C.; Liang, S.; Wang, Q.; Yang, Y.; Fu, H.; Wang, K.; Cui, D. Gold Nanoclusters-Based Nanoprobes for Simultaneous Fluorescence Imaging and Targeted Photodynamic Therapy with Superior Penetration and Retention Behavior in Tumors. *Adv. Funct. Mater.* **2015**, *25*, 1314–1325.
- (5) Sun, S.; Ning, X.; Zhang, G.; Wang, Y.-C.; Peng, C.; Zheng, J. Dimerization of Organic Dyes on Luminescent Gold Nanoparticles for Ratiometric pH Sensing. *Angew. Chem. Int. Ed.* **2016**, *55*, 2421–2424.
- (6) Zhang, X.; Chen, X.; Jiang, Y.-W.; Ma, N.; Xia, L.-Y.; Cheng, X.; Jia, H.-R.; Liu, P.; Gu, N.; Chen, Z.; *et al.* Glutathione-Depleting Gold Nanoclusters for Enhanced Cancer Radiotherapy Through Synergistic External and Internal Regulations. *ACS Appl. Mater. Interfaces* **2018**, *10*, 10601–10606.

- (7) Zheng, K.; Setyawati, M. I.; Leong, D. T.; Xie, J. Antimicrobial Gold Nanoclusters. *ACS Nano* **2017**, *11*, 6904–6910.
- (8) Lee, T.-H.; Gonzalez, J. I.; Zheng, J.; Dickson, R. M. Single-Molecule Optoelectronics. *Acc. Chem. Res* **2005**, *38*, 534–541.
- (9) Zheng, J.; Nicovich, P. R.; Dickson, R. M. Highly Fluorescent Noble-Metal Quantum Dots. *Annu. Rev. Phys. Chem.* **2007**, *58*, 409–431.
- (10) El-Sayed, M. A. Some Interesting Properties of Metals Confined in Time and Nanometer Space of Different Shapes. *Acc. Chem. Res* **2001**, *34*, 257–264.
- (11) Jin, R. Quantum Sized, Thiolate-Protected Gold Nanoclusters. *Nanoscale* **2010**, *2*, 343–362.
- (12) Duan, H.; Nie, S. Etching Colloidal Gold Nanocrystals with Hyperbranched and Multivalent Polymers: a New Route to Fluorescent and Water-Soluble Atomic Clusters. *J. Am. Chem. Soc.* **2007**, *129*, 2412–2413.
- (13) Lin, C.-A. J.; Yang, T.-Y.; Lee, C.-H.; Huang, S. H.; Sperling, R. A.; Zanella, M.; Li, J. K.; Shen, J.-L.; Wang, H.-H.; Yeh, H.-I.; Parak, W. J.; Chang, W. H. Synthesis, Characterization, and Bioconjugation of Fluorescent Gold Nanoclusters Toward Biological Labeling Applications. *ACS Nano* **2009**, *3*, 395–401.
- (14) Chen, T.-H.; Nieh, C.-C.; Shih, Y.-C.; Ke, C.-Y.; Tseng, W.-L. Hydroxyl Radical-Induced Etching of Glutathione-Capped Gold Nanoparticles to Oligomeric Au I–Thiolate Complexes. *RSC Advances* **2015**, *5*, 45158–45164.
- (15) Song, W.; Liang, R.-P.; Wang, Y.; Zhang, L.; Qiu, J.-D. Green Synthesis of Peptide-Templated Gold Nanoclusters as Novel Fluorescence Probes for Detecting Protein Kinase Activity. *Chem. Commun.* **2015**, *51*, 10006–10009.

- (16) Chakraborty, S.; Babanova, S.; Rocha, R. C.; Desireddy, A.; Artyushkova, K.; Boncella, A. E.; Atanassov, P.; Martinez, J. S. A Hybrid DNA-Templated Gold Nanocluster for Enhanced Enzymatic Reduction of Oxygen. *J. Am. Chem. Soc.* **2015**, *137*, 11678–11687.
- (17) Li, H.; Huang, H.; Feng, J.-J.; Luo, X.; Fang, K.-M.; Wang, Z.-G.; Wang, A.-J. A Polypeptide-Mediated Synthesis of Green Fluorescent Gold Nanoclusters for Fe³⁺ Sensing and Bioimaging. *J. Colloid Interface Sci.* **2017**, *506*, 386–392.
- (18) Duan, Y.; Duan, R.; Liu, R.; Guan, M.; Chen, W.; Ma, J.; Chen, M.; Du, B.; Zhang, Q. Chitosan-Stabilized Self-Assembled Fluorescent Gold Nanoclusters for Cell Imaging and Biodistribution in Vivo. *ACS Biomater. Sci. Eng.* **2018**, *4*, 1055–1063.
- (19) Yang, L.; Wang, H.; Li, D.; Li, L.; Lou, X.; Liu, H. Self-Nucleation and Self-Assembly of Highly Fluorescent Au₅ Nanoclusters for Bioimaging. *Chem. Mater.* **2018**, *30*, 5507–5515.
- (20) Nandi, I.; Chall, S.; Chowdhury, S.; Mitra, T.; Roy, S. S.; Chattopadhyay, K. Protein Fibril-Templated Biomimetic Synthesis of Highly Fluorescent Gold Nanoclusters and Their Applications in Cysteine Sensing. *ACS Omega* **2018**, *3*, 7703–7714.
- (21) Liu, Y.; Ai, K.; Cheng, X.; Huo, L.; Lu, L. Gold-Nanocluster-Based Fluorescent Sensors for Highly Sensitive and Selective Detection of Cyanide in Water. *Adv. Funct. Mater.* **2010**, *20*, 951–956.
- (22) Zhang, N.; Si, Y.; Sun, Z.; Chen, L.; Li, R.; Qiao, Y.; Wang, H. Rapid, Selective, and Ultrasensitive Fluorimetric Analysis of Mercury and Copper Levels in Blood Using Bimetallic Gold–Silver Nanoclusters with “Silver Effect-”Enhanced Red Fluorescence. *Anal. Chem.* **2014**, *86*, 11714–11721.

- (23) Chen, T.-H.; Tseng, W.-L. (Lysozyme Type VI)-Stabilized Au₈ Clusters: Synthesis Mechanism and Application for Sensing of Glutathione in a Single Drop of Blood. *Small* **2012**, *8*, 1912–1919.
- (24) Zhang, J.; Cai, C.; Razzaque, S.; Hussain, I.; Lu, Q.-W.; Tan, B. Synthesis of Water-Soluble and Highly Fluorescent Gold Nanoclusters for Fe³⁺ Sensing in Living Cells Using Fluorescence Imaging. *J. Mater. Chem. B* **2017**, *5*, 5608–5615.
- (25) Annie Ho, J.-A.; Chang, H.-C.; Su, W.-T. DOPA-Mediated Reduction Allows the Facile Synthesis of Fluorescent Gold Nanoclusters for Use as Sensing Probes for Ferric Ions. *Anal. Chem.* **2012**, *84*, 3246–3253.
- (26) Bothra, S.; Upadhyay, Y.; Kumar, R.; Kumar, S. K. A.; Sahoo, S. K. Chemically Modified Cellulose Strips with Pyridoxal Conjugated Red Fluorescent Gold Nanoclusters for Nanomolar Detection of Mercuric Ions. *Biosensors and Bioelectronics* **2017**, *90*, 329–335.
- (27) Wang, J.; Ma, S.; Ren, J.; Yang, J.; Qu, Y.; Ding, D.; Zhang, M.; Yang, G. Fluorescence Enhancement of Cysteine-Rich Protein-Templated Gold Nanoclusters Using Silver(I) Ions and Its Sensing Application for Mercury(II). *Sensors & Actuators: B. Chemical* **2018**, *267*, 342–350.
- (28) Bain, D.; Maity, S.; Paramanik, B.; Patra, A. Core-Size Dependent Fluorescent Gold Nanoclusters and Ultrasensitive Detection of Pb²⁺ Ion. *ACS Sustainable Chem. Eng.* **2017**, *6*, 2334–2343.
- (29) Deng, L.; Zhou, Z.; Li, J.; Li, T.; Dong, S. Fluorescent Silver Nanoclusters in Hybridized DNA Duplexes for the Turn-on Detection of Hg²⁺ Ions. *Chem. Commun.* **2011**, *47*, 11065–3.

- (30) Zhao, Q.; Chen, S.; Zhang, L.; Huang, H.; Zeng, Y.; Liu, F. Multiplex Sensor for Detection of Different Metal Ions Based on on-Off of Fluorescent Gold Nanoclusters. *Analytica Chimica Acta* **2014**, *852*, 236–243.
- (31) Xie, J.; Zheng, Y.; Ying, J. Y. Highly Selective and Ultrasensitive Detection of Hg²⁺ Based on Fluorescence Quenching of Au Nanoclusters by Hg²⁺–Au⁺ Interactions. *Chem. Commun.* **2010**, *46*, 961–963.
- (32) Selvakannan, P. R.; Swami, A.; Srisathiyarayanan, D.; Shirude, P. S.; Pasricha, R.; Mandale, A. B.; Sastry, M. Synthesis of Aqueous Au Core–Ag Shell Nanoparticles Using Tyrosine as a pH-Dependent Reducing Agent and Assembling Phase-Transferred Silver Nanoparticles at the Air–Water Interface. *Langmuir* **2004**, *20*, 7825–7836.
- (33) Bifunctional Peptides That Precisely Biomineralize Au Clusters and Specifically Stain Cell Nuclei. *Chem. Commun.* **2012**, *48*, 871–873.
- (34) Zhang, G.; Li, Y.; Xu, J.; Zhang, C.; Shuang, S.; Dong, C.; Choi, M. M. F. Glutathione-Protected Fluorescent Gold Nanoclusters for Sensitive and Selective Detection of Cu²⁺. *Sensors & Actuators: B. Chemical* **2013**, *183*, 583–588.
- (35) Vasimalai, N.; Fernández-Argüelles, M. T.; Espiña, B. Detection of Sulfide Using Mercapto Tetrazine-Protected Fluorescent Gold Nanodots: Preparation of Paper-Based Testing Kit for on-Site Monitoring. *ACS Appl. Mater. Interfaces* **2018**, *10*, 1634–1645.
- (36) Contino, A.; Maccarrone, G.; Zimbone, M.; Reitano, R.; Musumeci, P.; Calcagno, L.; Pietro Oliveri, I. Tyrosine Capped Silver Nanoparticles: a New Fluorescent Sensor for the Quantitative Determination of Copper(II) and Cobalt(II) Ions. *J. Colloid Interface Sci.* **2016**, *462*, 216–222.

- (37) Pettit, L. D.; Steel, I.; Kowalik, T.; Kozlowski, H.; Bataille, M. Specific Binding of the Tyrosine Residue in Copper(II) Complexes of Tyr-Pro-Gly-Tyr and Tyr-Gly-Pro-Tyr. *J. Chem. Soc., Dalton Trans.* **1985**, 1201–1205.
- (38) Gordon, D. J.; Fenske, R. F. Theoretical Study of O-Quinone Complexes of Iron. *Inorg. Chem.* **1982**, *21*, 2916–2923.
- (39) Dikalov, S. I.; Rumyantseva, G. V.; Piskunov, A. V.; Weiner, L. M. Role of Quinone-Iron(III) Interaction in NADPH-Dependent Enzymic Generation of Hydroxyl Radicals. *Biochemistry* **1992**, *31*, 8947–8953.
- (40) Lu, W.; Qin, X.; Liu, S.; Chang, G.; Zhang, Y.; Luo, Y.; Asiri, A. M.; Al-Youbi, A. O.; Sun, X. Economical, Green Synthesis of Fluorescent Carbon Nanoparticles and Their Use as Probes for Sensitive and Selective Detection of Mercury(II) Ions. *Anal. Chem.* **2012**, *84*, 5351–5357.
- (41) Zhou, T.-Y.; Lin, L.-P.; Rong, M.-C.; Jiang, Y.-Q.; Chen, X. Silver–Gold Alloy Nanoclusters as a Fluorescence-Enhanced Probe for Aluminum Ion Sensing. *Anal. Chem.* **2013**, *85*, 9839–9844.
- (42) Huang, C.-C.; Yang, Z.; Lee, K.-H.; Chang, H. T. Synthesis of Highly Fluorescent Gold Nanoparticles for Sensing Mercury(II). *Angew. Chem. Int. Ed.* **2007**, *119*, 6948–6952.

CHAPTER 4

SUMMARY AND FUTURE RESEARCH DIRECTIONS

4.1. Summary

Rapid advances in nanotechnology have led to such applications; nanomedicine, therapeutic mediation, imaging tool and sensing tools. Among various nanomaterials, the dissertation research presented herein focused on gold nanoparticles. The preceding chapters have detailed new designs in the gold nanorod for cancer stem cell treatment and have introduced the noble synthetic method for gold nanoclusters and their application in metal ions sensing. First, in Chapter 1, the concept of gold nanoparticle was described to provide better understating of unique optical, physical and chemical properties of gold nanoparticles in different size and shape.

In Chapter 2, the new design of gold nanorod that selectively binds to cancer stem cells and its application in hyperthermia therapy were described. Prior to this research, our group identified the synthetic ligand that specifically binds to cancer stem cells. The AuNR modified by this ligand on its surface selectively bound to cancer stem cells in MCF-7 cells. The AuNR showed better binding toward cancer stem cells over non-cancer stem cells by 5 times. Under the hyperthermia treatment, CSC population in MCF-7 cells treated by the AuNR was reduced by >50%, proved by in situ ALDEFLUOR assay. Also, we provided Western blot analysis data to support the notion decrease CSC population by seeing CSC-associated transcription factors, KLF4, C-myc, Nanog and Sox2.

In Chapter 3, the noble synthetic method for gold nanocluster using tyrosine as catalyst was demonstrated. We designed two tripeptides, tyrosine-cysteine-tyrosine (YCY) and serine-cysteine-tyrosine (SCY) to understand the role of tyrosine in forming fluorescent AuNC. By

adjusting pH to be basic, the mixture of gold ion and peptides formed fluorescent gold nanoclusters. The YCY peptide formed gold nanocluster emitting strong blue and red fluorescence and strong blue fluorescence was generated from the SCY peptide-templated gold nanocluster. Gold nanoclusters exhibited monodispersed with outstanding uniformity in size and spherical shape. These gold nanoclusters exhibited potential metal ions sensing tools because in the presence of Fe^{3+} and Cu^{2+} , fluorescence of gold nanoclusters was efficiently quenched and showed linear quenching response in a wide linear range. The results of hydrodynamic diameter distribution of gold nanoclusters after mixing with metal ions suggested that the fluorescence quenching was caused aggregation resulted from chelation between the peptide on the nanocluster and the target ion. The sensing capability of gold nanocluster is probably associated with the number of tyrosine residue in peptide.

4.2. Future research directions

4.2.1 Cancer stem cell targeted nanomedicine

Although we have demonstrated that our noble gold nanorod specifically targeted and efficiently reduced cancer stem cell population, there are remained things we must address and understand. First, we need to examine the capacity of cancer stemness after treatment. Mammosphere formation assay, which has been broadly used for the quantification of cancer stem cell activity can be used for assess the stemness of the cancer cells treated by gold nanorod and hyperthermia.¹⁻⁵ Restore of sensitivity to conventional therapies such as radiotherapy and chemotherapy may also provide an evidence that can support our hypothesis.⁵⁻⁸ Transplantation of cancer cells has been used to examine the tumor-initiating ability of cancer stem cells.^{5,9} By

utilizing transplantation, we will be able to give the answer of efficiency of our treatment. Second, we need to optimize the condition of laser irradiation. As mentioned in Chapter 1, different type of laser resulted in different result. For instance, continuous laser would be efficient to eliminate not only cancer stem cell population but also ablate to normal cancer cells.^{2,4,10,11} Expanding this research, different gold nanoparticle, such as nanoshell or nanocage would be able to be employed not only to improve an efficiency of cancer stem cell ablation but also to achieve synergistic effect by loading drugs inside of nanoparticles.^{4,12}

4.2.2 Gold nanocluster for metal ion sensor and bioimaging

Although we have demonstrated that our noble method is utilized to synthesize fluorescent gold nanocluster, we may need to discover the better method to achieve gold nanocluster possessing improved quantum yield.^{13,14} As one of methods, we may design new peptides having more tyrosine or cysteine residue because rich number of these residue in ligand will improve reducing capability resulting in improvement of brightness and quantum yield.^{15,16}

Fe^{3+} and Cu^{2+} play crucial role in not only environment but also regulation of biological process. For these reasons, several studies have reported the using of gold nanoclusters for detection of metal ions in biological system.^{14,17-20} Based on these results, we may utilize our gold nanoclusters to detect metal ion inside of cell.

4.3. References

- (1) Sun, T.-M.; Wang, Y.-C.; Wang, F.; Du, J.-Z.; Mao, C.-Q.; Sun, C.-Y.; Tang, R.-Z.; Liu, Y.; Zhu, J.; Zhu, Y.-H.; Yang, X.-Z.; Wang, J. Cancer Stem Cell Therapy Using Doxorubicin Conjugated to Gold Nanoparticles via Hydrazone Bonds. *Biomaterials* **2014**, *35*, 836–845.
- (2) Xu, Y.; Wang, J.; Li, X.; Liu, Y.; Dai, L.; Wu, X.; Chen, C. Selective Inhibition of Breast Cancer Stem Cells by Gold Nanorods Mediated Plasmonic Hyperthermia. *Biomaterials* **2014**, *35*, 4667–4677.
- (3) Yao, H.-J.; Zhang, Y.-G.; Sun, L. The Effect of Hyaluronic Acid Functionalized Carbon Nanotubes Loaded with Salinomycin on Gastric Cancer Stem Cells. *Biomaterials* **2014**, *35*, 9208–9223.
- (4) Sun, T.; Wang, Y.; Wang, Y.; Xu, J.; Zhao, X.; Vangveravong, S.; Mach, R. H.; Xia, Y. Using SV119-Gold Nanocage Conjugates to Eradicate Cancer Stem Cells Through a Combination of Photothermal and Chemo Therapies. *Adv. Healthcare Mater.* **2014**, *3*, 1283–1291.
- (5) Atkinson, R. L.; Zhang, M.; Diagaradjane, P.; Peddibhotla, S.; Contreras, A.; Hilsenbeck, S. G.; Woodward, W. A.; Krishnan, S.; Chang, J. C.; Rosen, J. M. Thermal Enhancement with Optically Activated Gold Nanoshells Sensitizes Breast Cancer Stem Cells to Radiation Therapy. *Sci. Translational Med.* **2010**, *2*, 55ra79–55ra79.
- (6) Sadhukha, T.; Niu, L.; Wiedmann, T. S.; Panyam, J. Effective Elimination of Cancer Stem Cells by Magnetic Hyperthermia. *Mol. Pharmaceutics* **2013**, *10*, 1432–1441.

- (7) Chen, Z.; Zhu, P.; Zhang, Y.; Liu, Y.; He, Y.; Zhang, L.; Gao, Y. Enhanced Sensitivity of Cancer Stem Cells to Chemotherapy Using Functionalized Mesoporous Silica Nanoparticles. *Mol. Pharmaceutics* **2016**, *13*, 2749–2759.
- (8) Ke, X.-Y.; Ng, V. W. L.; Gao, S.-J.; Tong, Y. W.; Hedrick, J. L. Co-Delivery of Thioridazine and Doxorubicin Using Polymeric Micelles for Targeting Both Cancer Cells and Cancer Stem Cells. **2014**, *35*, 1096–1108.
- (9) Wang, X.; Low, X. C.; Hou, W.; Abdullah, L. N.; Toh, T. B.; Mohd Abdul Rashid, M.; Ho, D.; Chow, E. K.-H. Epirubicin-Adsorbed Nanodiamonds Kill Chemoresistant Hepatic Cancer Stem Cells. **2014**, *8*, 12151–12166.
- (10) Conde, J.; Oliva, N.; Zhang, Y.; Artzi, N. Local Triple-Combination Therapy Results in Tumour Regression and Prevents Recurrence in a Colon Cancer Model. *Nature Mater* **2016**, *15*, 1128–1138.
- (11) Liu, Y.; Yang, M.; Zhang, J.; Zhi, X.; Li, C.; Zhang, C.; Pan, F.; Wang, K.; Yang, Y.; Martinez de la Fuentea, J.; Cui, D. Human Induced Pluripotent Stem Cells for Tumor Targeted Delivery of Gold Nanorods and Enhanced Photothermal Therapy. *ACS Nano* **2016**, *10*, 2375–2385.
- (12) Xia, Y.; Li, W.; Cobley, C. M.; Chen, J.; Xia, X.; Zhang, Q.; Yang, M.; Cho, E. C.; Brown, P. K. Gold Nanocages: From Synthesis to Theranostic Applications. *Acc. Chem. Res.* **2011**, *44*, 914–924.
- (13) Pyo, K.; Thanthirige, V. D.; Kwak, K.; Pandurangan, P.; Ramakrishna, G.; Lee, D. Ultrabright Luminescence From Gold Nanoclusters: Rigidifying the Au(I)–Thiolate Shell. *J. Am. Chem. Soc.* **2015**, *137*, 8244–8250.

- (14) Nandi, I.; Chall, S.; Chowdhury, S.; Mitra, T.; Roy, S. S.; Chattopadhyay, K. Protein Fibril-Templated Biomimetic Synthesis of Highly Fluorescent Gold Nanoclusters and Their Applications in Cysteine Sensing. *ACS Omega* **2018**, *3*, 7703–7714.
- (15) Zhao, J.-Y.; Cui, R.; Zhang, Z.-L.; Zhang, M.; Xie, Z.-X.; Pang, D.-W. Cytotoxicity of Nucleus-Targeting Fluorescent Gold Nanoclusters. *Nanoscale* **2014**, *6*, 13126–13134.
- (16) Ghosh, S.; Anand, U.; Mukherjee, S. Luminescent Silver Nanoclusters Acting as a Label-Free Photoswitch in Metal Ion Sensing. *Anal. Chem.* **2014**, *86*, 3188–3194.
- (17) Tian, D.; Qian, Z.; Xia, Y.; Zhu, C. Gold Nanocluster-Based Fluorescent Probes for Near-Infrared and Turn-on Sensing of Glutathione in Living Cells. *Langmuir* **2012**, *28*, 3945–3951.
- (18) Shang, L.; Yang, L.; Stockmar, F.; Popescu, R.; Trouillet, V.; Bruns, M.; Gerthsen, D.; Nienhaus, G. U. Microwave-Assisted Rapid Synthesis of Luminescent Gold Nanoclusters for Sensing Hg^{2+} in Living Cells Using Fluorescence Imaging. *Nanoscale* **2012**, *4*, 4155–4156.
- (19) Huang, H.; Li, H.; Feng, J.-J.; Wang, A.-J. One-Step Green Synthesis of Fluorescent Bimetallic Au/Ag Nanoclusters for Temperature Sensing and in Vitro Detection of Fe^{3+} . *Sensors & Actuators: B. Chemical* **2016**, *223*, 550–556.
- (20) Li, H.; Huang, H.; Feng, J.-J.; Luo, X.; Fang, K.-M.; Wang, Z.-G.; Wang, A.-J. A Polypeptide-Mediated Synthesis of Green Fluorescent Gold Nanoclusters for Fe^{3+} Sensing and Bioimaging. *J. Colloid Interface Sci.* **2017**, *506*, 386–392.

BIOGRAPHICAL SKETCH

When Jonghae was sophomore, he had a brain surgery due to a car accident. While in an intensive care unit, he encountered a number of patients who suffered from either serious injury, such as cancers, or cardiac disorders, and pondered what he could do for them using his knowledge and skills. Ever since, this unique motivation attracted him to biomedical science. After recovering from the surgery, he returned to college as a very mature student and became serious about his chemistry major and future as a scientist; his desire was to use his knowledge and abilities to ultimately improve human lives.

Jonghae was interested in advanced diagnostic methods that aid in disease prevention and treatment. Thus, after his second year of undergraduate study, he joined a research lab well-known for its development of biomedical application. He had concentrated on a sol-gel chemistry to develop a biosensor to diagnose diseases while he was an undergraduate student. Jonghae continued his research by entering a graduate program at same university. He led three independent projects, which are preparation of superhydrophobic surfaces preventing bacterial adhesion, nitric oxide-releasing superhydrophobic coating and nitric oxide-storing and releasing electro-spun nanofiber.

His past research experiences have trained him with the scientific knowledge and skills for biomedical application, sparking his curiosity and fascination to how his invented materials can be applied in a living organism. This curiosity led him to enroll into a PhD program at The University of Texas at Dallas, where he had the honor of working with Dr. Jiyong Lee, who has been acknowledged widely for his work in discovering small molecules for human disease treatment using a novel combinatorial chemical library. His project of 4 years focuses on

discovering novel inhibitors for the treatment of metastatic cancers, including breast, lung, and ovarian cancers. He partook in the discovery of a novel compound, LC129-8, that specifically targets and suppresses triple negative breast cancer.

With his accumulated experience in material chemistry and chemical biology, he desires to combine these experiences that ultimately allow him to not only develop improved techniques for drug discovery, but also invent advanced therapeutic technologies. For this, he is collaborating with Dr. Zhenpeng Qin in the Department of Mechanical Engineering to utilize ligand conjugated gold nanorods to target and eliminate breast cancer stem cells via light-induced hyperthermia.

In addition to research activities, he has devoted his time to the foundation of the Chemistry Graduate Student Association (CGSA).¹ As founder and president of the CGSA, he made it his goal to increase outreach and focused on increasing minority participation within the STEM fields. One of his achievements was that he invited Dr. John Rogers from the University of Illinois Urbana-Champaign (current Northwestern University), who is renowned in the field of biomedical application, for a seminar in the department. In addition, Jonghae arranged and coordinated a special talk by Dr. Rogers in which he advised graduate students on career paths and advancement.

Jonghae has been constantly exploring the biomedical sciences to provide any help to the improvement of human life. Despite the obstacles and challenges he faced with his research projects, his strong desire to discover and impact human lives keeps him from stopping, and he is constantly eager to challenge new research.

1. Co-founder and co-president of Chemistry Graduate Student Association in the University of Texas at Dallas.

CURRICULUM VITAE

JONGHAE YOUN

Department of Chemistry and Biochemistry

The University of Texas at Dallas

800 West Campbell Road, Richardson, Texas 75080-3021

E-mail: Jonghae.Youn@utdallas.edu

Education and Training

- 2014–2019 **Doctor of Philosophy** Department of Chemistry and Biochemistry
University of Texas at Dallas, Richardson, United States
Research advisor: Professor Jiyong Lee
- 2010–2012 **Master of Science** Department of Chemistry
Kwangwoon University, Seoul, South Korea
Research advisor: Professor Jae Ho Shin
- 2006–2010 **Bachelor of Science** Department of Chemistry
Kwangwoon University, Seoul, South Korea

Awards and Scholarships

- 2019 PhD Research Small Grant (\$1000)
- 2018 Korean UTD KSA scholarship (\$1000)
- 2016 Korean UTD KSA scholarship (\$1000)

Research Experience

2014– Present **Graduate Research Assistant**, Department of Chemistry and Biochemistry,

Lee lab of chemical biology, University of Texas at Dallas

(Advisor: Professor Jiyong Lee)

- Identification of novel compound targeting triple negative breast cancer cells
- Elimination of cancer stem cells by gold nanorods hyperthermia
- Development of peptide-stabilized gold nanocluster for sensing Cu(II) and reactive oxygen species.

2012–2014 **Research Scientist**, Department of Chemistry,

Chemical Sensor Research Group, Kwangwoon University (Advisor: Professor Jae

Ho Shin)

- Designed superhydrophobic coatings using hybrid organic-inorganic sol-gel materials based on epoxy-amine systems: enhancing mechanical durability

2010 & 2012 **Visiting Researcher**, Department of Chemistry, Laboratory of Professor Mark

H. Schoenfish, University of North Carolina at Chapel Hill, Raleigh, NC,

United States

(Advisor: Professor Jae Ho Shin and Professor Mark H. Schoenfish)

- Succeeded in process development and preparation of simple and facile technique to prepare superhydrophobic surfaces with anti-bacterial properties
- Introduced superhydrophobic nitric oxide-releasing xerogels

2010–2012 **Graduate Research Assistant**, Department of Chemistry,

Chemical Sensor Research Group, Kwangwoon University (Advisor: Professor Jae

Ho Shin)

- Designed superhydrophobic coatings using silica-polymer hybrid nanocomposite.
- Developed nitric oxide-storing and releasing electrospun-nanofiber.

2008–2010 **Undergraduate Researcher**, Department of Chemistry,
Chemical Sensor Research Group, Kwangwoon University (Advisor: Professor Jae
Ho Shin)

- Synthesized ferrocene-modified silica nanoparticles as an electrochemical probe for label-free electrochemical aptamer sensors

Skills and Techniques

- High throughput on-bead one-compound screening
- Cell viability test: MTT and WST-1
- Mammalian cell culture
- Mass spectrometry: MALDI-TOF and LC-MS
- Fluorescence microscopy
- Confocal microscopy
- Dynamic Light Scattering
- Solid phase synthesis: peptides and peptoids
- Protein analysis by Western Blot
- ELISA-like binding assay

Publications

Complete list of published work:

<https://www.ncbi.nlm.nih.gov/pubmed/?term=Jonghae+youn>

- Youn, J.; Kang, P.; Qin, Z.; Lee, J. “Selective elimination of breast cancer stem cells by gold nanorod hyperthermia” **In preparation.**

- Youn, J.; Kim, P.; Kang, P.; Qin, Z.; Lee, J. “Tyrosine-assisted fluorescent gold nanoclusters for sensing Fe³⁺ and Cu²⁺” **In preparation.**
- Chen, L.; Long, C.; Youn, J.; Lee, J. “A phenotypic cell-binding screen identifies a novel compound targeting triple-negative breast cancer” *ACS Combinatorial Science* **2018**, *20* (6), 330-334.
- Storm, W. L.*; Youn, J.*; Reighard, K. P.; Worley, B V. Lodaya, H. M.; Shin, J. H.; Schoenfisch, M. H. Superhydrophobic nitric oxide-releasing xerogels, *Acta Biomaterialia*, **2014**, *10*(8), 3442-3448. *co-first authors
- Privett, B. J.; Youn, J.; Hong, S. A.; Lee, J.; Han, J.; Shin, J. H.; and Schoenfisch, M. H.; Antibacterial Fluorinated Silica Colloid Superhydrophobic Surfaces. *Langmuir*, **2011**, *27*(15), 9597-9601.

Patents

- Jae Ho Shin, Woo-Young Jung, Mingoo Kim, and Jonghae Youn “Method for producing nanofibers capable of storing and transferring nitric oxide and nanofibers capable of storing and transferring nitric oxide produced thereby” US Patent US9879362B2
- Benjamin Privett, Mark H. Schoenfisch, Jae Ho Shin, and Jonghae Youn “Superhydrophobic coatings and methods for their preparation,” US Patent US9675994B2
- Jae Ho Shin, Woo-Young Jung, Mingoo Kim, and Jonghae Youn “a fabricating method of nanofibers as a nitric oxide storage and delivery scaffold and the nanofibers as a nitric oxide storage and delivery scaffold fabricated thereby” Korean Patent 10-1743124-0000
- Jae Ho Shin, Seung-Un Shim, Jeong Bong Lee, Jonghae Youn “Biosensor for glycosylated hemoglobin using electrochemically active nanoparticles” Korean Patent 10-1721572-0000
- Jae Ho Shin, Jonghae Youn, Woo-Young Jung, Mingoo Kim, Eunji-Hwang, and Yu Bin Jung. “a Method of fabricating superhydrophobic surface coating” Korean Patent 10-1468817-0000
- Jiyeon Lee, Jonghae Youn, Jeongyeon Choi, Junhee Han, Sukkyu Kim, Ji Hoon Lee, Hakhyun Nam, Geun Sig Cha, and Jae Ho Shin “Label-Free electrochemical aptamer sensor using nanoparticles” Korean Patent 10-1321082-0000

Teaching Experience

2014–2019 **Teaching Assistant, Department of Chemistry and Biochemistry**

University of Texas at Dallas, Richardson, United States

- General Chemistry Laboratory I and II.

2010–2012 **Teaching Assistant, Department of Chemistry**

Kwangwoon University, Seoul, South Korea

- General Chemistry Experiments
- Physical Analytical Chemistry Laboratory